Back-action and coherent oscillation in a suspended nanotube resonator



Yutian Wen

Linacre College

University of Oxford

A thesis submitted for the degree of

Doctor of Philosophy

Hilary 2020

To my parents.

Abstract

The constant development of mesoscopic physics demands ever more precise and fast measurement and control of nanoscale objects. In this thesis, I demonstrate a sensitive electrical measurement of a carbon nanotube mechanical resonator at radio frequency, and the observation of its coherent oscillation as a consequence of the measurement back-action.

A single-electron transistor is embedded in the nanotube, the conductance of which is sensitive to the resonator displacement. The measurement scheme exploits this linear transduction and amplifies the electrical signal with an impedance-matching tank circuit followed by cryogenic amplifiers. As a result, the vibration displacement can be continuously monitored at radio frequency, with a sensitivity approaching within a factor 470 of the standard quantum limit.

The remarkable sensitivity is accompanied with strong back-action forces from electron tunnelling which randomly perturb the mechanical states. Despite its stochastic nature, in the subsequent experiments I observed self-sustaining coherent mechanical oscillation induced by such back-action. The emergence of the coherent oscillation from a static source is reminiscent of unconventional lasing without stimulated emission. The single-electron transistor, pumped by a constant bias, plays the role of a gain medium while the resonator functions as a phonon cavity. Other analogues of laser behaviour, including injection locking, classical squeezing through anharmonicity, and frequency narrowing through feedback, were demonstrated.

These experiments together explored a new paradigm of electromechanics, which might facilitate future fundamental physics research as novel probes at the nanoscale.

Contents

List of Abbreviations **xiii**

1 Introduction **1**
1.1 Quantum transport in mesoscopic systems . . . 3
1.1.1 Single-electron transistors . . . 4
1.1.2 Quantum dots . . . 4
1.2 Constant interaction model of semiconductor quantum dots . . . 5
1.2.1 Single dot . . . 6
1.2.2 Double dot . . . 9
1.3 Nanoelectromechanical systems . . . 11
1.4 Electromechanical coupling in a suspended quantum dot . . . 12
1.4.1 Suspended carbon nanotube device . . . 14
1.5 Quantum limit of continuous measurement . . . 15
1.6 Coherence characterization . . . 17
1.6.1 Autocorrelation functions of stochastic processes . . . 18
1.6.2 Allan deviation . . . 18

2 Engineering RF readout **21**
2.1 Cryogenic measurement circuitry . . . 21
2.2 Calibrating the drive signal . . . 23
2.3 Modeling the tank circuit . . . 25
2.4 SQUID amplifiers . . . 26

3 Measuring carbon nanotube vibrations using a single-electron transistor as a fast linear amplifier **29**
3.1 Introduction . . . 30
3.2 Experiment setup . . . 31
3.3 DC measurements . . . 33
3.4 RF measurements . . . 33
3.4.1 Tank circuit optimization . . . 34
3.5 Displacement sensitivity . . . 34
3.6 The electromechanical measurement sensitivity . . . 39

3.6.1 The electromechanical response function 39
3.6.2 Estimating the displacement imprecision 41
3.6.3 The expected displacement sensitivity 44
3.7 Conclusion 45

4 A coherent nanomechanical oscillator driven by single-electron tunnelling 47
4.1 Introduction 48
4.2 Back-action turns a resonator into an oscillator 51
4.3 Mechanical coherence 54
4.4 Injection locking and anharmonic effects 57
4.5 Stabilisation through feedback 60
4.6 Methods 62
4.6.1 IQ tomography 62
4.6.2 Signal autocorrelation 63
4.6.3 Feedback stabilization 64
4.7 Theory of self-driven oscillations 64
4.7.1 Oscillation mechanism 64
4.7.2 Quantifying the electromechanical coupling 67
4.7.3 Phonon number and minimal linewidth 69
4.7.4 Consequences of anharmonicity 70
4.8 Characterizing the displacement sensitivity 78
4.9 Supplementary data 80
4.9.1 Mechanical linewidth through the oscillation threshold . . . 80
4.9.2 Resonance linewidth 81
4.9.3 Self-oscillation frequency stability 81
4.9.4 Thermal Dependence 84
4.9.5 Further characterization of the emission sidebands 84
4.9.6 Joint histogram of feedback-locked oscillation 86
4.9.7 50 Hz pick-up in the $g^{(2)}$ data 87
4.9.8 Oscillation bistability 87
4.9.9 Strong localization 88
4.10 Conclusion 89

5 Conclusions and outlook 91

Appendices

A Fabrication processes **95**
A.1 Carbon Nanotube synthesis 95
A.1.1 Catalyst preparation 95
A.1.2 Catalyst deposition 95
A.1.3 Chemical vapour deposition 97
A.2 Electrode Base Chip 98
A.2.1 Global marks and bonding pads 99
A.2.2 Local marks 99
A.2.3 Gates 100
A.2.4 Source and drain electrodes 100
A.3 Stamping transfer 100
A.4 Nanotube characterization and recipe optimization 101
A.4.1 Furnace setup 101
A.4.2 Raman spectroscopy 102
A.4.3 Transmission electron microscopy 104

B Autocorrelation functions of intermediate-frequency signals **107**

References **109**

Acknowledgements

I hold the utmost respect and the deepest gratitude to my supervisors, Dr Edward Laird and Prof. Andrew Briggs.

Edward has always been my role model of a well-rounded physicist, from whom I learned everything between principles of research undertaking and scientific presentation. Among his many aphorisms, "Your data is only as clean as your setup." is the one I constantly quote to people. His supervision and practical advices are invaluable.

I want to thank Andrew for guidance and support, for running an excellent lab for and putting together a brilliant group of scientists. From him I learned to look at problems in the big picture. Every time I write an abstract, I start by asking myself how I would present it to Andrew.

It has been a fascinating journey of four years, and I am privileged to have done it in the company of my wonderful colleagues in the Quantum Electronic Devices group at Oxford: Natalia Ares, Tian Pei, Felix Schupp, Matthias Mergenthaler, Reuben Harding, Alex Barbaro, Junjie Liu, Anna Pearson, Sapna Sinha, Dominic Lennon, Wenjing Yan, Hyungil Moon, and Florian Vigeau. Thank you all for the help and input to my research, for the patience when I was an (even more) ignorant new DPhil student, and for all the good laughs in the office.

Over the years, the fellow residents of the 12-14 Parks Road have proven to be indispensable suppliers of advices for scientific challenges outside the cryostats, and for that I thank Tongxin Chen, Ren-Jie Chang, Yuewen Sheng, Nicola Dotti, Michael Slota, Alessandro Lodi, and Xinya Bian.

I am grateful to Neil Young, Alex Robertson, Si Zhou, Jakyung Lee for the help with TEM imaging. And to Paul Pattinson, who is always prompt to respond whenever any clean room equipment malfunctions.

Thanks to all my friends. Oxford would not have been the same without you. And a special one to Sue, for inspiration and aspiration. Shout-out to my fellow midnight gym-goers. It's a comfort to know that I am not the only one stressing out.

This thesis is dedicated to my parents, who have always been so unreservedly supportive to my every decision, encouraging me to aim high. I cannot imagine growing up in a different family, and I won't trade it for the world.

List of Abbreviations

ADC . . . . . Analog-to-digital converter

ADEV . . . . . Allan deviation

CI . . . . . Constant interaction

CNT . . . . . Carbon nanotube

CVD . . . . . Chemical vapour deposition

EBL . . . . . Electron beam lithography

EOS . . . . . Electron-optical system

FET . . . . . Field-effect transistor

HBT . . . . . Heterostructure bipolar transistor

HPF . . . . . High-pass filter

IF . . . . . Intermediate frequency

LHS . . . . . Left-hand side

LO . . . . . Local oscillator

LPF . . . . . Low-pass filter

MEMS . . . . Microelectromechanical systems

MFC . . . . . Mass flow controller

MIBK . . . . . Methyl isobutyl ketone

MOSFET . . . Metal-oxide-semiconductor field-effect transistor

NEMS . . . . . Nanoelectromechanical systems

op-amp . . . . Operational amplifier

PID . . . . . Proportional-integral-derivative (controller)

PMMA . . . . Poly(methyl methacrylate)

QND . . . . . Quantum nondemolition

QPC . . . . . Quantum point contact

RF . . . . . Radio-frequency

RHS . . . . . Right-hand side

RMS . . . . . Root mean square

rpm . . . . . Round per minute

sccm . . . . . Standard cubic centimeters per minute

SEM . . . . . Scanning electron microscope

SET . . . . . Single-electron transistor

SET . . . . . Single-electron tunnelling

SHO . . . . . Simple harmonic oscillator

SQL . . . . . Standard quantum limit

SQUID . . . . Superconducting quantum interference device

SWCNT . . . Single-walled carbon nanotube

TCF . . . . . Time-correlation function

TEM . . . . . Transmission electron microscopy

TG . . . . . Tracking generator

TLS . . . . . Two-level system

VBW . . . . . Video bandwidth

1 Introduction

Contents

1.1 Quantum transport in mesoscopic systems 3
1.1.1 Single-electron transistors 4
1.1.2 Quantum dots 4
1.2 Constant interaction model of semiconductor quantum dots 5
1.2.1 Single dot 6
1.2.2 Double dot 9
1.3 Nanoelectromechanical systems 11
1.4 Electromechanical coupling in a suspended quantum dot 12
1.4.1 Suspended carbon nanotube device 14
1.5 Quantum limit of continuous measurement 15
1.6 Coherence characterization 17
1.6.1 Autocorrelation functions of stochastic processes 18
1.6.2 Allan deviation 18

Nanoelectromechanical system (NEMS) [1] devices are nano-to-micrometer scale mechanical resonators coupled to electronic devices [2]. The mechanical and electrical degrees of freedom of NEMS may interact electrostatically [3–5], magnetostatically [6], electromagnetically [7, 8], and via piezoelectricity [9, 10] or piezoresistivity [11]. This makes possible means of precise measurement and control over the nanomechanical components, which are not only important in their own rights as nontrivial dynamical systems, allowing access to interesting regimes in

fundamental physics, but also envisioned for a variety of applications as fast and ultrasensitive converters between minute mechanical signals and electrical ones [12, 13].

NEMS is a natural evolution from the readily commercialized microelectromechanical system (MEMS), enabled by new fabrication methods derived from semiconductor integrated circuit manufacturing. The latter have already found wide application in commodity products, ranging from gyroscopes in smart phones to microfluid drug delivery pumps [14]. In comparison, NEMS promises to operate at higher speeds whilst consuming less power [15], poising to overtake MEMS in many different applications [16, 17].

This thesis revolves around a particular type of NEMS, i.e., the suspended carbon nanotube resonators. The main body comprises two parts: Chapter 3 describes a novel radio-frequency (RF) readout technique for the mechanical displacement of the nanotube resonator by using an embedded single-electron transistor (SET) as a linear amplifier, and Chapter 4 presents how we used such technique to observe the coherent oscillation of the nanotube that is driven by sequential electron tunnelling through the SET. To preface the more detailed discussions, I shall introduce the scientific background in Chapter 1, and lay out the experimental setup in Chapter 2. The thesis concludes with an outlook for potential development from the presented experiments in Chapter 5.

The interdisciplinary nature of this thesis demands a rather diverse coverage on multiple overlapping topics in physics for the introductory chapter, so I attempt to split it into two branches. In the first branch I adopt a bottom-up philosophy and focus on the device anatomy. I shall begin with the core element of the system that enabled the high precision measurement, i.e., the single-electron transistor, and briefly review the general quantum transport through the SET in Section 1.1-1.2. Then, Section 1.3 accounts for the extra mechanical elements and overview the general applications for NEMS/MEMS devices in science as well as industry. The first branch is completed with the modeling of the electromechanical interaction in Section 1.4. The second branch is concerned with methodologies.

Section 1.5 overviews the physics of RF readout methods, and Section 1.6 covers some prerequisite concepts in metrology.

1.1 Quantum transport in mesoscopic systems

In the early 1980s, the rapid advancement in micro-fabrication technology placed the condensed matter physics community in a position to answer the long-unresolved question: *what happens on the boundary between the macroscopic, classical realm and the microscopic, quantum mechanical one?* A series of demonstrations of macroscopic quantization effect in electrical circuits, most noticeably the discovery of the quantum Hall effect [18], commenced the decades-long endeavour in the study of mesoscopic physics that is still ongoing today [19, 20]. It was then already well-established that the electrical resistance of a quantum conductor is associated with its scattering properties, by the famous Landauer formula [21, 22]:

$$G(\mu) = G_0 \sum_n T_n(\mu) \ , \tag{1.1}$$

where $G(\mu)$ is the electrical conductance at chemical potential μ, $G_0 = e^2/(\pi\hbar) \approx 7.75 \times 10^{-5}\ \Omega^{-1}$ is the conductance quantum, T_n are the transmission eigenvalues of the channels, and the sum runs over all transport channels in the conductor. For this two-probe Landauer–Büttiker single-particle formalism to be true, relevant length scales should meet the following condition [23]:

$$a_0 \ll \lambda_{\mathrm{F}} \lesssim L \lesssim l_0 < l_\phi \lesssim l_{\mathrm{in}} \ , \tag{1.2}$$

where a_0 is the atomic Bohr radius, λ_{F} the Fermi wave length, l_ϕ the coherence length, L the sample length, l_0 the elastic mean free path, and l_{in} the energy relaxation length. That is, the transportation length is much larger than atoms ($a_0 \ll L$), but not large enough for the conduction to be ohmic ($L < l_0$) [24]. Additionally, if $L \ll l_0$, the sample is in the ballistic conduction regime where the carriers travel through the sample with little scattering, so they simply obey Newton's second law of motion at non-relativistic speeds.

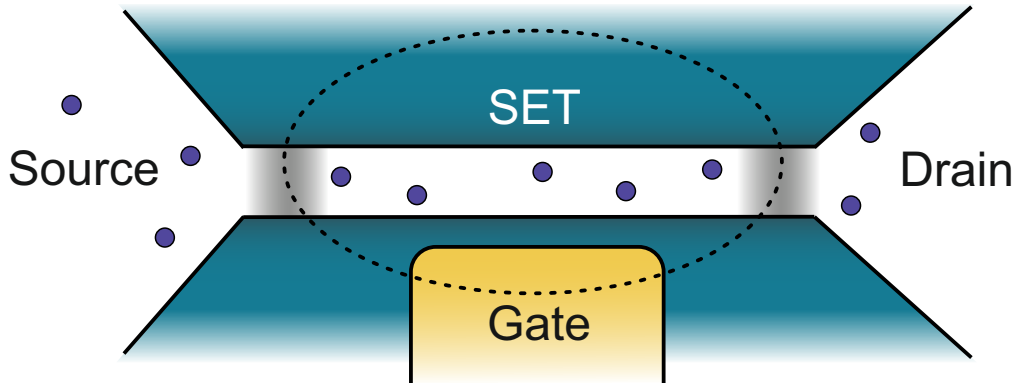


Figure 1.1: Schematic diagram of a single-electron transistor. The purple disks represent electrons, some of which are confined in the SET region defined between the tunnel barriers (grey). Under a finite bias voltage, the electrons may travel through this region sequentially. A tuning voltage can be applied to a nearby conductor (yellow) to adjust the chemical potential in the channel area.

1.1.1 Single-electron transistors

Driven by G. Moore's self-fulfilling prophecy [25], the constant miniaturization of field-effect transistors (FET) eventually, in the late 1980s, reached a regime where the carrier quantization starts to manifest macroscopically. As illustrated in Fig. 1.1, the transistor channel connecting the source and drain reservoirs, often defined between a pair of tunnel barriers [26], is so small that the Coulomb repulsion between carriers results in a finite charging energy E_C to add an extra electron to it. $E_C = e^2/C$ where C is the total capacitance of the isolated channel region. At low temperatures where $k_B T < E_C$, the transistor conductivity becomes sensitive to the gate voltage V_G at the single charge scale, which gives rise to the name single-electron transistor (SET). In addition to the normal carrier depletion over the larger range that applies to transistors of all sizes, electron tunnelling through the SET channel is periodically suppressed by the charging energy, exhibiting a current oscillation as a function of the gate voltage [27, 28]. This phenomenon is known as Coulomb blockade [29], and I will describe it quantitatively in Section 1.2.

1.1.2 Quantum dots

Quantum dots are artificial mesoscopic structures in a solid, comprising $10^3 - 10^9$ atoms and a comparable number of electrons [30–32], the majority of which are

tightly bound. The number of free electrons typically ranges from zero to several thousand. The size and material of quantum dots can vary widely [33]. One common type is the confined two-dimensional electron gas (2DEG) in semiconductor devices [30, 31], especially in III–IV group materials and silicon heterostructures [33–35]. Semiconductor quantum dots hold great promises for photovoltaics, photo emission and detection, with excellent compatibility with modern semiconductor industry, which have been driving intensive study over the past decades [30, 32, 33]. Another major approach is the bottom up design utilizing the myriad types of nanomaterials, including semiconducting nanowires [36–38] or carbon nanotubes [39, 40], self-assembled quantum dots [41], normal metals [42], superconductors [43, 44], ferromagnetic nanoparticles [45], and single molecules trapped between electrodes [46]. The nanomaterial-based quantum dots have demonstrated even stronger quantum confinement.

When a quantum dot is coupled to electrical reservoirs and at least one gate probe is available for tuning the on-dot chemical potential, it becomes a single-electron transistor of nanoscale size. In addition to the charging energy ladder, the strong quantum confinement further induces a discrete spectrum for single electrons with energy spacing $\Delta E = \frac{hv_{\text{Fermi}}}{2L}$, where v_{Fermi} is the Fermi velocity on dot. In this sense a quantum dot is analogous to an artificial atom [32].

More exhaustive studies of few electron quantum transport in a single quantum dot can be found in Refs. [30, 31]. Ref. [32] is concerned with double dots in detail. Ref. [33] focuses on the spins in few-electron quantum dots. Ref. [47] in particular reviews the case of carbon nanotube-based quantum dots.

1.2 Constant interaction model of semiconductor quantum dots

In this section we introduce a minimal model for electrical interactions in single and double quantum dot transistors, the constant interaction (CI) model [48], which accounts for not only the Coulomb interaction but also the discrete energy spectrum due to the quantum confinement. For the sake of simplicity, the CI model makes

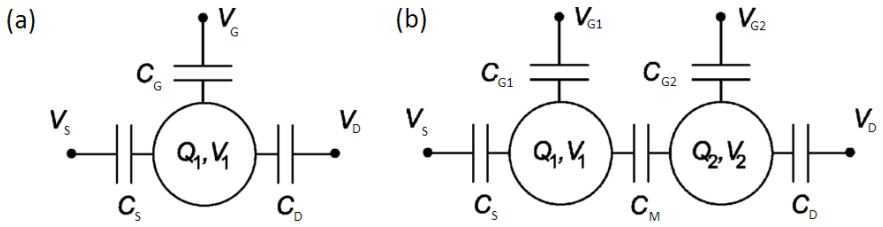


Figure 1.2: Single (a) and double dots (b)(represented by disks) can be modeled as a network of tunnel capacitors. The tunnelling resistances are neglected in this figure. Reproduced with permission from American Physical Society [32].

two assumptions. First, Coulomb interactions between electrons in the dot, and between electrons and environment, are characterized by lumped parameter models as shown in Fig. 1.2. The second assumption is that the single-particle energy-level spectrum is independent of these interactions and therefore independent of the number of electrons on dot. The exact solution to the multiple-electron state in a closed system in general requires solving a many-body Schrodinger equation. However, for the purpose of this thesis, only the sequential tunnelling is relevant and the electron-electron interaction can be omitted, therefore we consider only the single electron states in single and double dot subsequently in this section.

1.2.1 Single dot

We start off with just one single dot. Within the CI model, the source-dot, dot-drain, and gate-dot Coulomb interaction are parameterized via simple, constant capacitances C_{S}, C_{D}, C_{G}, as labeled in Fig 1.2a. The total capacitance of the dot is then defined as $C = C_{\mathrm{S}}+C_{\mathrm{D}}+C_{\mathrm{G}}$. Voltages applied to the source, drain and gate are denoted V_{S}, V_{D}, and V_{G}, respectively. Together they determine the total number N of free electrons in the dot. Without loss of generality, N is taken to be 0 for $V_{\mathrm{G}} = 0$. The energy required to add one electron to level N on a single dot is denoted $E(N)$.

The total energy $U(N)$ of a single dot with N electrons in the ground state is then given by

$$U(N) = \frac{(-|e|N + C_{\mathrm{S}}V_{\mathrm{S}} + C_{\mathrm{D}}V_{\mathrm{D}} + C_{\mathrm{G}}V_{\mathrm{G}})^2}{2C} + \sum_{n=1}^{N} E(n) \ , \tag{1.3}$$

where $-|e|$ represents the free electron charge. The electrochemical potential $\mu(N)$ of the dot is therefore

$$\mu(N) \equiv U(N) - U(N-1) \tag{1.4}$$

$$= (N-1/2)E_{\mathrm{C}} - \frac{E_{\mathrm{C}}}{|e|}(C_{\mathrm{S}}V_{\mathrm{S}} + C_{\mathrm{D}}V_{\mathrm{D}} + C_{\mathrm{G}}V_{\mathrm{G}}) + E(N)\ , \tag{1.5}$$

where $E_{\mathrm{C}} = e^2/C$ is the charging energy. The electrochemical potential contains an electrostatic part (the first two terms) and a chemical part (the last term). The electrochemical potentials are spaced by the addition energy required for an extra electron in the dot:

$$E_{\mathrm{add}}(N) = \mu(N) - \mu(N-1) \tag{1.6}$$

$$= E_{\mathrm{C}} + [E(N) - E(N-1)] = E_{\mathrm{C}} + \Delta E\ . \tag{1.7}$$

In this model, the addition energy consists of electrostatic charging energy E_{C} plus the energy level spacing ΔE.

Now we can move on to the electron transport through the dot. Electron tunnelling depends critically on the alignment of electrochemical potentials of the dot with respect to that in the source μ_S and the drain μ_D. The drain reservoir is conventionally taken to be the electrical ground, i.e. $\mu_D = 0$. Applying a bias voltage $V_{\mathrm{SD}} = V_{\mathrm{S}} - V_{\mathrm{D}}$ to the source electrode opens an energy window of $\mu_S - \mu_D = -|e|V_{\mathrm{SD}}$. For energy levels within the bias window, the electron orbitals in one reservoir are filled whereas those on the other side are empty. If a dot level falls within the bias window, electrons can then tunnel from one reservoir to the other through the dot. Further increasing the bias voltage makes more channels available for tunnelling. In the following subsections we consider the low- and high-bias regimes respectively.

Low-bias regime

In the low-bias limit, the electrochemical levels in the source and drain nearly align. As illustrated in Fig. 1.3a-c, sweeping the gate voltage V_{G} modulates the electrochemical potential in the dot. When the ground state of N enters the bias window (Fig. 1.3b), that is, $\mu_S \geq \mu(N) \geq \mu_D$, one free electron in the source

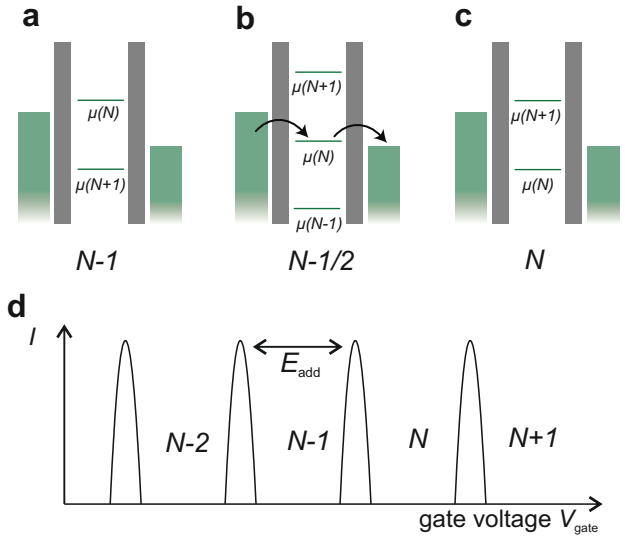


Figure 1.3: (a,c) When $\mu(N)$ is not aligned with the electrode chemical potential, electron tunnelling through the quantum dot will be Coulomb blocked. (b) The blockade will be lifted when $\mu(N)$ falls within the bias window, inducing a peak in tunnel current as a function of gate voltage, as shown in (d).

electrode can tunnel through the barrier into the dot, filling the $\mu(N)$ orbital, and subsequently tunnel from the dot to the drain, hereby leaving the orbital unoccupied again. Further increasing the gate voltage moves $\mu(N)$ out of the bias window and suppresses the tunnelling current, until the gate voltage changes by $E_{\mathrm{add}}/|e|$ and one extra electron is added to the dot to compensate for this change. As a function of the gate voltage, we observe a periodic train of tunnel current maxima as shown in Fig. 1.3d.

High-bias regime

The Coulomb blockade may be alternatively lifted with an increased bias. To highlight the consequent current switching, it is common to plot the differential conductance dI/dV_{SD} as a function of the gate and bias voltage (Fig. 1.4). With a finite bias, conduction is permitted so long as the chemical potential of the N-th electron remains between the Fermi levels in the source and drain. The two extremal cases (in-sets) leads to two sets of parallel straight lines (purple and yellow) in the current plot, of which the slopes are indicative of the mutual capacitances between

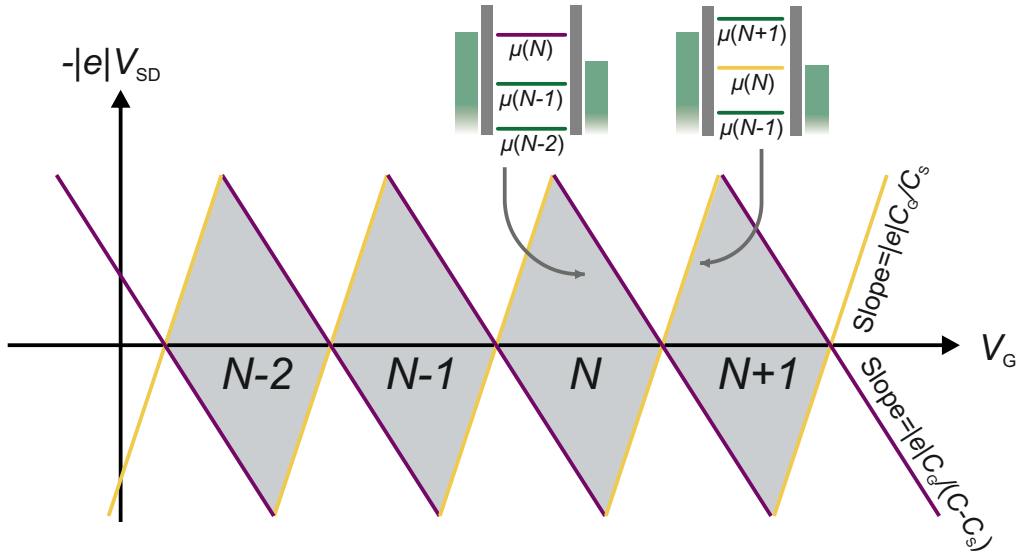


Figure 1.4: Schematic Coulomb diamonds of a high-bias measurement, as explained in Section 1.2.1. Adapted with permission from American Physical Society [33].

the SET and the electrodes, as shown in the figure. Now the tunnelling current is only Coulomb blocked in the light grey rhombus areas, known as the *Coulomb diamonds*.

1.2.2 Double dot

The following subsection reviews the CI model in a double dot, based on the deduction of Ref. [32]. Ignoring cross capacitance, the chemical potential in either site of a double dot (Fig. 1.2b), numbered 1 and 2, may be individually addressed by two separate gates. The tunnel barrier between the dots is modeled as a constant capacitance C_{M}. The total capacitance for each dot is thus $C_{1(2)} = C_{\mathrm{S(D)}} + C_{\mathrm{G1(2)}} + C_{\mathrm{M}}$. With subscript numbers indicting which dot, the respective total charge on dot is defined as $Q_{1(2)}$, and similarly the energy spacing $\Delta E_{1(2)}$, the individual charging energy $E_{\mathrm{C1(2)}}$, and the electrochemical potential $\mu_{1(2)}$. In the weak tunnelling limit, we can ignore hybridization and write the double dot state in the localized-charge basis, (Q_1, Q_2). The total charges are then related to the applied voltages via:

$$\begin{pmatrix} Q_1 + C_{\mathrm{S}}V_{\mathrm{S}} + C_{\mathrm{G1}}V_{\mathrm{G1}} \\ Q_2 + C_{\mathrm{D}}V_{\mathrm{D}} + C_{\mathrm{G2}}V_{\mathrm{G2}} \end{pmatrix} = \begin{pmatrix} C_1 & -C_{\mathrm{M}} \\ -C_{\mathrm{M}} & C_2 \end{pmatrix} \begin{pmatrix} \mu_1 \\ \mu_2 \end{pmatrix} . \tag{1.8}$$

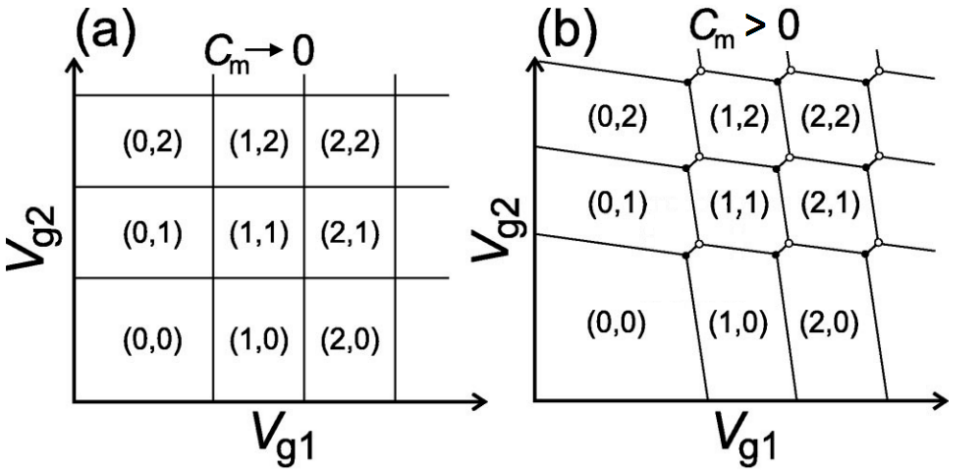


Figure 1.5: Stability diagrams of linear transport when the two dots are (a) completely decoupled (b) weakly coupled. Adapted with permission from American Physical Society [32].

In the low bias limit we assume $V_{\rm S} \approx V_{\rm D} = 0$. Following the same treatment as mentioned in the previous section, we have the electrochemical potential for adding the $N_{1(2)}$th electron to dot 1(2)

$$\mu_1(N_1, N_2) = U_{\rm C}(N_1, N_2) - U_{\rm C}(N_1 - 1, N_2) + \Delta E_1 \tag{1.9}$$

$$= (N_1 - \frac{1}{2})E_{\rm C1} + N_2 E_{\rm CM} - \frac{1}{|e|}(C_{\rm G1}V_{\rm G1}E_{\rm CM} + C_{\rm G2}V_{\rm G2}E_{\rm CM}) + \Delta E_1 \ , \tag{1.10}$$

$$\mu_2(N_1, N_2) = U_{\rm C}(N_1, N_2) - U_{\rm C}(N_1, N_2 - 1) + \Delta E_2 \tag{1.11}$$

$$= (N_2 - \frac{1}{2})E_{\rm C2} + N_1 E_{\rm CM} - \frac{1}{|e|}(C_{\rm G1}V_{\rm G1}E_{\rm CM} + C_{\rm G2}V_{\rm G2}E_{\rm CM}) + \Delta E_2 \ , \tag{1.12}$$

where the electrostatic coupling energy $E_{\rm CM}$ is defined as the change of energy in one dot when an extra electron is added to the other dot.

Eqs. (1.10) and (1.12) relate the electrochemical potential of dot 1 and dot 2 to the voltages applied to the gates, which in turn determine the number of excess electrons on each dot. Hence we can construct a stability diagram at fixed bias [49], giving the equilibrium electron numbers N_1 and N_2 as a function of $V_{\rm G1}$ and $V_{\rm G2}$.

Fig. 1.5a and b are two schematic stability diagrams of the double dot system in the linear transport regime. If coupling energy $E_{\rm CM}$ between the two dots is nearly zero (Fig. 1.5a), the $(V_{\rm G1}, V_{\rm G2})$-phase space is segmented into square domains as a

natural consequence of the periodic potential ladder for both dots. Each horizontal (vertical) line in the diagram separating two equilibrium domains represents a set of (V_{G1}, V_{G2}) configurations that allows one electron to transfer from the source (drain) to dot 1(2) and vice versa, so the system becomes conductive only when the gate voltage configuration are set to the intersection points of two lines such that one electron can tunnel from the source to the drain through both dots.

When the two dots are coupled with finite interaction strength, as shown in Fig. 1.5b, each equilibrium domain becomes hexagonal. The vertices of the square domains split into pairs of *triple points*. The edge connecting each pair of triple points corresponds to the configuration where the potential in both dots are equal. The physical meaning of the other four edges remain the same as their counterparts in Fig. 1.5a, except a change in slopes as a consequence of the mutual capacitances.

1.3 Nanoelectromechanical systems

MEMS's are indispensable components in modern electronics. As of 2010-2017, it is estimated that the annual sales for integrated MEMS accelerometers alone average over 1.4 billion dollars [50]. NEMS/MEMS devices are expected to find commercial applications in mainly four categories [13, 51, 52]: sensors [53–56], actuators [57–60], timing/frequency controllers [61–63], and energy harvesters [64–66], empowering a wide range of applications in industrial R&D, mobile communication, healthcare, and vehicular technologies [67].

On the scientific front, the mechanical degrees of freedom of nanoelectromechanical systems have been demonstrated to dispersively, dissipatively, or parametrically couple to a collection of quantum electronics devices, including embedded single-electron transistors [3–5], quantum point contacts [68, 69], microwave cavities [7, 8], Nitrogen-Vacancy (NV) centers [70, 71], and various optical elements [72–75]. This opens ways to generate non-classical mechanical states via strong coupling [76–78]. O'Connell et al. [79] demonstrated cooling of a mechanical mode to its quantum ground state using a microwave-frequency mechanical oscillator coupled to a qubit, which was used to measure the quantum state of the resonator, and

controllably create single phonons in the resonator. More recently, Ref. [80] demonstrated motional entanglement of the massive oscillators via a microwave resonator. The electromechanical coupling in NEMS might facilitate sensitive measurements in both directions. The quantum electronic elements can be utilized as quantum limited transducers for ultrasensitive motion measurements. Indeed, in this thesis an embedded SET is used to detect the resonator displacement. Alternative efforts towards quantum limited displacement measurements have also used superconducting SETs [4] and microwave resonators [8]. Conversely, the mechanical resonators have been configured to perform dispersive state readout for superconducting qubits [81] and magnetic spin resonance [82]. More thorough reviews of key experiments with micro- and nanoelectromechanical systems can be found in Ref. [83–85].

1.4 Electromechanical coupling in a suspended quantum dot

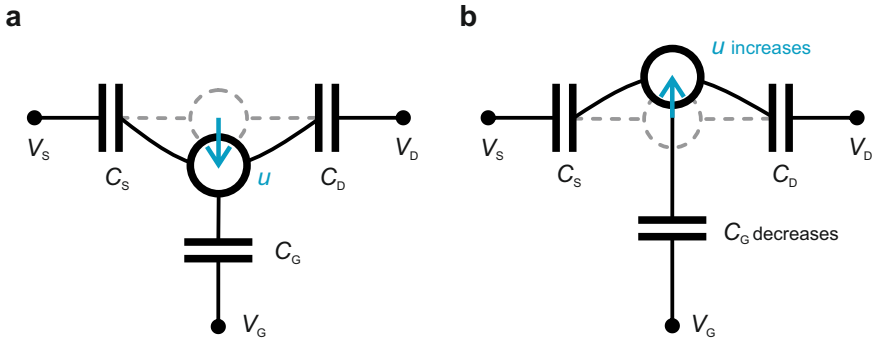


Figure 1.6: Schematics of the electromechanical coupling variation in a suspended quantum dot according to its displacement. (a) When the quantum dot moves to the nearest point to the gate electrode, its gate capacitance C_G is maximized. (b) The quantum dot is displaced by u, moving away from the gate, and the gate capacitance decreases.

Of particular interest to this thesis is the class of NEMS where the mechanical degree of freedom is coupled to an embedded quantum dot, which has been actively studied in the past decades [86–90]. In 2009 Steele et al. [89] observed the strong coupling between single-electron tunnelling through a suspended nanotube and its

nanomechanical motion in a measurement enabled by the record-breaking quality factor. As illustrated in Fig. 1.6, the charge carriers on-dot expecience a static Coulomb force as the resonator displacement modulates the dot-gate capacitance. The electromechanical coupling originates from the extra force exerted on the quantum dot by the additional electron. In the constant-interaction model, the coupling force can be written as

$$F_{\mathrm{EM}} = \frac{eV}{C}\frac{\partial C_{\mathrm{G}}}{\partial u} \tag{1.13}$$

where u is the quantum dot displacement. If we focus on a particular resonance mode of frequency Ω_0, this force can be compared with the quantum zero-point force scale, defined by analogy with the zero-point displacement $u_{\mathrm{ZPM}} \equiv \sqrt{\hbar/2m\Omega_0}$ as $F_{\mathrm{ZP}} \equiv m\Omega_0^2 u_{\mathrm{ZPM}} = \sqrt{\hbar m\Omega_0^3/2}$. This leads to a dimensionless electromechanical coupling parameter defined as [91]:

$$\lambda \equiv \frac{1}{2}\left(\frac{F_{\mathrm{EM}}}{F_{\mathrm{ZP}}}\right)^2 = \frac{F_{\mathrm{EM}}^2}{\hbar m\Omega_0^3}\ . \tag{1.14}$$

The coupling parameter λ can also be interpreted as the ratio between the polaronic energy [92] $E_{\mathrm{p}} \equiv F_{\mathrm{EM}}^2/m\Omega_0^2$ and the phonon energy $\hbar\Omega_0$.

Depending on the coupling strength, classical [93] or quantum mechanical [94] treatment might be applied to the problem. If the electromechanical force is less than the quantum fluctuations, i.e., λ is less than unity, then the device is in the regime of weak coupling and therefore the only relevant value is its expectation at a given displacement. In case of strong coupling, the appropriate framework should be the Born-Oppenheimer approximation [94]. However, as we shall see in Chapter 4, the classical approximation might hold true even for some strong coupling scenarios. My experiments show that if the electrons tunnels through the quantum dot at a much higher rate than the oscillation frequency, we can treat the charge fluctuation as Gaussian [95] and focus only on the mean electrical force as a function of the displacement, which we will model classically in Sec. 4.7.1. Though originally developed for the weak-coupling regime $0 < \lambda \ll 1$ [91, 96], our results show that these classical models give qualitatively accurate predictions beyond that range, when λ approaches or exceeds unity.

1.4.1 Suspended carbon nanotube device

One of the major challenges facing nanoelectromechanical systems is the reduced quality factor due to the increased surface-volume ratio and the resultant damping effects [97, 98]. Carbon nanotubes (CNT) are an amazing material for NEMS in this regard [99] because of the striking contrast between its dimensions and quality factor [53], thanks to its high aspect ratio and tensile strength [15, 88]. As one of the perceivably lightest form nanomechanical resonators, it is expected to achieve quantum ground state of mechanical motion in achievable cryogenic temperatures.

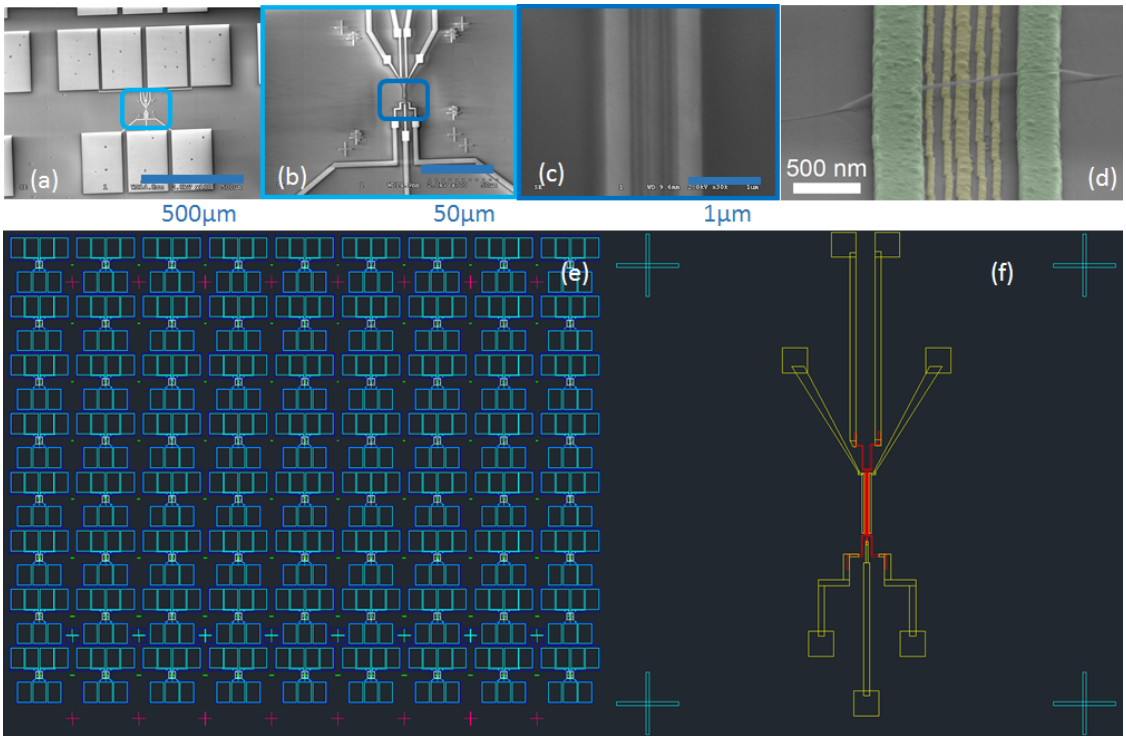


Figure 1.7: Imaging the suspended CNT device under study at different length scales. (a-d) SEM images of a representative CNT device. (d) is false colored to highlight the CNT (grey), the finger gates (yellow), and the source and drain contact electrodes (green). (e) An overview of the chip design. Red: global marks. Blue: bonding pads. (f) Zoom-in of the individual device design. Bonding pads are not shown. The local marks are blue. The gates are red. The source and drain electrodes are yellow. Image (d) courtesy of Dr Tian Pei [100].

Although carbon nanotubes were first discovered by L. V. Radushkevich and V. M. Lukyanovich [101] in 1953, the extensive global study that is still on-going today only commenced after Iijima's famous work [102] in 1991. Soon afterwards it was realized that the perfect combination of remarkable electrical conductance [103], low

mass, and high mechanical compliance [104–107] would render carbon nanotubes a competitive choice of material for NEMS devices. They are the only known form of carbon molecules that exhibit semiconductivity. The electron motion is ballistic over micrometer scales [108–111]. And due to the extremely large tensile strength [104, 105] and elastic modulus [106, 107], suspended carbon nanotubes can be made into mechanical resonators of ultrahigh quality factors [53, 112, 113]. The physical properties of carbon nanotubes are reviewed comprehensively in Ref. [114].

SEM and optical images of the suspended carbon nanotube device under study in the next chapters are shown in Fig. 1.7. By applying DC voltages to the finger gates (yellow in Fig. 1.7d), we can create quantum dots in the middle of the nanotube, thus forming a NEMS by the operation principles mentioned in Sec. 1.4. The fabrication utilizes a nanotube transfer technique [115] such that the nanotube synthesis process does not interfere with the gate electrodes metal deposition. For more details of the fabrication recipe the readers are referred to Appendix A.

1.5 Quantum limit of continuous measurement

Following the derivation of Ref. [116], this section provides a brief introduction to the sensitivity limit for quantum (non-)demolition measurements, and demonstrates the quantum limit in a couple of simple and relevant settings, so as to contextualize the measurement schemes developed later in this thesis in a general framework. The readers are referred to Ref. [116–119] for more in-depth reviews on quantum noise, measurement, and amplification.

Quantum (non-)demolition measurements

The measurement of a quantum state inescapably involves coupling it to one or a cascading series of bigger, classical probes which convert and amplify the quantum signal into our macroscopic world. Such coupling disrupts the quantum states of the system via *measurement back-action*, and thus sets physical limit to the measurement efficiency in various ways. Depending on whether the eigenstates of the observable being measured are stationary, quantum limited measurements

can be categorized into two types: quantum non-demolition (QND) measurements and non-QND measurements.

QND measurement is the optimal repeatable measurement of fundamental practical importance in overcoming the detection deficiency, which has found widespread usage in quantum information processing [120–126] and many other applications. Because the system Hamiltonian commutes with the observable, the back-action does not alter the value of the observable once it is determined, but it still acts on the canonical conjugate, causing the quantum state to dephase at rates exceeding that of information acquisition, which sets the QND quantum limit [116].

The non-stationary observables are directly subject to the back-action noise, which constrain the sensitivities of the non-QND weak continuous measurement from approaching zero. Although there is no limit to the precision of an instantaneous, projective measurement, it is forbidden by Heisenberg's uncertainty principle to continuously track the trajectory of such quantum state, be it microscopic or macroscopic, with infinite sensitivity. Regardless of the measurement schemes, or however hard one might try to eliminate noise in the circuitry, eventually at one point they cannot improve the quantity resolution without disturbing the its quantum state evolution, which accumulates into ever larger error in future instances. In case of a simple harmonic oscillator (SHO), this limit is equivalent to its zero-point motion (ZPM) [116]

$$x_{\mathrm{opt}} = x_{\mathrm{ZPM}} = \sqrt{\hbar/2M\Omega}\ , \tag{1.15}$$

where M is the oscillator mass, Ω its resonance frequency.

Standard quantum limit of a bosonic linear amplifier

The Haus-Caves formulation of the standard quantum limit [116, 127, 128] adopts a basic input/output model for an arbitrary phase-preserving amplifier. For the sake of simplicity for now we are only concerned with a single bosonic mode with a narrow bandwidth centered at ω. Assign photon ladder operators $\hat{a}$ ($\hat{b}$) to the quantum

signal at the input (output) port that obey the usual bosonic commutation relations:

$$[\hat{a}, \hat{a}^\dagger] = 1 \ , \ [\hat{b}, \hat{b}^\dagger] = 1 \ , \tag{1.16}$$

and their symmetrized noise is given by

$$(\Delta a)^2 \equiv \frac{1}{2}\langle\{\hat{a}, \hat{a}^\dagger\}\rangle - |\langle\hat{a}\rangle|^2 \ , \ (\Delta b)^2 \equiv \frac{1}{2}\langle\{\hat{b}, \hat{b}^\dagger\}\rangle - |\langle\hat{b}\rangle|^2 \ . \tag{1.17}$$

Consider the power gain G:

$$\langle\hat{b}^\dagger\hat{b}\rangle = G\langle\hat{a}^\dagger\hat{a}\rangle \ . \tag{1.18}$$

For both Eq. (1.16) and Eq. (1.18) to be true, we therefore must introduce an additive noise $\mathcal{F}$ from the amplifier such that

$$\hat{b} = \sqrt{G}\hat{a} + \hat{\mathcal{F}} \ , \ \hat{b}^\dagger = \sqrt{G}\hat{a}^\dagger + \hat{\mathcal{F}}^\dagger \ , \tag{1.19}$$

which is also assumed to be uncorrelated with the input signal,

$$[\hat{\mathcal{F}}, \hat{a}] = [\hat{\mathcal{F}}, \hat{a}^\dagger] = 0 \ , \ \langle\hat{\mathcal{F}}\hat{a}\rangle = \langle\hat{\mathcal{F}}\hat{a}^\dagger\rangle = 0 \ . \tag{1.20}$$

Substituting these conditions into Eq. (1.16) we have

$$[\hat{\mathcal{F}}, \hat{\mathcal{F}}^\dagger] = 1 - G \ , \tag{1.21}$$

which yields the standard quantum limit of the minimum noise added by a linear amplifier

$$(\Delta b)^2 = G(\Delta a)^2 + \frac{1}{2}\langle\{\hat{\mathcal{F}}, \hat{\mathcal{F}}^\dagger\}\rangle \geq G(\Delta a)^2 + |G - 1|/2 \ . \tag{1.22}$$

In the large gain limit $G \gg 1$ that indicates the quantum limit of added noise is half a photon referred to the input.

1.6 Coherence characterization

Considerable effort in Chapter 4 is dedicated to the discussion on the coherence properties of the nanotube mechanical oscillation, so in this section we review the relevant mathematical concepts and tools [129, 130].

1.6.1 Autocorrelation functions of stochastic processes

In Sec. 4.6.2 we will characterize the coherence of the oscillation signal by calculating its first- and second-order autocorrelation functions, $g^{(1)}(\tau)$ and $g^{(2)}(\tau)$, of not the original signal but its immediate frequency (IF) components. In this section we prove the validity of this somewhat unusual treatment. The first-order autocorrelation function is defined as [131]:

$$g^{(1)}(\tau) \equiv \frac{\langle \boldsymbol{V}_{\mathrm{M}}^{*}(t)\boldsymbol{V}_{\mathrm{M}}(t+\tau)\rangle}{\langle \boldsymbol{V}_{\mathrm{M}}^{*}(t)\boldsymbol{V}_{\mathrm{M}}(t)\rangle}, \tag{1.23}$$

where τ is the delayed time interval, and $\boldsymbol{V}_{\mathrm{M}} = V_{\mathrm{M}}(t)\mathrm{e}^{\mathrm{i}[2\pi f_{\mathrm{M}}t+\phi(t)]}$ the complex voltage of the mechanical signal, $V_{\mathrm{M}}(t)$ and $\phi(t)$ its slowly varying amplitude and a fluctuating phase. The expectation value is averaged over a long time trace.

For signals well above 1 MHz it is harder to directly record it in an analog-to-digital conversion (ADC). In this case the standard route involves first shifting the signal to an intermediate frequency (heterodyning), which is then fed to a square law detector through a narrow band filter to minimize the noise in the unwanted frequency bands [116]. In Chapter 4 I will take an alternative approach, calculating the autocorrelation functions from the intermediate-frequency output from a lock-in amplifier. The validity of such approach is verified in Appendix B.

The second-order correlation function [131] is defined as

$$g^{(2)}(\tau) \equiv \frac{\langle \boldsymbol{V}_{\mathrm{M}}^{*}(t)\boldsymbol{V}_{\mathrm{M}}^{*}(t+\tau)\boldsymbol{V}_{\mathrm{M}}(t+\tau)\boldsymbol{V}_{\mathrm{M}}(t)\rangle}{\langle \boldsymbol{V}_{\mathrm{M}}^{*}(t)\boldsymbol{V}_{\mathrm{M}}(t)\rangle^{2}} \tag{1.24}$$

$$= \frac{\langle V_{\mathrm{M}}^{2}(t)V_{\mathrm{M}}^{2}(t+\tau)\rangle}{\langle V_{\mathrm{M}}^{2}(t)\rangle^{2}} \ . \tag{1.25}$$

For a perfectly coherent source, $g^{(2)}(\tau) = 1$ at all τ, whereas Gaussian chaotic emission has $g^{(2)}(\tau) = 1 + e^{-\pi(\tau/\tau_{\mathrm{coh}})^2}$ [131], where τ_{coh} is a coherent time scale.

1.6.2 Allan deviation

The Allan deviation (ADEV) [132, 133] is a key measure of frequency stability of an oscillation signal on different time scales. We take it that the signal $x(t)$ is sampled by a fast and stable ADC at rate f_{SA}. Relative phase $\theta(t_i)$ within each measurement

interval can therefore be extracted from time trace x_i. Divide the time trace into segments of varying length τ, and the original ADEV is defined as [132]

$$\sigma_{\text{Allan}}(\tau) = \sqrt{\frac{1}{2}\langle(\bar{y}_i - \bar{y}_{i+1})^2\rangle} \tag{1.26}$$

$$\approx \sqrt{\frac{1}{2(N-1)}\sum_{i=1}^{N-1}(\bar{y}_i - \bar{y}_{i+1})^2}\ , \tag{1.27}$$

where the fractional frequency $\bar{y}_i$ is the normalized difference between the temporal frequency in the i-th time slot and the nominal frequency f_{LO}, defined as [132]

$$\bar{y}_i = (\frac{f(t) - f_{\text{LO}}}{f_{\text{LO}}})_{\text{i}} \approx \frac{[\theta(t_{i+1}) - \theta(t_i)]f_{\text{SA}}}{2\pi f_{\text{LO}}}\ . \tag{1.28}$$

To improve the confidence of the resulting stability estimate, especially over longer τ, the original ADEV is often superseded by its overlapping version [134]

$$\sigma_{\text{Allan}}(\tau) = \sqrt{\frac{1}{2M^2(N-2M+1)}\sum_{j=1}^{N-2M+1}\sum_{i=j}^{j+M-1}(\bar{y}_{i+M} - \bar{y}_{i+1})^2}\ . \tag{1.29}$$

2
Engineering RF readout

Contents

2.1 Cryogenic measurement circuitry 21
2.2 Calibrating the drive signal 23
2.3 Modeling the tank circuit 25
2.4 SQUID amplifiers 26

This chapter intends to give a separate and comprehensive review of the design and engineering of the electrical circuits in the cryogenic experiments in Chapter 3 and Chapter 4, so that we might focus on the scientific aspects from here on. All experiments in this thesis were conducted in two dilution refrigerators (Oxford Instrument Triton 200) with almost identical wiring schemes.

2.1 Cryogenic measurement circuitry

As an example, in this section we will walk through the complete measurement circuitry (Fig. 2.1) for Chapter 4. In Chapter 3 I used a similar setup (Sec. 3.2), only without the superconducting quantum interference device (SQUID) amplifier (cf. Sec. 2.4).

The nanotube quantum dot is configured using DC voltages supplied from a Delft IVVI rack. To drive the motion, an RF tone, applied to port 1 of the cryostat,

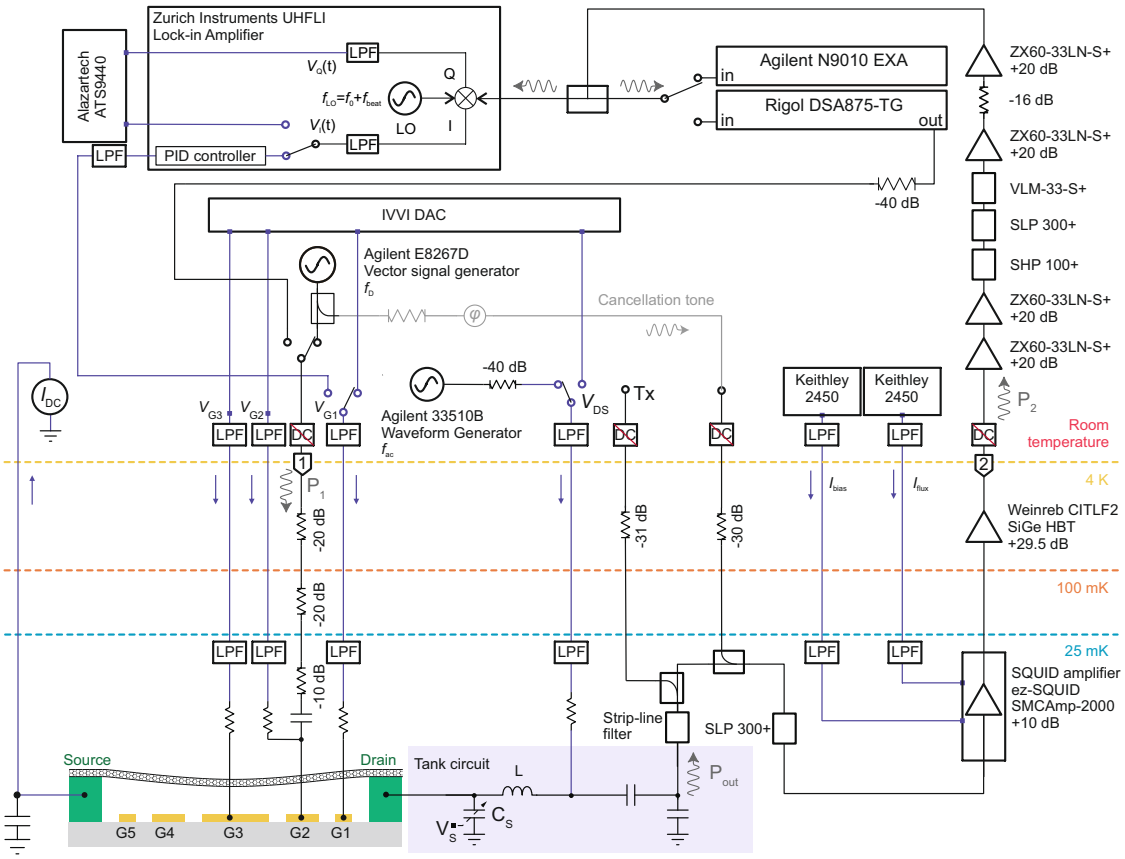


Figure 2.1: Full circuit diagram of the setup, as explained in Section 2.1.

passes via an attenuated coaxial line and a bias tee to gate G2. The DC and RF connection to the sample is separated via a bias tee. Both DC and RF wires were attenuated and low-pass-filtered at various stages of the cryostat, in order to minimize the electrical noise that reaches the sample, as well as to reduce the heat-load by leakage through the wires. The overall cutoff frequency is 350 Hz in the DC lines, and 1 GHz in the RF lines except the one from Port 1. All RF lines are additionally fitted with high-pass filters that cutoff from below 100 kHz.

The DC component of the current through the nanotube is monitored by a current-to-voltage amplifier whose output is acquired by an analog-to-digital converter (ADC, Alazartech ATS9440). The RF component of the current, which is proportional to the nanotube's instantaneous displacement, is transduced to a voltage using a tank circuit and then amplified using a SQUID amplifier (from ez-SQUID [135]) at the cryostat base temperature followed by by a SiGe heterostructure

bipolar transistor amplifier at 4 K. The SQUID is current- and flux- biased using a pair of Keithley 2450 sources. The RF signal, emerging from port 2 of the cryostat, is further amplified and filtered at room temperature before being passed to an RF lock-in amplifier (Zurich Instruments UHFLI) and a spectrum analyser (Agilent N9010EXA) or scalar network analyser input (Rigol DSA875-TG) This RF electromechanical readout is described in Chapter 3, and the SQUID is characterized in Ref. [136].

The transmission measurements of Fig. 3.2 and Fig. 4.2b are performed using the scalar network analyser to inject a tone into port 1 and measure the resulting amplified signal. For self-oscillation measurements (Figs. 4.2c, 4.5, and 4.6), the signal is acquired using the spectrum analyser. For the coherence measurements of Figs. 4.3-4.4, the signal is demodulated by the lock-in amplifier to yield in-phase and quadrature voltages, which are passed to the ADC. For injection locking (Fig. 4.5), the tone is injected at port 1. In this measurement, a phase-shifted cancellation tone is added to the SQUID input to prevent amplifier saturation. For feedback stabilisation (Fig. 4.6), a proportional–integral–derivative controller (PID controller) integrated into the lock-in amplifier is used to apply a feedback voltage (low-pass filtered to 350 Hz) to gate G1. For the frequency-comb experiment of Fig. 4.6e, the oscillating drain-source bias was applied using a waveform generator (Agilent 33510B).

2.2 Calibrating the drive signal

To calibrate the applied drive amplitude, I measure the broadening of the Coulomb peaks as a function of RF power injected into the cryostat through port 1, with the frequency chosen away from the mechanical resonance (Fig. 2.2). Since the measured DC current is a time average over the RF cycle, this broadening is a measure of the RF amplitude at the gate. To quantify it, I first fit the middle peak at the lowest applied power assuming lifetime-broadened Coulomb blockade [48]:

$$I_{\mathrm{DC}} = I_{\mathrm{offset}} + I_0 \frac{(\Gamma_V/2)^2}{(V_{\mathrm{G}} - V_0)^2 + (\Gamma_V/2)^2} \tag{2.1}$$

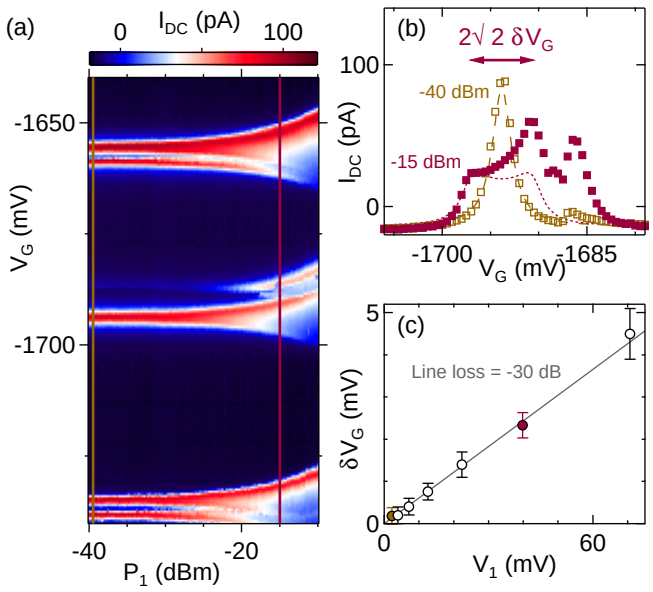


Figure 2.2: Calibrating line attenuation (a) Current through the nanotube as a function of gate voltage and RF drive power into port 1, showing Coulomb peak broadening at high power. (b) Cuts through the central peak at two different drive powers, with fits (cf.Sec. 2.2). The double arrow marks the peak-to-peak drive voltage with -16 dBm applied, which corresponds to the Coulomb peak splitting. The satellite peaks in a and b probably correspond to transport via excited states of the dot. (c) Points: Fitted rms amplitude as a function of drive amplitude. Line: Linear fit. Taking account of the impedance mismatch at the gate, the slope gives the attenuation in the cryostat wiring. Throughout this figure, the drive frequency is $f = 120$ MHz and the bias is $V_{SD} = 1.6$mV.

to extract the intrinsic linewidth $\Gamma_V = 2.3$ mV[1]. Keeping all these parameters fixed, I then fit the peak at each power by convolving Eq. (2.1) with the expected broadening function for a sinusoidal drive:

$$f_P(V_G) = \frac{1}{\pi\sqrt{2\,\delta V_G^2 - V_G^2}}\,\Theta(2\,\delta V_G^2 - V_G^2) \tag{2.2}$$

where the rms drive amplitude δV_G is the fit parameter (Fig. 2.2b) and $\Theta(x)$ is the Heaviside step function.

Plotting the fitted amplitude at the gate against the amplitude V_1 applied at port 1 shows that $\delta V_G = 0.061 \times V_1$ (Fig. 2.2c). Taking account of the impedance mismatch at the end of the signal line, which has the effect of doubling the amplitude on the gate, this implies a line loss of -30 ± 1 dB, as expected from the the nominal

[1]Here the fit parameters I_{offset}, I_0, and V_0 parameterize the offset current, peak current, and location of the Coulomb peak.

−30 dB of the attenuators in the cryostat. This measured line loss is the value used to calibrate δV_G in Chapter 3, and similar procedures were done for Chapter 4.

2.3 Modeling the tank circuit

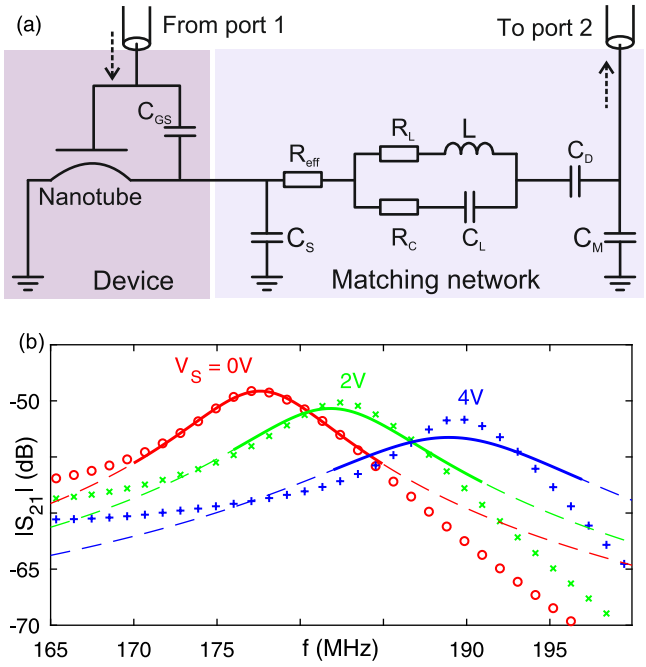


Figure 2.3: Characterization of the tank circuit (a) Lumped element model of the impedance matching tank circuit. For an explanation of component values, see text. The nanotube has a large resistance, and is therefore not included in the model. (b) Electrical transmission from port 1 to port 2, for different settings of the tuning voltage V_S and with $V_{SD} = 0$ mV. Symbols: Data. The main electrical resonance appears as a tuneable transmission peak in the range 178 − 205 MHz. Curves: Fits to an electrical model of the tank circuit. The solid section of each curve indicates the fitting range.

This section explains the tank circuit model, how the model parameters are extracted, and how these lead to the estimate of Z_{trans} used in Eq. (3.30). The impedance matching tank circuit is modelled as shown in Fig. 2.3a. The circuit is constructed from an on-board inductor L, fixed capacitors $C_D = 87$ pF and C_M, and a tunable capacitor C_S. In practice, the circuit also incorporates significant parasitic impedances, which we take account of as follows [137]. The self-resonance and loss of the inductor (Coilcraft 1206CS-221) are modelled by adding a capacitor and resistors as shown, with fixed values given by the component datasheet: $L = 223$ nH, $C_L = 0.082$ pF, $R_C = 25\,\Omega$, and $R_L = K \times \sqrt{f_C}$ with $K = 3.15 \times 10^{-4}\,\Omega/\sqrt{\text{Hz}}$. Dissipation

elsewhere in the circuit is modelled by an effective resistance R_{eff}. The parasitic coupling between the driving gate and the source electrode, which excites the tank circuit independently of the nanotube's motion, is modelled by a capacitor C_{GS}.

The values of the unknown parasitics were estimated by fitting the transmission traces S_{21} from port 1 to port 2 in Fig. 2.3b, measured using a network analyzer at different settings of the varactor tuning voltage V_{S}. The main tank circuit resonance is evident as a broad transmission peak, whose frequency increases as C_{S} is tuned towards lower values. By fitting these traces, we are able to extract the tank circuit parameters.

The trace with $V_{\text{S}} = 0$ V is fitted with the following four free parameters: $C_{\text{S}} = 3.82\,\text{pF}$, $R_{\text{eff}} = 5.04\,\Omega$, $C_{\text{GS}} = 14.5\,\text{fF}$, and $C_{\text{M}} = 80\,\text{pF}$. Although it is possible that other specified component values change substantially at low temperature, in fact these four free parameters lead to good agreement with the data. For the other traces, only the behaviour of the varactor should change, and the fits therefore hold C_{GS} and C_{M} fixed, obtaining fair agreement with the data using only C_{S} and R_{eff} as free parameters. With all parameters in the model circuit of Fig. 2.3 now estimated, the value of the transimpedance Z_{trans} then follows from Kirchoff's laws.

2.4 SQUID amplifiers

The superconducting quantum interference device [138] is the most sensitive detector of magnetic flux available. For decades SQUIDs have been extensively used in a wide-range of low-frequency applications, including susceptometry [139], gravity wave detection [140], magnetic resonance imaging [141], biomagnetism [142], and more recently, as fundamental building blocks in quantum information processing [143–145]. The SQUID excels in these applications because of its low power dissipation and noise properties.

A typical microstrip SQUID amplifier (Fig. 2.4a) loads the input voltage to a thin-film superconductor coil (brown), which is magnetically tightly coupled to the SQUID washer (purple) below. As illustrated in Fig. 2.4b, the coil converts the input voltage V_{i} into a current I_{i}, which induces a change in the total flux threading

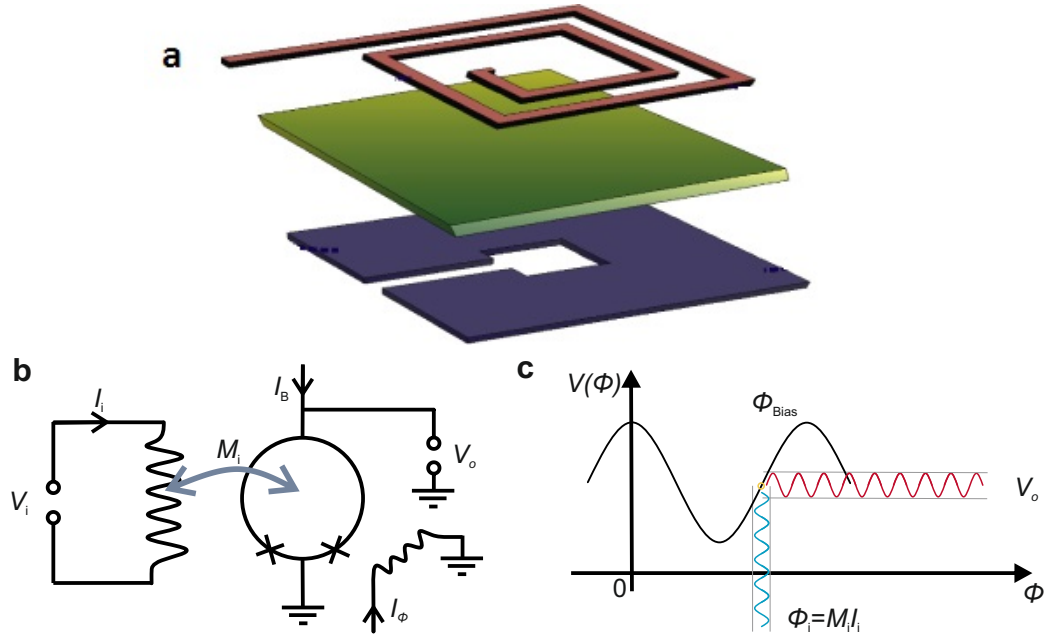


Figure 2.4: (a) Schematics of a microstrip SQUID amplifier. The superconductor coil (brown) is separated from the SQUID washer (purple) by an insulating film (green). (b) Electrical configuration of a DC SQUID. (c) The oscillation of the total voltage drop $V(\Phi)$ across the SQUID as a function of the total flux bias Φ. Adapted from Ref. [146].

the SQUID. This in turn modulates the the voltage drop across the SQUID, hence generating the output voltage V_o. To maximize the voltage amplification, a small wire-wound coil is used to offset the static flux such that the operation point (yellow) is at the steepest slope in Fig. 2.4c.

3

Measuring carbon nanotube vibrations using a single-electron transistor as a fast linear amplifier

Contents

3.1 Introduction 30
3.2 Experiment setup 31
3.3 DC measurements 33
3.4 RF measurements 33
3.4.1 Tank circuit optimization 34
3.5 Displacement sensitivity 34
3.6 The electromechanical measurement sensitivity 39
3.6.1 The electromechanical response function 39
3.6.2 Estimating the displacement imprecision 41
3.6.3 The expected displacement sensitivity 44
3.7 Conclusion 45

In this chapter we demonstrate sensitive and fast electrical measurements of a carbon nanotube mechanical resonator. The nanotube is configured as a single-electron transistor, whose conductance is a sensitive transducer for its own displacement. Using an impedance-matching circuit followed by a cryogenic amplifier, the vibrations can be monitored at radio frequency. The sensitivity of this continuous displacement measurement approaches within a factor 470 of

the standard quantum limit.

3.1 Introduction

Suspended carbon nanotubes are mechanical resonators [88] with low mass, high compliance, and high quality factor [53, 112], which makes them sensitive electromechanical detectors for tiny forces [147] and masses [54, 148, 149]. The time-averaged current through a vibrating nanotube probes electron-phonon coupling [89, 150–152], non-linear dissipation [153], and mechanical mode mixing [154] on the nanoscale. Time-resolved measurements go further, allowing for the study of transient effects such as spin switching [155, 156], mechanical dephasing [157], or even force-detected magnetic resonance [158]. Although the low mass favours large electromechanical coupling, the large electrical impedance of nanotube devices makes it difficult to amplify the current signal with high sensitivity and bandwidth, especially since low temperatures are needed to suppress thermal noise.

One approach is to down-convert the electromechanical signal to a frequency within the bandwidth of a cryogenic current amplifier, using either two-source mixing or the non-linear conductance of the nanotube itself [159, 160]. For fast measurements, parasitic capacitance must be minimised by placing the amplifier close to the resonator. The resulting heat load has usually prevented operation below 1 K [157, 160], although recently such a setup achieved high sensitivity at millikelvin temperatures and with a bandwidth of 87 kHz [161]. A second approach, with higher bandwidth, is to detect the changing capacitance between the vibrating nanotube and a pickup antenna [162]. However, the small size of the pickup antenna means that a large electric field is needed to generate an appreciable signal. A third approach, used for other kinds of nanoscale resonator [163, 164], is to connect the resonator's output directly to a fast amplifier matched to the cable impedance (typically 50 Ω). However, the electrical divider formed between the large impedance of the device and the small impedance of the cable degrades the signal.

Here, we demonstrate a circuit that combines sensitivity with high speed by monitoring the electromechanical signal directly, while requiring only a DC bias

voltage. The circuit exploits a single-electron transistor (SET) defined within the nanotube as the initial stage of displacement amplification [3, 4, 89, 112, 151, 152, 165, 166]. The SET output current, which depends linearly on displacement, is monitored directly at radio frequency using a low-noise cryogenic radio-frequency (RF) amplifier with MHz bandwidth. To improve the coupling between the SET and the cryogenic amplifier, we use an impedance-matching stage based on a tuneable RF tank circuit [137]. We characterize the displacement imprecision achieved in this setup and show that it approaches within a factor 470 of the limit set by quantum mechanics. This technique combines the speed allowed by RF readout with the high sensitivity of an SET amplifier integrated into the moving nanotube.

3.2 Experiment setup

The experimental setup is shown in Fig. 3.1a. The resonator is fabricated by stamping a carbon nanotube across lithographically patterned Cr/Au contact electrodes, giving a suspended length of $l = 800$ nm [115, 167, 168]. Beneath the nanotube, five predefined Cr/Au finger gates, labelled G1-5, allow tuning of the electrical potential along the nanotube. This device is bonded to a printed circuit board and loaded into a 25 mK dilution refrigerator. For electromechanical excitation, gate G2 is connected via a bias tee to an RF drive line (port 1 in Fig. 3.1a), and is driven either by a RF signal generator or using the output of a network analyzer.

With the drain electrode held at ground, a source-drain bias V_{SD}, applied to the source electrode, drives a current through the nanotube which can be measured both at DC and at RF. The DC current I_{DC} is monitored using a room-temperature current amplifier connected to the drain. The RF response is measured using a cryogenic amplifier anchored at 5 K inside the cryostat. A resonant tank circuit (Fig. 3.1a right), constructed using chip inductors and capacitors on the circuit board and bonded to the source electrode, is interposed between the device and the amplifier to transduce the RF current through the nanotube to an output voltage V_{out}, which is fed to the cryogenic amplifier [162]. This amplified signal is fed via

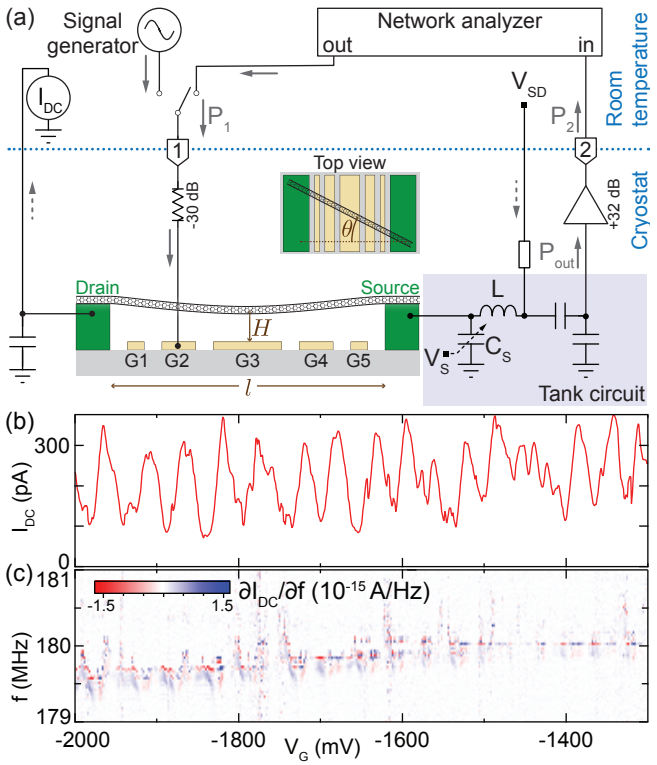


Figure 3.1: **a** Device and measurement setup. The vibrating nanotube is suspended between source and drain electrodes and over five gate electrodes that define a quantum dot potential. Gate 2 is connected to an attenuated high-frequency line for mechanical actuation. The device is biased by voltage V_{SD} and measured both via DC transport and via a tuneable RF circuit (see text). The DC current path is marked by dashed arrows, the RF path by solid arrows. The length l and suspended height H of the nanotube are indicated in the main diagram, and an inset marks the alignment angle θ. **b** Coulomb blockade peaks measured in DC current as a function of DC voltage V_G on gate 2, with $V_{SD} = 5$ mV. **c** Characterization of the mechanical resonance in transport. With RF power applied at frequency f, the derivative $\partial I_{DC}/\partial f$ shows the resonance as a weakly gate-dependent feature at $f \sim 180$ MHz. The RF power at port 1 was $P_1 = -35$ dBm, and the bias was $V_{SD} = 5$ mV. In panels **b** and **c**, the other gate voltages were held at positive voltages between 0 and 300 mV.

port 2 of the cryostat into the network analyzer. The tank circuit incorporates a variable capacitor C_S, controlled with a tuning voltage V_S, which adjusts the electrical resonance frequency [137].

To allow sensitive electromechanical measurements, the suspended nanotube is operated as an SET. This SET is formed between the Schottky barriers along the nanotube and tuned using DC voltages applied to the finger gates [47, 169]. Figure 3.1b plots the DC current I_{DC} through the nanotube as a function of the DC voltage V_G applied to gate G2. The pattern of current peaks indicates Coulomb

blockade, confirming SET behaviour.

3.3 DC measurements

We first identify the mechanical resonance using DC transport. With an RF drive at frequency f applied to gate G2, Fig. 3.1c shows the derivative $\partial I_{\mathrm{DC}}/\partial f$ as a function of f and V_{G}. The current has a sharp peak or dip when f matches the mechanical resonance frequency f_{M}, leading to a feature in the derivative [88, 112] appearing around $f_{\mathrm{M}} \approx 180$ MHz. The resonance frequency increases with increasing V_{G} as the mechanical tension changes. It is also modulated by Coulomb blockade, because electron tunnelling modifies the effective spring constant [89, 151].

3.4 RF measurements

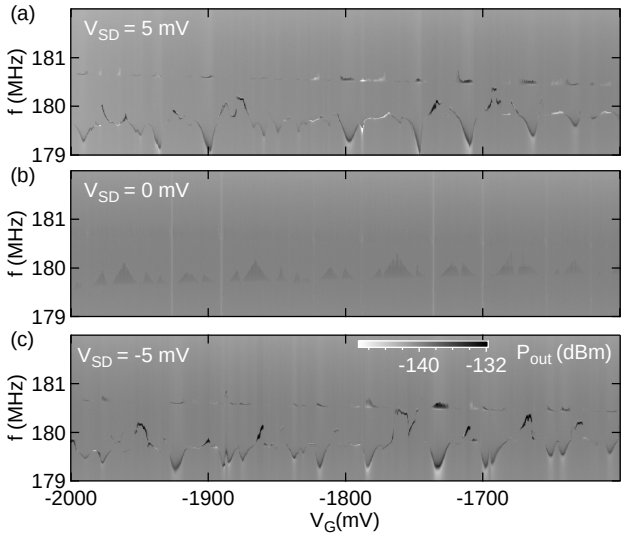


Figure 3.2: Characterization of the mechanical resonance. Transmitted signal, converted to tank circuit output power P_{out}, as a function of frequency and gate voltage for different settings of V_{SD}. Here $V_{\mathrm{SD}} = 0$ V and drive power is $P_1 = -70$ dBm. The main mechanical resonance is evident as a sharp feature in panels **a** and **c**, whose frequency varies with gate voltage because of Coulomb blockade. A weaker resonance appears at slightly higher frequency. This may be a mode vibrating approximately in the plane of the sample, i.e. orthogonal to the stronger resonance, and is not studied further.

3.4.1 Tank circuit optimization

We now turn to RF measurements. To optimise the sensitivity, we first tune the tank circuit's electrical resonance frequency f_E to a value near f_M by tuning the varactor voltage V_S (See Sec. 2.3). In this Chapter, we fix $V_S = 0$ V, giving optimum sensitivity around $f_E \approx 178$ MHz and a detection bandwidth of ≈ 8 MHz, set by the electrical quality factor.

The mechanical signal appears as a sharp resonance superimposed on the electrical transmission peak when a source-drain bias V_{SD} is applied. This is evident in Figs. 3.2(a-c), which show the power P_{out} transmitted from the output of the tank circuit, plotted as a function of frequency and gate voltage. This signal arises because the motion of the nanotube relative to the gates modulates the SET conductance, leading to a current oscillating at the vibration frequency. This current is transduced to an RF output voltage V_{out}, with $P_{out} = V_{out}^2/Z_0$, where $Z_0 = 50\ \Omega$ is the line impedance. As expected from this mechanism, the signal appears for both positive and negative bias (Fig. 3.2a,c), but nearly vanishes at zero bias (Fig. 3.2b). The fact that the signal is larger with a bias applied confirms that it arises mainly from the SET conductance. The weak signal remaining at zero bias indicates a small capacitive contribution [162]. We interpret this mode as the fundamental out-of-plane flexural mode.

3.5 Displacement sensitivity

We now characterize the displacement sensitivity. We do this by measuring the signal and the noise of the output voltage when the nanotube is driven to a fixed displacement amplitude, by adding a known oscillating gate voltage δV_G to V_G. This measurement is performed with the gate voltage tuned to the flank of a Coulomb blockade peak (Fig. 3.3a). As expected, this gate voltage leads to a strong mechanical signal (Fig. 3.3b).

Both signal and noise are extracted from Fig. 3.3c, which shows the power spectrum P_{out}, measured with root-mean-square driving amplitude $\delta V_G = 1.3\ \mu$V

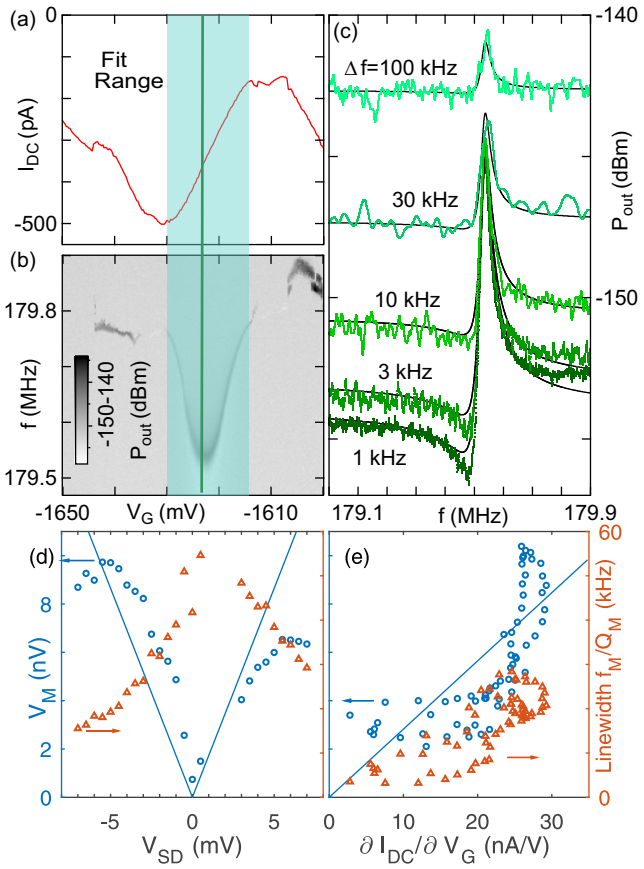


Figure 3.3: Measuring the displacement sensitivity **a** DC current as a function of gate voltage in the region of one Coulomb blockade peak, with $V_{\mathrm{SD}} = -5$ mV. **b** Mechanical resonance measured in RF power simultaneously with **a**. **c** Transmission as a function of frequency, measured with gate excitation voltage $\delta V_{\mathrm{G}} = 1.2$ μV and for different settings of the network analyzer's resolution bandwidth RBW. Points: data; Curves: fits to Eq. (3.1). Measurements are taken on the flank of the Coulomb blockade peak (vertical line in a-b). **d** Mechanical signal(circles, left axis) and linewidth (triangles, right axis) as functions of bias. Line: Fit of the form $V_{\mathrm{M}} \propto |V_{\mathrm{SD}}|$. **e** The same quantities as functions of transconductance. Line: Fit of the form $V_{\mathrm{M}} \propto \partial I_{\mathrm{DC}}/\partial V_{\mathrm{G}}$.

and for different settings of the network analyzer's resolution bandwidth Δf. The mechanical resonance is evident at frequency $f_{\mathrm{M}} \approx 179.55$ MHz. Whereas a purely mechanical response would lead to a symmetric Lorentzian peak, the observed peak is asymmetric, indicating a small contribution from stray electronic transmission in the sample holder. To extract the mechanical signal strength, we fit these traces with the following function, which takes account of the resonant mechanical response, a non-resonant electrical background, and broadband detection noise (see Sec. 3.6.1):

$$P_{\mathrm{out}}(f) = \frac{A^2}{Z_0}\left|Be^{i\phi_B} + \frac{f_{\mathrm{M}}^2/Q_{\mathrm{M}}}{f_{\mathrm{M}}^2 - f^2 + i\frac{f f_{\mathrm{M}}}{Q_{\mathrm{M}}}}\right|^2 \delta V_{\mathrm{G}}^2 + \frac{S_{VV}\Delta f}{Z_0}, \tag{3.1}$$

where $Z_0 = 50\ \Omega$ is the line impedance, Q_M is the mechanical quality factor, S_{VV} is the one-sided spectral density of the system voltage noise, Δf is the resolution bandwidth, and A, B, and ϕ_B are constants. By fitting Fig. 3.3c to Eq. (3.1), using f_M, Q_M, S_{VV}, A, B, and ϕ_B as global fit parameters, we find a voltage sensitivity $\sqrt{S_{VV}} = 50.3 \pm 0.5\ \mathrm{pV}/\sqrt{\mathrm{Hz}}$ and a quality factor $Q_\mathrm{M} = 6000 \pm 1500$. From Fig 3.3b, it is clear that the linewidth varies strongly with gate voltage across the Coulomb peak, which implies that the quality factor is limited by dissipation due to inelastic electron tunnelling [89, 151]. The fitting function does not take account of possible mechanical non-linearity, which is justified by the good quality of the fits in Fig. 3.3c. We have also confirmed that this drive amplitude is below the observable onset of Duffing distortion of the lineshape, and is also below the onset of power-broadening [170].

On resonance, the purely electromechanical part of the signal in Fig. 3.3c is:

$$V_\mathrm{M} = A\,\delta V_\mathrm{G} \tag{3.2}$$

$$= 8.79 \pm 0.08\ \mathrm{nV}. \tag{3.3}$$

To quantify the sensitivity, we must relate this output voltage amplitude to the corresponding displacement u. The displacement depends on the driving force δF via:

$$u = |\chi_\mathrm{M}(f)|\,\delta F \tag{3.4}$$

$$= |\chi_\mathrm{M}(f)|\,V_\mathrm{G}\frac{\partial C_2}{\partial u}\,\delta V_\mathrm{G}. \tag{3.5}$$

where where C_2 is the capacitance between the gate and the nanotube. Here $\chi_\mathrm{M}(f) \equiv \frac{1}{4\pi^2 m}[f_\mathrm{M}^2 - f^2 + i\frac{f f_\mathrm{M}}{Q_\mathrm{M}}]^{-1}$ is the mechanical susceptibility [171] at driving frequency f, and m is the mass. The force is $\delta F = V_\mathrm{G}\frac{\partial C_2}{\partial u}\,\delta V_\mathrm{G}$. We must therefore estimate the parameters in Eq. (3.5). This is complicated by the uncertainty in the nanotube's mass, its diameter, and in the suspended height above the gate, which affects the capacitance derivative. The full estimation procedure is described in Sec. 3.6. Using the known gate capacitance $C_2 \approx 3.3 \pm 0.6$ aF, extracted from a Coulomb blockade measurement similar to Fig. 3.1b, we use finite-element electrostatic simulation to deduce that the height is $H = 18^{+92}_{-13.5}$ nm. Combining this

value with the nanotube diameter $D = 4.5 \pm 1.5$ nm, estimated from transmission electron microscopy, leads to a capacitance derivative $\partial C_2/\partial u = 49.4^{+271}_{-40.5}$ pF m^{-1}. The error range is dominated by the uncertainty in the suspended height and suspension angle θ. The nanotube's mass is $m = 21.3^{+81}_{-15.5}$ ag, with the uncertainty arising from the unknown number of walls and from the suspension angle θ.

Substituting these quantities into Eq. (3.5) allows us to calculate that in Fig. 3.3c the mechanical amplitude is $u = 25.2^{+811}_{-24.3}$ pm. The proportionality constant between the signal voltage (Eq. (3.3)) and the corresponding displacement is therefore known, finally leading to a displacement sensitivity, defined as the square root of the measurement imprecision:

$$\sqrt{S_{uu}} = \frac{u}{V_\mathrm{M}}\sqrt{S_{VV}} \tag{3.6}$$

$$= 144^{+4700}_{-139}\ \mathrm{fm}/\sqrt{\mathrm{Hz}}. \tag{3.7}$$

The large range of this estimate reflects the combination of uncertainties entering Eq. (3.5).

In this model, the electromechanical signal V_M should increase with $|V_\mathrm{SD}|$, because a larger bias leads to a larger mechanically modulated current. This is tested in Fig. 3.3d, which plots V_M against V_SD. As expected, the signal is approximately proportional to bias. At high bias, the signal falls below the trend because the SET Coulomb peaks become less sharp. The electromechanical signal should also be proportional to the SET transconductance $\partial I_\mathrm{DC}/\partial V_\mathrm{G}$. This is tested in Fig. 3.3e, which plots V_M against transconductance at fixed bias. The data show approximate proportionality, again confirming that the signal arises mainly from conductance through the SET.

We now compare the experimental displacement sensitivity with what would be achieved by a quantum-limited detector [4]. In a continuous phase-preserving measurement, minimum uncertainty requires the imprecision noise to be equal to the noise generated by backaction. In this ideal case, the displacement sensitivity

obeys the standard quantum limit (SQL) [8, 116]:

$$\sqrt{S_{uu}(\mathrm{SQL})} = \sqrt{\frac{\hbar Q_{\mathrm{M}}}{4\pi^2 m f_{\mathrm{M}}^2}} \tag{3.8}$$

$$= 4.8^{+5.5}_{-2.9}\ \mathrm{fm}/\sqrt{\mathrm{Hz}}. \tag{3.9}$$

Comparing Eq. (3.9) with Eq. (3.7) gives the normalised sensitivity:

$$\frac{\sqrt{S_{uu}}}{\sqrt{S_{uu}(\mathrm{SQL})}} = 30^{+440}_{-27} \tag{3.10}$$

meaning that this measurement is within a factor 470 of the SQL, and may in fact surpass it. A larger mass than estimated, for example because of surface contamination, would imply smaller sensitivity relative to the SQL; a geometry in which the nanotube sags close to the gate implies a larger sensitivity but still within the range of Eq. (3.1). The uncertainty could be reduced by calibrating the displacement using a measurement of Brownian motion. Imprecision below the SQL is possible if measurement backaction excites the resonator out of its ground state [116].

In fact, some backaction is evident in Fig. 3.3b, which shows that the gate voltage range with the strongest signal also leads to a broader mechanical resonance. Figure 3.3e confirms this by plotting the mechanical linewidth against transconductance, showing that higher transconductance, and therefore stronger measurement, correlates with a broader line. This is because the fluctuating occupation of the SET creates a stochastic force which reduces the mechanical quality factor [5, 172]. However, the dependence on source-drain bias is opposite (Fig. 3.3d). Both behaviors have been explained by considering the damping mechanism[173]. Electromechanical damping occurs when the changing displacement brings the SET's chemical potential alternately above and below the Fermi level in one of the leads, so that electrons preferentially tunnel onto the SET with low energy and off with high energy. This damping is reduced by detuning the quantum dot chemical potential from one or both Fermi levels. In the situation of this measurement, where the bias is large compared to both the thermal energy and lifetime broadening, this detuning is achieved by separating the two Fermi levels with a source-drain bias (Fig. 3.3d) or by tuning the

SET chemical potential between the Fermi levels with a gate voltage (Fig. 3.3e). This behaviour has been previously observed and modelled quantitatively[172]. At zero bias, occupation fluctuations create mechanical backaction without contributing to the signal. Increasing the bias therefore increases the efficiency of the measurement, allowing the SQL to be approached more closely. This description ignores the effect of transport resonances and energy-dependent tunnelling, which lead to more complex backaction even including negative damping[173]. A more complete theory of this RF displacement sensor would need to include these effects to assess the potential for quantum-limited measurement.

Finally we consider what limits the achieved displacement imprecision given by Eq. (3.7). The imprecision is approximately as expected given the noise of the cryogenic amplifier (see Sec. 3.6.3), and could therefore be improved by using an improved superconducting amplifier [146]. Alternatively, the conversion of displacement to current could be improved with larger DC gate voltage, while increasing the quality factor of the tank circuit could give larger transimpedance. Ultimately, the sensitivity will be limited by the SET's shot noise [174, 175].

3.6 The electromechanical measurement sensitivity

In this section, we explain how the response curves of Fig. 3.3c are fitted, and how the fit parameters lead to an estimate of the displacement sensitivity. In Section 3.6.1 we derive the fit function. Section 3.6.2 uses the fit parameters to deduce the sensitivity, including error bars. Section 3.6.3 estimates what sensitivity should be expected given the circuit parameters.

3.6.1 The electromechanical response function

The signal $V_{\rm out}$ (see Fig. 3.1a) arises because the motion excites an oscillating current I through the nanotube and onto the source electrode, and the tank circuit transduces this current to an output voltage $V_{\rm out}$. Here, we show that the

corresponding output power is described by Eq. (3.1). The output is related to the current by the circuit's transimpedance [137]

$$Z_{\rm trans}(f) = V_{\rm out}/I. \tag{3.11}$$

With a drive signal $\delta V_{\rm G}$ at frequency f applied to the gate, the output is therefore

$$V_{\rm out}(f) = Z_{\rm trans}(f)I + \xi(f)\delta V_{\rm G} + V_{\rm N}. \tag{3.12}$$

where the first term describes the electromechanical signal, the second term describes the effect of stray signal paths (parameterized by a coupling constant $\xi(f)$), and the third term describes electrical noise. Both $Z_{\rm trans}(f)$ and $\xi(f)$ depend on frequency.

The current I contains two terms: a contribution from transport through the nanotube, proportional to the displacement u; and a contribution proportional to the velocity $\dot{u}$, arising because the motion modulates the gate capacitance:

$$I = \frac{\partial I}{\partial u}u + \frac{\partial q}{\partial u}\dot{u} \tag{3.13}$$

$$= \frac{\partial q}{\partial u}\left(\frac{1}{C_2}\frac{\partial I}{\partial V_{\rm G}}u + \dot{u}\right) \tag{3.14}$$

where $q \equiv \sum_k C_k V_k$ is the charge induced on the quantum dot [29] by the nearby electrodes. Here the index k labels the electrodes, each set to voltage V_k and coupled to the quantum dot by capacitance C_k. In previous work[137], where the tank circuit was connected to a gate electrode, the transport contribution was zero ($\partial I/\partial V_{\rm G} = 0$), but here it is the largest part of the signal.

We now assume a linear mechanical response as in Eq. (3.1), so that the displacement is related to the driving signal by

$$u(f) = \chi_{\rm M}(f)\, C_2' V_{\rm G}\, \delta V_{\rm G}, \tag{3.15}$$

where $\chi_{\rm M}(f) = \frac{1}{4\pi^2 m}[f_{\rm M}^2 - f^2 + i f f_{\rm M}/Q_{\rm M}]^{-1}$ is the mechanical susceptibility, and a prime denotes a derivative [1] with respect to u. Taking the Fourier transform of Eq. (3.14) and inserting into Eq. (3.12) gives for the output signal:

$$V_{\rm out}(f) = \hat{A}\left(\hat{B} + \frac{f_{\rm M}^2/Q_{\rm M}}{f_{\rm M}^2 - f^2 + i\frac{f f_{\rm M}}{Q_{\rm M}}}\right)\delta V_{\rm G} + V_{\rm N} \tag{3.16}$$

[1] Displacement u is defined towards the substrate, so that C' is positive.

where we define the complex parameters:

$$\hat{A} \equiv \frac{Z_{\rm trans}(f_{\rm M}) q' C_2' V_{\rm G} Q_{\rm M}}{4\pi^2 m f_{\rm M}^2} \left(\frac{1}{C_2} \frac{\partial I}{\partial V_{\rm G}} + 2\pi i f_{\rm M} \right) \tag{3.17}$$

$$\hat{B} \equiv \xi(f_{\rm M})/\hat{A}, . \tag{3.18}$$

The derivative of the induced charge is

$$q' = \sum_k C_k' V_k, \tag{3.19}$$

with the sum running over gate electrodes only since the source and drain electrodes are held near zero potential. Henceforth we take $\hat{A}$ and $\hat{B}$ as constants because the frequency dependence of the electrical circuit is weaker than the frequency dependence of the mechanical response.

The fitting function for Fig. 3.3c is obtained by converting the voltage of Eq. (3.16) into a detected power:

$$P_{\rm out}(f) = |V_{\rm out}(f)|^2/Z_0 \tag{3.20}$$

$$= \frac{A^2}{Z_0} \left| B e^{i\phi_B} + \frac{f_{\rm M}^2/Q_{\rm M}}{f_{\rm M}^2 - f^2 + i\frac{f f_{\rm M}}{Q_{\rm M}}} \right|^2 \delta V_{\rm G}^2 + \frac{S_{VV}\Delta f}{Z_0} \tag{3.21}$$

where $Z_0 = 50\ \Omega$ is the line impedance, S_{VV} is the voltage noise one-sided spectral density, and Δf is the resolution bandwidth of the network analyser. We have defined $A \equiv {\rm Re}\{\hat{A}\}$, $B \equiv {\rm Re}\{\hat{B}\}$, and $\phi_{\rm B} \equiv \arg\{\hat{B}\}$. This is Eq. (3.1), with fit parameters $f_{\rm M}$, $Q_{\rm M}$, A, B, ϕ_M, and S_{VV}.

3.6.2 Estimating the displacement imprecision

To calculate the displacement imprecision, we must estimate the parameters appearing in Eq. (3.5), repeated here:

$$u = \frac{1}{4\pi^2 m} \left| \frac{1}{f_{\rm M}^2 - f^2 + i\frac{f f_{\rm M}}{Q_{\rm M}}} \right| V_{\rm G} C_2' \, \delta V_{\rm G}. \tag{3.22}$$

For the data of Fig. 3.3c, we estimate these as follows:

- The parameters $f_{\rm M} = 179.53 \pm 0.03$ MHz and $Q_{\rm M} = 6000 \pm 1500$ are deduced by fitting Fig. 3.3c.

Parameter		Estimate		Unit	Method
		High imprecision	Best	Low imprecision	
Mechanical frequency	f_{M}	179.50	179.53	179.56	MHz	Fit Fig. 3.3c
Quality factor	Q_{M}	7500	6000	4500	-	
Electromechanical signal	V_{M}	8.7	8.8	8.9	nV	
Voltage noise	$\sqrt{S_{VV}}$	50.8	50.3	49.8	$\mathrm{pV}/\sqrt{\mathrm{Hz}}$	
Nanotube diameter	D	3	4.5	6	nm	TEM
Number of walls	N_{W}	1	2	3	-	
Suspended height	H	4.5	18	110	nm	Electrostatic simulation
Misalignment	θ	0	35	70	$^\circ$	
Effective charge derivative	$\partial q/\partial u$	-344	-53.2	-14.8	pC/m	
Capacitance derivative	$\partial C_2/\partial u$	320	49.4	13.1	pF/m	
Mass	m	5.8	21.3	102	ag	Eq. (3.23)
Excitation voltage	δV_{G}	1.6	1.4	1.3	μV	Section 2.2
RMS displacement	u	836	25.2	0.9	pm	Eq. (3.24)
Displacement sensitivity	$\sqrt{S_{uu}}$	4830	144.3	5.3	$\mathrm{fm}/\sqrt{\mathrm{Hz}}$	Eq. (3.7)
Expected sensitivity	$\sqrt{S_{uu}^{\mathrm{expected}}}$	106	574	2596	$\mathrm{fm}/\sqrt{\mathrm{Hz}}$	Eq. (3.30)
Standard quantum limit	$\sqrt{S_{uu}(\mathrm{SQL})}$	10.3	4.84	1.91	$\mathrm{fm}/\sqrt{\mathrm{Hz}}$	Eq. (3.9)

Table 3.1: Summary of parameters used to calculate the displacement sensitivity, showing the best estimate of parameters, and two cases corresponding to the highest and the lowest values of the imprecision consistent with the experimental results. The error bar in Eq. (3.1) is taken by considering these two extremes.

- The gate capacitance derivative C_2', which sets the electrostatic force, is estimated from a finite-element electrostatic simulation. Setting up the simulation is made difficult by the fact that the height H of the nanotube above the gate, the nanotube's misalignment θ, and its diameter D are not known precisely (Fig. 3.1a). However, these quantities are constrained by the fact that the gate capacitance C_2 is known. From the Coulomb peak spacing for the SET (Fig. 3.4) the gate capacitance is $C_2 = e/\Delta V_G = 3.3 \pm 0.6$ aF. This lets us use the simulation to determine the minimum and maximum values of $\partial C_2/\partial u$ consistent with this value of C_2 and with the geometric constraints. We expect from TEM images that $D = 4.5 \pm 1.5$ nm, while the range of H is set by the thickness of the contact electrodes, giving $H < 110$ nm.

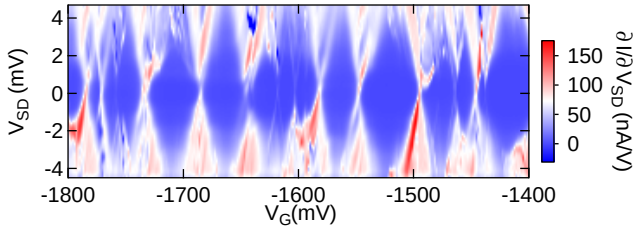


Figure 3.4: Differential conductance through the nanotube as a function of the voltage V_G on gate 2 and of the bias V_{SD} across the quantum dot. The width of the Coulomb diamonds is $\Delta V_G = 49 \pm 8$ mV, from which the corresponding gate capacitance $C_2 = 3.3 \pm 0.6$ aF is extracted.

The maximum misalignment consistent with these constraints is $\theta = 70°$, which can occur when $D = 6$ nm and $H = 110$ nm. If there is no misalignment ($\theta = 0°$) and the diameter is $D = 3$ nm, the suspended height is required to be as small as $H = 4.5$ nm. As the preferred estimate for θ we take the central value, giving $\theta = 35 \pm 35$ degrees and implying $H = 18^{+92}_{-13.5}$ nm and $\partial C_2/\partial u = 49.4^{+271}_{-40.5}$ pF m^{-1}. The numerical derivative is calculated by simulating a uniform displacement of the nanotube, and multiplying by $\sqrt{2}$ to take account of the fact that the actual mode shape has a larger displacement near the centre [83].

- The nanotube's mass is given by:

$$m = \frac{\pi \rho_S N_{\mathrm{W}} D l}{\cos\theta} = 21.3^{+81}_{-15.5}\ \mathrm{ag} \tag{3.23}$$

  where $l = 800$ nm is the contact spacing, $\rho_S = 7.7 \times 10^{-7}$ kg m^{-2} is the sheet density of graphene and $N_{\mathrm{W}} = 2 \pm 1$ is the number of nanotube walls estimated by TEM.

- The drive amplitude δV_{G} is known from the RF transmission of the cryostat wiring, and confirmed by measuring Coulomb peak broadening (Section 2.2).

Substituting these values into Eq. (3.22) leads to an estimate for the rms displacement on resonance:

$$u = 25.2^{+811}_{-24.3}\ \mathrm{pm} \tag{3.24}$$

and therefore a displacement sensitivity, defined as the square root of the measurement imprecision [116]:

$$\sqrt{S_{uu}} = \frac{u}{V_{\mathrm{M}}}\sqrt{S_{VV}} \tag{3.25}$$

$$= 144.3^{+4686}_{-139}\ \mathrm{fm}/\sqrt{\mathrm{Hz}}. \tag{3.26}$$

These estimated parameters and their contributions to the uncertainty of S_{uu} are summarised in Table 3.1.

3.6.3 The expected displacement sensitivity

We now compare this experimentally extracted displacement sensitivity (Eq. (3.26)) with the value expected from the electrical characteristics of the circuit. On resonance, the electromechanical signal is dominated by the first term of Eq. (3.12):

$$V_{\mathrm{M}} = Z_{\mathrm{trans}}(f_{\mathrm{M}}) I \tag{3.27}$$

$$= Z_{\mathrm{trans}}(f_{\mathrm{M}}) \frac{q'}{C_2} \frac{\partial I_{\mathrm{DC}}}{\partial V_{\mathrm{G}}} u, \tag{3.28}$$

where I is taken from Eq. (3.14), neglecting the small second term. This implies a sensitivity

$$\sqrt{S_{uu}^{\text{expected}}} = \frac{u}{V_{\text{M}}}\sqrt{S_{VV}} \tag{3.29}$$

$$= \frac{1}{Z_{\text{trans}}(f_{\text{M}})}\frac{1}{q'}\frac{C_2}{\frac{\partial I_{\text{DC}}}{\partial V_{\text{G}}}}\sqrt{S_{VV}}. \tag{3.30}$$

The transimpedance of the circuit is not directly measurable but can be plausibly modelled (see Section 2.3), leading to $Z_{\text{trans}}(f_{\text{M}}) \approx 198\ \Omega$. Taking the slope $\frac{\partial I_{\text{DC}}}{\partial V_{\text{G}}} \approx 28$ nA/V from data similar to Fig. 3.3a, taking the charge derivative $q' \approx -50$ pC/m from Eq. (3.19) using electrostatic simulation of the gate capacitances, and taking the noise $\sqrt{S_{VV}} \approx 51\text{pV}/\sqrt{\text{Hz}}$ from the specification of the cryogenic amplifier, leads by Eq. (3.30) to an expected sensitivity:

$$\sqrt{S_{uu}^{\text{expected}}} \sim 600\ \text{fm}/\sqrt{\text{Hz}}. \tag{3.31}$$

This is within the uncertainty of the measurement (Eq. (3.26)), implying that the motion is approximately as estimated in Eq. (3.24), that the electrical signal indeed arises from changes in the nanotube's conductance, and that the noise is dominated by the electrical noise of the cryogenic amplifier. However, we note that this agreement depends on the estimate of Z_{trans}, and that including parasitic impedances in our circuit model can lead to poorer agreement between Eq. (3.26) and Eq. (3.31), possibly implying a larger nanotube mass than stated in Eq. (3.23).

In Fig. 3.5 we plot the experimentally extracted displacement sensitivity $\sqrt{S_{uu}}$ with the expected value $\sqrt{S_{uu}^{\text{expected}}}$ under various assumptions of the misalignment angle θ and the nanotube height H. It can be seen that the uncertainty in the nanotube geometry has resulted in a large error bar, and that $\sqrt{S_{uu}}$ and $\sqrt{S_{uu}^{\text{expected}}}$ have opposite dependence to the misalignment angle. The reduced discrepancy therefore indicatively supports our estimated conditions.

3.7 Conclusion

In conclusion, this experiment shows how to monitor a vibrating carbon nanotube with low noise and high speed using an integrated SET transducer. Such a device

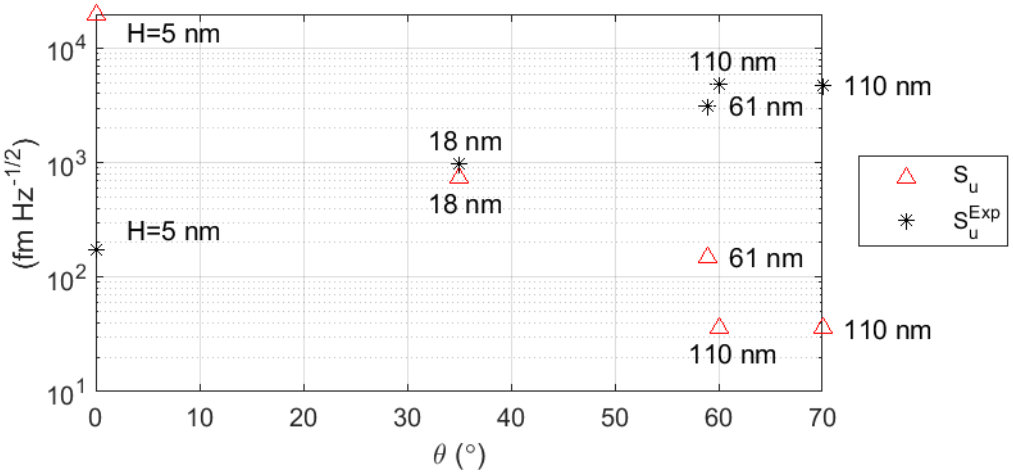


Figure 3.5: Measured displacement sensitivity $\sqrt{S_{uu}}$ and the expected value $\sqrt{S_{uu}^{\text{expected}}}$ as functions of the misalignment angle θ and the nanotube height H.

could monitor weak and transient forces on the nanoscale, for example in scanning probe microscopy. This resonator also approaches the quantum regime both in terms of the ratio of phonon energy to thermal energy (approximately 1:3) and in terms of the measurement sensitivity. This work therefore opens the way to measuring dynamic electron-phonon coupling effects.

4

A coherent nanomechanical oscillator driven by single-electron tunnelling

Contents

4.1 Introduction 48
4.2 Back-action turns a resonator into an oscillator 51
4.3 Mechanical coherence 54
4.4 Injection locking and anharmonic effects 57
4.5 Stabilisation through feedback 60
4.6 Methods 62
4.6.1 IQ tomography 62
4.6.2 Signal autocorrelation 63
4.6.3 Feedback stabilization 64
4.7 Theory of self-driven oscillations 64
4.7.1 Oscillation mechanism 64
4.7.2 Quantifying the electromechanical coupling 67
4.7.3 Phonon number and minimal linewidth 69
4.7.4 Consequences of anharmonicity 70
4.8 Characterizing the displacement sensitivity 78
4.9 Supplementary data 80
4.9.1 Mechanical linewidth through the oscillation threshold . 80
4.9.2 Resonance linewidth 81
4.9.3 Self-oscillation frequency stability 81
4.9.4 Thermal Dependence 84
4.9.5 Further characterization of the emission sidebands . . . 84
4.9.6 Joint histogram of feedback-locked oscillation 86
4.9.7 50 Hz pick-up in the $g^{(2)}$ data 87
4.9.8 Oscillation bistability 87
4.9.9 Strong localization 88

4.10 Conclusion 89

A single-electron transistor embedded in a nanomechanical resonator represents an extreme limit of electron-phonon coupling. While it allows fast and sensitive electromechanical measurements, it also introduces back-action forces from electron tunnelling that randomly perturb the mechanical state. Despite the stochastic nature of this back-action, it has been predicted to create self-sustaining coherent mechanical oscillations under strong coupling conditions. Here, we verify this prediction using real-time measurements of a vibrating carbon nanotube transistor. This electromechanical oscillator has some similarities with a laser. The single-electron transistor pumped by an electrical bias acts as a gain medium and the resonator acts as a phonon cavity. Although the operating principle is unconventional because it does not involve stimulated emission, we confirm that the output is coherent. We demonstrate other analogues of laser behaviour, including injection locking, classical squeezing through anharmonicity, and frequency narrowing through feedback.

4.1 Introduction

Back-action forces are an inescapable accompaniment to nanomechanical measurements. While their ultimate limit is set by quantum uncertainty [116], in practical devices they may become significant even well before this limit is reached. Among the most sensitive nanomechanical probes is the single-electron transistor (SET), which transduces motion with a precision that can approach the standard quantum limit [4, 176]. However, the price is that the force exerted even by individual electrons modifies the mechanical dynamics. This introduces strong electron-phonon coupling [89, 95, 151], which has usually been recognised by its incoherent effects such as dissipation, frequency softening, nonlinearity, and cooling [5]. Here, we show that electromechanical back-action can also have a coherent result, by harnessing it to create a self-sustained mechanical oscillation. The resulting device is analogous to a laser, where the optical field is replaced by the mechanical displacement. In contrast to existing phonon lasers pumped by optical or mechanical drives [177–179],

the oscillator is driven by a constant electrical bias. The device exhibits several laser characteristics, detected via its electrical emission, including phase and amplitude coherence. It serves both as a novel on-chip phonon source and to explore the connection between the physics of back-action and of lasers.

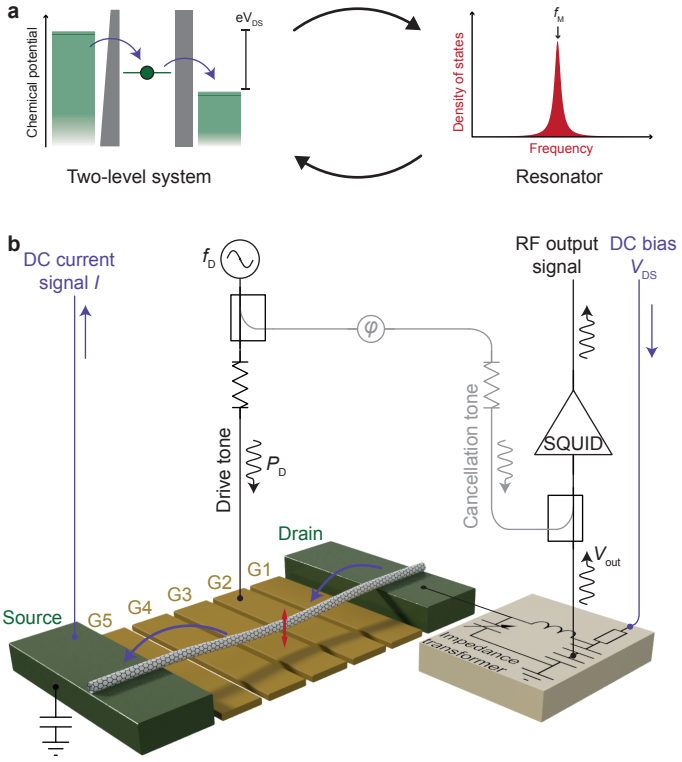


Figure 4.1: Strongly coupled single-electron electromechanics. **a**, Schematic of a single-electron transistor (SET) coupled to a mechanical resonator. The SET acts as a two-level system, while the resonator is a phonon cavity at mode frequency f_{M}. Electron tunnelling through the SET leads to a non-equilibrium population distribution which pumps the oscillator. **b**, Device realisation and measurement setup. The vibrating nanotube, configured as an SET, is suspended between contact electrodes (green) and above gate electrodes (yellow). The SET is biased by a drain-source voltage V_{DS}, and the motion is measured via the electrical current, which is monitored both at DC (current path indicated by blue arrows) and via an RF circuit for time-resolved measurements (signal path marked by undulating arrows; see text). The resonator can be driven directly by a tone with power P_{D} at frequency f_{D}, part of which is routed via a cancellation path to avoid saturating the amplifiers.

To enter this regime of strong back-action, the SET, serving as a two-level system, must couple strongly to a mechanical resonator serving as a phonon cavity (Fig. 4.1a). As a high-quality resonator, we use a suspended carbon nanotube [88]. Nanotubes have both low mass and high mechanical compliance, which are favourable for strong electron-phonon interaction [89, 151, 161, 180, 181]. The selected nanotube is a narrow-gap semiconductor, allowing the SET to be defined in the nanotube

itself using tunnel barriers at each end and a conducting segment near the middle. The two relevant SET states are the configurations with and without an excess electron. Flexural vibration of the nanotube modulates the electrical potential experienced by the SET, causing the current to vary with displacement; at the same time, each added electron exerts a force that is larger than both quantum and thermal force fluctuations (see Sec. 4.7.2). They also introduce feedback leading to electromechanical frequency softening, nonlinearity, dissipation [170] and eventually back-action noise [116, 182]. With sufficiently strong electron-phonon coupling, the feedback instability between these two degrees of freedom leads to Franck-Condon physics [183, 184] and switching events [94, 95, 185, 186].

The combination of these effects sets up an electromechanical feedback with rich predicted behaviour [187]. If the SET's energy splitting is resonant with the mechanical frequency, electrical excitations should be able to pump the resonator in a direct analogue of the micromaser [188]. More surprisingly, a laser-like instability is predicted even in a non-resonant situation, with complex dynamics that depend on level alignment and damping, and go beyond conventional laser behaviour [91, 96]. It is, to some extent, an electromechanical counterpart of the spin-polarized DC current-driven magnetic oscillation seen in nanomagnets et al. [189]. Previous experiments measuring time-average current through a nanotube have provided strong evidence for a threshold between resonance and oscillation [89, 112, 153]. However, to test these predictions by fully characterizing the resulting states requires time-resolved displacement measurements [190, 191], which have not yet been possible in this regime of strong back-action. The real-time observation of such resonator makes it a possible platform to study nonequilibrium thermodynamics in the nanoscale [192, 193].

4.2 Back-action turns a resonator into an oscillator

To explore these dynamic effects, we implemented an electromechanical circuit for measuring the nanotube's vibrations directly [180] (Fig. 4.1b). The carbon nanotube resonator is stamped across metallic contact electrodes to give a vibrating segment of length $l \approx 800$ nm [115], and is measured at a temperature of 25 mK. Voltages applied to five finger gates beneath the nanotube (labelled G1-G5) are used both to tune the electrical potential and to actuate vibrations by injecting an RF tone with drive power P_{D}. A voltage bias V_{DS} is applied between the contacts to drive a current I. To configure the nanotube as an SET, the gate voltages are set to tune an electron tunnel barrier near each contact. The conductance thus depends strongly on the displacement, which allows sensitive electromechanical readout via the current through the nanotube. The radio-frequency (RF) part of the current is passed through an impedance transformer and then amplified, with the primary amplifier being an ultra-low-noise SQUID [136]. The resulting RF output voltage V_{out} is therefore proportional to the instantaneous displacement and is a sensitive time-resolved record of the mechanical vibrations [180].

To identify signatures of electromechanical feedback, we first measure the DC conductance as a function of bias and DC gate voltage V_{G} applied to gate G2 (Fig. 4.2a). Superimposed on the diamond pattern characteristic of single-electron charging are irregular sharp ridges of strongly positive or negative conductance as the nanotube switches between high and low-current states. Such features are associated with the onset of mechanical instability for bias exceeding a critical threshold [89, 91].

We detect the mechanical resonance by fixing the bias voltage and measuring the transmission of the drive tone to the RF amplifier input, using a scalar network analyser. When the drive frequency matches the mechanical resonance, the resulting motion relative to the gate electrodes changes the chemical potential of the SET, modulating the current at the drive frequency. This current, entering the impedance transformer, excites an RF output voltage V_{out}, which is proportional to the nanotube's displacement [180]. The RF output signal voltage is therefore

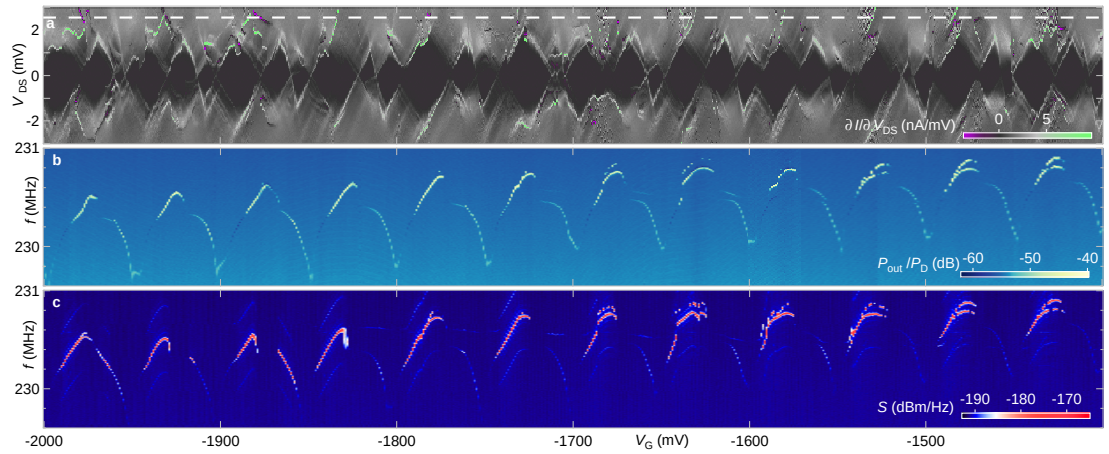


Figure 4.2: Mechanical resonance and oscillation a, Differential conductance of the nanotube as a function of gate voltage V_G and bias V_{DS}, with no driving applied. The diamond pattern is characteristic of Coulomb blockade in an SET, with some irregularity due to electrostatic disorder. Superimposed on the expected diamond pattern are sharp lines of strongly positive or negative differential conductance (green or purple in this colour scale), indicating thresholds for self-oscillation. **b**, Mechanical resonance detected in a transmission measurement. The nanotube is biased with $V_{DS} = 2.5$ mV (dashed line in a) and driven with power $P_D = -99$ dBm to gate G2. The transmission is plotted as the emitted power P_{out} into the amplifier chain. The mechanical resonance appears as a sharp spectral peak, or occasionally as a faint dip when RF leakage interferes destructively with the mechanical signal. **c**, Emission spectrum under the same conditions but with no RF drive. A spectral peak is still present, at almost exactly the same frequency as in b. This indicates self-driven mechanical oscillations. Faint sidebands to the main signal are artefacts of the SQUID (see Sec. 4.9.5).

proportional to the nanotube's displacement, apart from the contributions of nonlinear SET transconductance and of RF electrical leakage [180]. For most gate voltage settings, these contributions are small. The mechanical resonance therefore appears as a sharp peak in the electrical transmission from the drive to the output (Fig. 4.2b). The resonance frequency fluctuates quasiperiodically with gate voltage, which is a further indication of electromechanical coupling because the effective spring constant is softened when the SET is configured close to a Coulomb charge transition [89, 151]. From the peak width, the mechanical quality factor is $Q_M \approx 1.8 \times 10^4$, with some gate voltage dependence because of electromechanical damping.

Mechanical oscillations, as distinct from a mechanical resonance, become evident when the output power spectrum is measured without driving using a spectrum analyser (Fig. 4.2c). This undriven emission, plotted as a power spectral density S referenced to the amplifier input, shows a peak whose frequency approximately

follows the resonance of Fig. 4.2b. The peak is only present for some gate voltage settings, and is brightest close to the transport ridges of Fig. 4.2a. Furthermore, this peak strengthens with increasing bias (see Sec. 4.9.1). For some gate voltage settings on the right of the graph, the peak switches between two or more frequencies, suggestive of dynamical bifurcation. All these observations imply that the observed undriven emission is a result of self-excited mechanical oscillations driven by the DC bias across the device.

The coordinate displacement of the CNT modulates the effective electrical potential of the SET, which is transduced to an RF signal in the tank circuit, hence creating the sharp features in the spectrum. On Coulomb peaks, the electron tunnelling overscreens the gate voltage, softening the effective spring constant [89, 151], so the mechanical signal periodically dips. We notice the sudden departure of the resonance peaks from the expected frequency, similar to the DC observation in Ref. [89], aligning with the switching ridges in Fig. 4.2a. In searching for the RF emission, we turn off the actuation power and plot the undriven spectrum in Fig. 4.2c, and find the resonance peaks remaining in where they align with the DC switch-ridges. The switching feature is predicted [91] for where the single-electron tunnelling is just strong enough to compensate for the mechanical damping. The oscillation amplitude thus grows resonantly until the amplitude is too large and the SET damping becomes positive again [91] (see Sec. 4.7.1). The alignment of the switching events in both the current in Fig. 4.2a and the RF resonance peaks in Fig. 4.2b,c suggests the single-electron-tunnelling induced coherent oscillation in this nanomechanical resonator [89, 91]. and indeed we prove the elevated resonance frequency another feature of the self-oscillation behavior in Sec. 4.7.1. A second mode with a slightly higher resonance frequency is visible near $V_{\mathrm{G}} = -1600$ mV in Fig. 4.2b,c, likely due to an orthogonal mode. We notice accompanying each major Coulomb peak there are constantly a pair of weak peaks that do not close at zero bias. This is possibly due to some defect-induced strong localization in the nanotube, splitting the charge states spatially and effectively creating a

double quantum dot with a thin middle wall. We will show some evidence for such interpretation in Sec. 4.9.9.

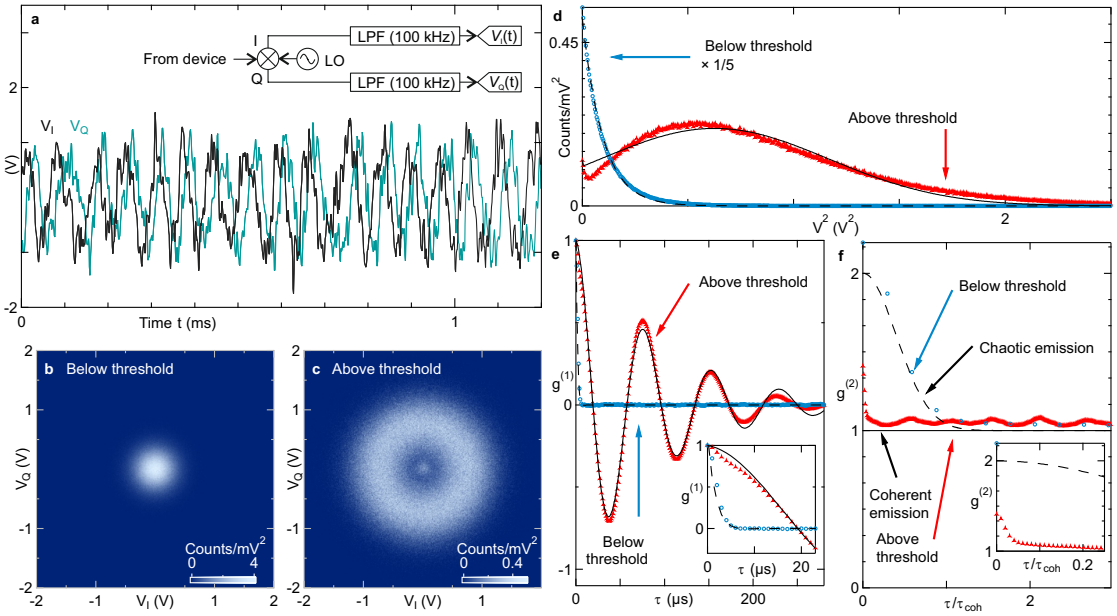


Figure 4.3: Coherence of the free-running oscillator. **a**, Time traces of in-phase (I) and quadrature (Q) components demodulated from the oscillator output. The heterodyne demodulation circuit is shown in the inset. (LO: local oscillator; LPF: low-pass filter). **b**, Joint histogram of demodulated components with the gate voltage set below the oscillation threshold ($V_G = -1982$ mV). **c**, Histogram when configured above threshold ($V_G = -1568$ mV), showing the characteristic ring of coherent emission. **d**, Symbols: Histograms of total power $V^2(t) = V_I^2(t) + V_Q^2(t)$ below and above threshold, corresponding to the joint histograms in **b, c**. The former is scaled downwards for clarity. Dashed line: fit to below-threshold data, assuming quasi-thermal source. Solid lines: fits to above-threshold data. Grey line assumes a Gaussian distribution of phonon numbers plus a small quasi-thermal fraction. **e**, Symbols: Autocorrelation as a function of time difference τ. Solid line: Above-threshold fit of the form $g^{(1)}(\tau) = e^{-\tau/\tau_{coh}} \cos(2\pi\Delta f\tau)$, giving coherence time $\tau_{coh} = 99$ μs and heterodyne frequency detuning $\Delta f = 13$ kHz. Dashed line: Similar fit to below-threshold data with Δf fixed at zero, giving a decay time $\tau_{coh} = 3.3$ μs consistent with the filter bandwidth. **f**, Symbols: Second-order correlation, plotted with respect to the coherence time fitted above. Curves: Parameter-free predictions for Gaussian chaotic emission and for coherent emission [131]. Insets in **e** and **f** are zoom-ins.

4.3 Mechanical coherence

With fast electromechanical readout, the coherence of this mechanical oscillator can be directly confirmed by measuring the output signal in real time. To do this, the signal is mixed with a local oscillator in a heterodyne circuit [194, 195] to generate records of the in-phase and quadrature voltages $V_I(t)$ and $V_Q(t)$ as a function of time t. The output record (Fig. 4.3a) shows clear sinusoidal oscillations. The onset

of mechanical coherence is seen when the in-phase and quadrature time traces are represented as two-dimensional histograms for gate voltage settings above and below the oscillation threshold. Below threshold, the histogram is peaked near the origin, consistent with a band-limited but quasi-thermal source such as a randomly kicked resonator (Fig. 4.3b). However, above threshold the histogram has a ring shape, showing amplitude coherence characteristic of a laser-like oscillator (Fig. 4.3c). The ring diameter corresponds to an approximate phonon number $\bar{n}_{\mathrm{p}} \sim 10^4$, i.e. an oscillation amplitude of ~ 1 nm, although there is a large uncertainty because of unknown device parameters.

The clearest comparison to an ideal classically coherent source comes from a histogram of total output power, which is proportional to the number of phonons in the mode (Fig. 4.3d). Below threshold, the histogram follows the exponential distribution of completely incoherent quasi-thermal emission [194]. Above threshold, the histogram shifts to a distribution where the most probable state has a non-zero output power, as expected for a coherent source. It is approximately fitted by a Gaussian distribution, characteristic of a coherent oscillator in the limit of large phonon number $\bar{n}_{\mathrm{p}}$. However, the distribution is slightly skewed, while its width, which for an ideal coherent state would be $\sim \sqrt{\bar{n}_{\mathrm{p}}}$, is much larger than expected. Both the excess width and the skew indicate additional noise in the oscillator, presumably due to complex feedback between motion and electron tunnelling.

While amplitude coherence is shown by the histogram, phase coherence is determined by plotting the autocorrelation of the demodulated signal $g^{(1)}(\tau)$ as a function of time interval τ (Fig. 4.3e). For these settings, the data are well fitted by an decaying sinusoid, reflecting the slow phase drift of the free-running oscillator. The envelope decay gives a phase coherence time $\tau_{\mathrm{coh}} = 99$ μs, i.e. a coherence linewidth of $\delta f_{\mathrm{coh}} = 1/\pi\tau_{\mathrm{coh}} = 3$ kHz, approximately three times narrower than the mean resonance linewidth $f_{\mathrm{M}}/Q_{\mathrm{M}}$ (See Sec. 4.9.2). The emission spectrum shows no dependence of linewidth on temperature up to 700 mK (data not shown). Coherence is further confirmed by plotting the second-order correlation function

$g^{(2)}(\tau)$, which shows chaotic quasi-thermal behaviour below threshold but nearly coherent behaviour above threshold [131] (Fig. 4.3f).

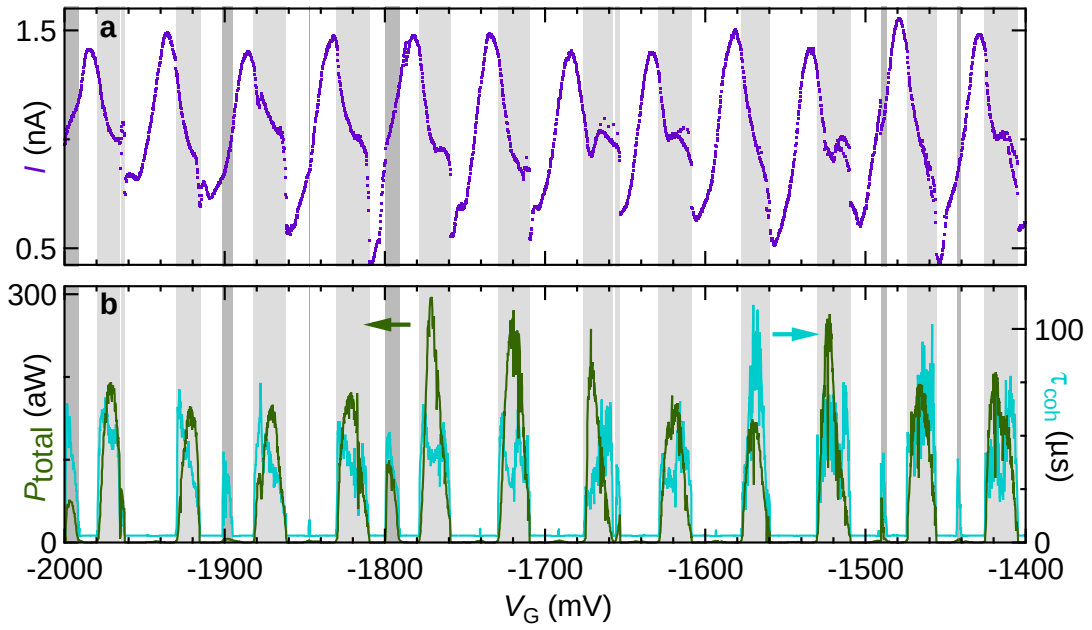


Figure 4.4: Tuning the coherence with a gate voltage. **a**, The DC current I through the device as a function of gate voltage V_G, with $V_{DS} = 2.5$ mV and no RF drive. **b**, Simultaneously acquired emission power P_{total} (left axis) and fitted coherence time τ_{coh} (right axis). Shading marks voltage settings with detectable emission.

As the gate voltage is swept, the device switches between oscillating and non-oscillating states, and both the oscillator power and coherence time vary (Fig. 4.4). By simultaneously measuring the RF and DC signals, the consequences for DC transport can be seen. Fig. 4.4a shows current as a function of gate voltage over several periods of Coulomb blockade, while Fig. 4.4b shows the coherence time and emission power P_{total} over the same range. The oscillator switches on and off approximately once per Coulomb period. Both the coherence time and the emitted power vary irregularly, but as expected most switches between oscillating and non-oscillating conditions coincide with abrupt current changes.

At least three theoretical mechanisms allow an electrical current to create the positive feedback force that drives coherent oscillations. When two energy levels, for example in a double quantum dot, are misaligned by a multiple of the phonon

energy [196], positive feedback occurs through conventional stimulated emission [194]. However, such a condition should occur at precise gate voltage settings, whereas Fig. 4.2c shows emission across a wide range of gate voltage. Another possible mechanism is electrothermal, in which the thermal mass of the resonator delays the expansion or contraction due to ohmic heating [197]. While this mechanism may contribute in our device, the sign of the feedback should be proportional to dI/dV_{G}. However, Fig. 4.4 shows oscillations occur on both sides of the Coulomb peaks. We therefore attribute the oscillations mainly to a third mechanism; the combination of the SET's capacitance with delayed electron tunnelling. When the tunnel barriers are such that the usual dependence of the SET's charge on displacement is inverted, this creates the required positive feedback force [91, 96] (see Sec. 4.7.1).

In RF measurements, this explains the peak bifurcation in Fig. 4.2b,c, because the spectrum analyzer is set to a much narrower bandwidth (RBW = 3 Hz, VBW = 1.5 Hz) so the resonator switches between states during acquisition, giving rise to the double peak pattern that align with the mosaic features in DC. It is also responsible for the bright spot in Fig. 4.3c. Finally in this Figure we notice the RF power P_{total} does not vanish when $I/V_{\mathrm{G}} = 0$, a natural consequence of the current being modified by the vibration [91].

4.4 Injection locking and anharmonic effects

While the phase coherence time extracted from the autocorrelation characterizes the long-term oscillator stability, it is limited by slowly varying extrinsic effects such as charge noise or adsorbed atoms [161]. To evaluate sensing schemes that rely on detecting mechanical frequency shifts, it important to identify the oscillator's intrinsic linewidth if this slow variation could be eliminated, which may be much narrower. To measure the intrinsic linewidth, we employ two techniques from laser spectroscopy to stabilise the oscillator frequency.

First, we demonstrate that the oscillator can be locked to a stable but weak seed tone applied to the gate [199, 200]. This phenomenon of injection locking, previously demonstrated for trapped ions [201] and driven mechanical resonators [202], arises

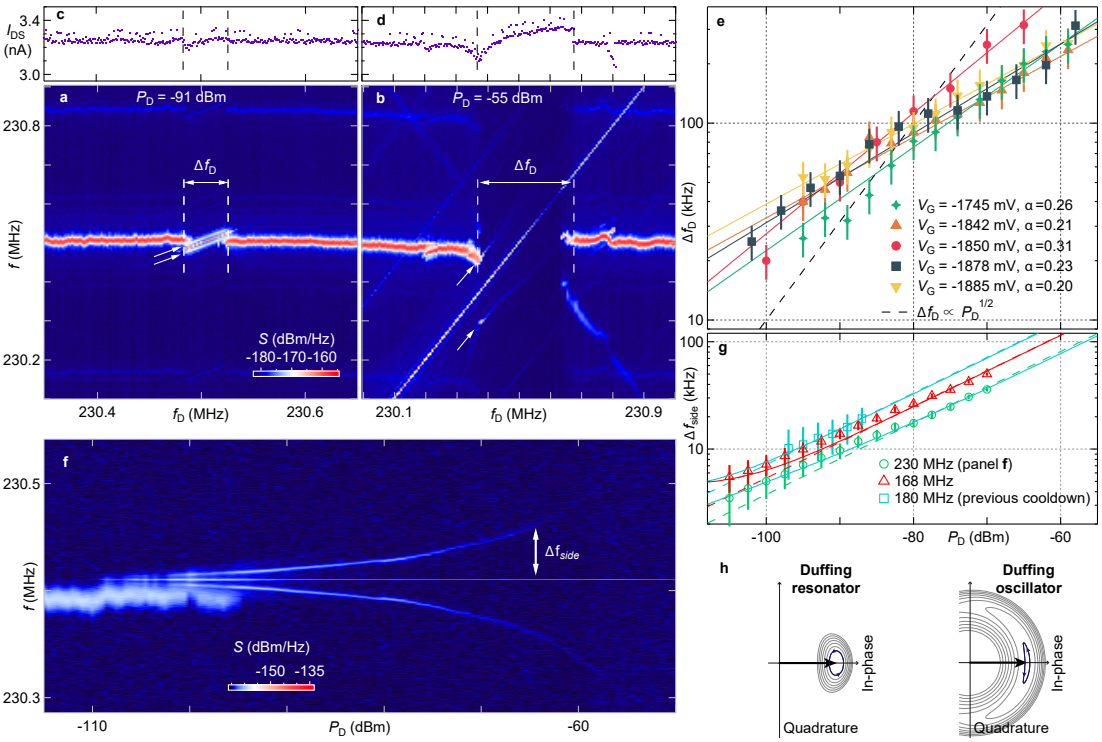


Figure 4.5: Injection locking of the nanomechanical oscillator. a, b, Oscillator emission, plotted as a spectral density $S(f)$, in the presence of an injection tone at frequency f_D. The broad horizontal line is the free-running emission. When the injection frequency is within the capture range Δf_D, the oscillator locks to it, resulting in both a shift and a narrowing of the emission peak. These two plots, measured with different injection power P_D, show that the capture range increases with increasing power. A pair of power-dependent satellites is marked by arrows. (Other faint sidebands running parallel to the main signal are artefacts of pickup in the SQUID.) In panel **b**, a distortion sideband is also evident running from upper left to lower right. **c, d**, DC current as a function of f_D, measured simultaneously with **a** and **b**. **e**, Locking range Δf_D as a function of injection power P_D, measured for different gate voltage settings. Symbols: Data; Solid lines: Fits of the form $f_D \propto P_D^{\alpha}$, with α as a free parameter. Dashed line: Dependence for $\alpha = 1/2$, as expected for conventional injection locking [198]. Error bars reflect the width of the transition to locking in plots similar to **a** and **b**. **f**, Transmission spectrum plotted against injection power, showing transition from free-running (low power) to locked (high power). In the locked regime, the expected central emission peak is accompanied by a pair of satellites. To avoid frequency mixing in the SQUID, it is unbiased during this measurement. **g**, Symbols: satellite offset frequency under different tuning conditions. Lines: Fits to models of the Duffing oscillator (see Sec. 4.7.4). Dashed lines are high-power approximation $\Delta f_{\mathrm{side}} \propto P_D^{1/3}$; solid lines are fit to numerical model with Duffing factor as the free parameter. Error bars reflect the linewidths. **h** Cartoons of hamiltonian function in the rotating frame for Duffing resonator and oscillator. Thick arrow denotes the stationary amplitude. Fluctuations around this amplitude orbit along the hamiltonian contours. The contours are squeezed in both cases, but more so for the oscillator because the magnitude is stabilised by self-feedback.

because feedback amplifies small forces close to the operation frequency. In this measurement, the emission is monitored while the seed tone is applied at a nearby frequency f_{D} (Fig. 4.5). As seen in Fig. 4.5a, b, for a range of f_{D} settings near the free-running oscillator's frequency and with sufficient drive power P_{D}, the broad emission line collapses onto the injection frequency. The locking events are accompanied by steps in the DC current (Fig. 4.5c, d).

The frequency range Δf_{D} over which the oscillator is locked extends over many linewidths. Figure 4.5e shows the locking range as a function of injected power, confirming that a stronger injection tone has greater frequency pull. The data are well fitted by a power law of the form $f_{\mathrm{D}} = AP_{\mathrm{D}}^{\alpha}$, where A and α are fit parameters. However, whereas the theory of conventional oscillators [198] predicts an exponent $\alpha = 0.5$, the data show a smaller exponent $\alpha \sim 0.3$.

A second unexpected feature is a pair of weak spectral satellites, marked by arrows in Fig 4.5a-b. To investigate these further, Fig. 4.5f shows the emission spectrum as a function of injection power across the transition to locking. Surprisingly, the satellite offset frequency Δf_{side} depends on injection power, with a dependence that is approximately $\Delta f_{\mathrm{side}} \propto P_{\mathrm{D}}^{0.3}$ (Fig. 4.5g).

Both the anomalous locking range and the sidebands can be explained by the oscillator's anharmonicity, which modifies the conventional theory of injection locking in harmonic oscillators. As recently demonstrated in a high-quality nanowire, similar satellites can appear when the anharmonic frequency shift is much larger than the linewidth [203]. They arise because the fluctuations of the displacement about its stationary driven value experience an effective restoring spring constant which is modified by the anharmonicity and therefore different from the resonator's bare spring constant [204]. The effective spring constant may differ between fluctuations in magnitude and phase, leading to classically squeezed fluctuations; the degree of squeezing can be inferred from the relative intensities of the satellites.

In this respect the nanotube oscillator behaves very differently from an anharmonic (Duffing) resonator. In an anharmonic resonator, the satellites are asymmetric [203], with the intensity ratio never greater than $\tanh^2 \frac{1}{4} \ln 3 \approx 0.27$;

however, in Fig. 4.5f the intensity ratio is close to unity. The reason is illustrated in Fig. 4.5h and explained further in the Sec. 4.7.4. In an anharmonic driven resonator, a perturbed state orbits the stationary point in the rotating frame, which when transformed to the lab frame gives sidebands in the displacement spectrum. An elliptical orbit contains a higher spectral weighting at the frequency corresponding to its sense of rotation, and therefore transforms to asymmetric sidebands. In the anharmonic driven oscillator, the orbits can become very elongated, because the self-feedback stabilises magnitude but not phase. Such an orbit contains nearly equal components in both rotation senses, and therefore generates symmetric sidebands. This is an indication that the injection-locked oscillator generates a classically squeezed state, in the sense that the displacement variance is much larger in the phase quadrature than in the amplitude quadrature.

By solving the equations of motion including a Duffing restoring force (proportional to displacement cubed) in the limit of strong driving and weak damping (see Sec. 4.7.4), both f_{D} and Δf_{side} are found to be proportional to $P_{\mathrm{D}}^{1/3}$. This is in good agreement with the data (Fig. 4.5e, g). A numerical solution not assuming strong drive gives slightly better fit for Δf_{side} (Fig. 4.5g).

4.5 Stabilisation through feedback

While injection locking clearly stabilises the oscillator's state, it also contaminates the output spectrum with the high-frequency seed tone. An improved way to measure the oscillator's intrinsic linewidth is to use feedback to cancel out slow frequency wander. This exploits the voltage tuning of the oscillator, and is analogous to Pound-Drever-Hall locking, used for sensitive laser measurements such as gravitational wave astronomy [205, 206]. To implement this scheme (Fig. 4.6), the oscillator is incorporated into a phase-locked loop using error signal voltage fed to gate G1 (see Methods). Figure 4.6a shows dramatic frequency narrowing when the feedback is turned on. With optimised control parameters, the stabilised linewidth is $\delta f < 2$ Hz (Fig. 4.6b), which is limited by the spectral resolution and implies over 10^8 coherent oscillations at the operating frequency of 230 MHz.

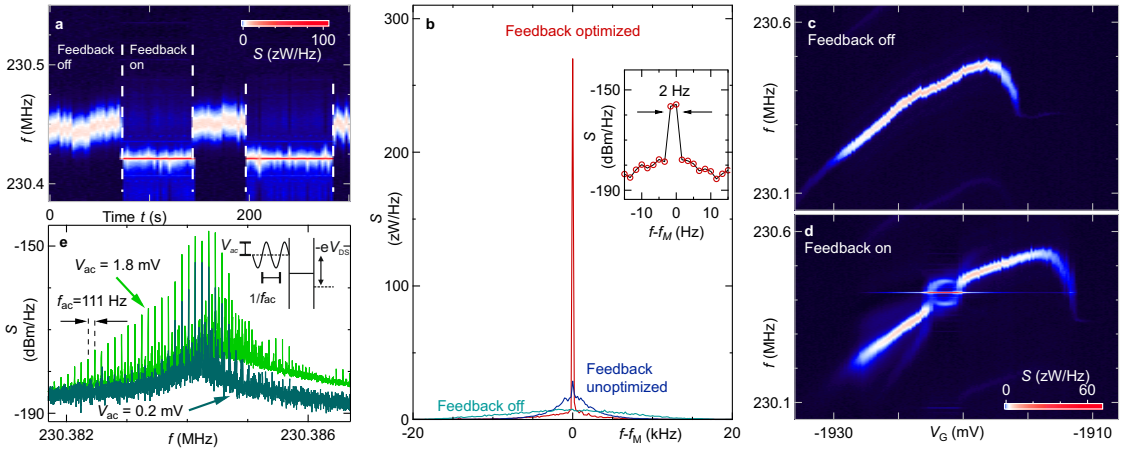


Figure 4.6: Stabilizing the oscillator with feedback **a**, Power spectrum of oscillator emission $S(f)$ as a function of time. With feedback off, the emission peak is broad and fluctuates. Turning feedback on leads to intense emission at the target frequency, here 230.42 MHz. To make the stabilised peak visible, the data is binned over 1 kHz vertical window in panels **a, c**, and **d**. **b**, Power spectrum for three different setting of the feedback controller's PID settings: feedback off, on but unoptimized, and fully optimized. When optimally locked the linewidth is less than 2 Hz (inset), limited by the point spacing. **c, d** Free-running (**c**) and feedback-locked (**d**) oscillation spectra as functions of DC gate voltage, showing the locking range. With feedback on, a weak stabilised peak persists even when the oscillator's central frequency has moved outside the main locking range, indicating that occasional large frequency excursions occur that can be detected when they are temporarily stabilised by the feedback circuit. **e** Using the stabilised oscillator as the basis for a microwave frequency comb. Modulating the voltage bias (see inset) leads to a series of narrow, equally spaced sidebands, whose strength depends on the modulation depth. In this case the comb extends over a range up to 35 kHz.

This represents an upper limit on the intrinsic linewidth, and shows it is limited by slowly varying environmental perturbations, such as voltage noise, substrate switchers, and changing surface contamination, rather than by intrinsic damping or by high-frequency noise, which the feedback does not cancel. It is the linewidth that the free-running oscillator would achieve if these slow perturbations could be eliminated by better fabrication or filtering. Similar to the Schawlow-Townes limit on a laser's linewidth [207], the ultimate linewidth for an oscillator without stimulated emission is [208] $\delta f_{\rm ult} = f_{\rm M}/4\bar{n}_{\rm p}Q_{\rm M} \sim 0.3$ Hz.

As expected, the feedback circuit succeeds in concentrating nearly the entire output into a narrow spectral line, provided that the oscillator's free-running frequency is close to the target frequency (Fig. 4.6c, d) The stabilisation range is set by the maximum feedback voltage. However, feedback stabilises part of the emission even when this condition is not met, as seen by a weak spectral peak persisting

beyond the expected voltage range (Fig. 4.6d). This indicates that the oscillator occasionally deviates by several linewidths from its central frequency. Feedback makes these excursions visible by temporarily capturing them.

Finally, we demonstrate how to generate a more complex output spectrum by exploiting the non-linear conductance of the SET. A time-varying drain-source voltage modulates the amplitude of the oscillator's output, leading to regular sidebands spaced by the modulation frequency (Fig. 4.6e). Radio-frequency combs have been proposed for precise frequency comparison, as already used in optics [209], and this nanomechanical comb is an alternative to devices based on superconducting resonators [210] or Josephson junctions [195, 211].

4.6 Methods

4.6.1 IQ tomography

To generate the time traces in Fig. 4.3a, the amplified emission is mixed with a local oscillator running at a nominal frequency offset by $\Delta f = 15$ kHz below the mechanical frequency. The local oscillator and the IQ mixer are implemented in a Zurich Instruments UHFLI lock-in amplifier. The mixer's two intermediate-frequency (IF) outputs, corresponding to the two quadratures of the signal and oscillating at frequency Δf, are low-pass filtered with a 100 kHz cutoff to generate the time traces of Fig. 4.3a. Histograms and autocorrelation traces are built up from 1 s of data at each voltage setting. For the data of Fig. 4.4, in which the oscillator frequency changes with gate voltage, the local oscillator is adjusted at each voltage setting to maintain approximately constant frequency offset Δf.

The histograms resulting from these time traces (Fig. 4.3d) were fitted as follows [194], using the fact that $V^2(t)$ is proportional to the number of phonons. Below threshold, the histogram was fitted assuming a quasi-thermal distribution

$$P(V^2) \propto e^{-V^2/V_{\mathrm{T}}^2}, \tag{4.1}$$

with V_{T} as a free parameter. Above threshold, the fit is

$$P(V^2) \propto e^{-(V^2-V_0^2)^2/\sigma_V^4} + A_{\mathrm{T}} e^{-V^2/V_{\mathrm{T}}^2} \tag{4.2}$$

with V_0, σ_V, V_{T} and A_{T} as free parameters, where the two terms represent a Gaussian distribution over phonon numbers and a small quasi-thermal contribution, respectively.

The sharpness of the central spot in Fig. 4.3c compared with the ring in Fig. 4.3c and spot in Fig. 4.3b confirms that these latter features are broadened by intrinsic device noise rather than by detection noise.

4.6.2 Signal autocorrelation

The autocorrelation is defined as

$$g^{(1)}(\tau) \equiv \frac{\langle V_{\mathrm{I}}(t) V_{\mathrm{I}}(t+\tau)\rangle}{\langle V_{\mathrm{I}}^2(t)\rangle}, \tag{4.3}$$

where the expectation value is averaged over a long time trace of 1 s. In Fig. 4.3e, this function is fitted with the exponentially decaying oscillation stated in the caption, with τ_{coh} and Δf as fit parameters. While the fit here is good, at other gate voltages the oscillator sometimes jumps between different frequencies during data acquisition. For Fig. 4.4b, a more general function is therefore used: $g^{(1)}(\tau) = \mu e^{-\tau/\tau_{\mathrm{coh}}} \cos(2\pi\Delta f \tau) + (1-\mu) e^{-\tau/\tau_{\mathrm{filter}}}$. The first term represents the contribution of the oscillator running at its primary frequency, and the second term represents contributions from other frequencies outside the detection bandwidth. The additional fit parameters are μ, the fraction of time at the primary oscillation frequency, and τ_{filter}, the decay time of the other contributions.

The second-order correlation function [131] is

$$g^{(2)}(\tau) \equiv \frac{\langle V^2(t) V^2(t+\tau)\rangle}{\langle V^2(t)\rangle^2}. \tag{4.4}$$

For a perfectly coherent source, $g^{(2)}(\tau) = 1$ at all τ, whereas Gaussian chaotic emission has $g^{(2)}(\tau) = 1 + e^{-\pi(\tau/\tau_{\mathrm{coh}})^2}$. These are the functions plotted in Fig. 4.3f.

4.6.3 Feedback stabilization

In the phase-locked loop used for Fig. 4.6, the amplified emission is first mixed with a local oscillator running at the target frequency to generate a quadrature voltage proportional to the phase error. This error signal is digitised at up to 14.06 MHz and used as input for a proportional-integral-derivative (PID) controller [212] to generate a correction voltage. The correction voltage is filtered with a 350 Hz low-pass cutoff and clipped to a range of ±0.8 mV, before being fed back to gate G1 of the device.

4.7 Theory of self-driven oscillations

4.7.1 Oscillation mechanism

Here we describe a simple model of the self-oscillation mechanism, and explain why the gate voltage settings that lead to self-oscillations usually also coincide with local maxima of the resonance frequency (as seen in Fig. 4.2b, c). The model works in the limit of a slow oscillator, where the phonon energy is much smaller than the energy splitting of the SET. We take a simplified approach to self-oscillations mediated by Coulomb blockade, following especially Refs. [91, 96], which present much more complete theory.

Consider a single quantum dot suspended above a gate held at positive potential V, representing the average potential of the five gates in this experiment (Fig. 4.7). The equation of motion for the displacement u as a function of time t is:

$$m\ddot{u}(t) = -m\Omega_0^2 u(t) - \frac{m\Omega_0}{Q_0}\dot{u}(t) + \frac{q(t)V}{D} \tag{4.5}$$

where $\dot{u}$ denotes a time derivative, m is the suspended mass and $\Omega_0 = 2\pi f_{\mathrm{M}}$ and Q_0 are the bare mechanical resonance frequency and quality factor. The last term describes the electrostatic force on the suspended device: $q(t)$ is the instantaneous charge on the dot and D is a distance (on the order of the separation between nanotube and gate) that relates the gate voltage V to the electric field experienced by the dot.

Electromechanical feedback occurs because the dot charge depends on the displacement [213]. For a very open quantum dot, the characteristic electron tunnel rate Γ_t is much larger than the mechanical frequency ($\Gamma_t \gg \Omega_0$) and so the charge in Eq. (4.5) can be replaced by its instantaneous classical expectation value, set by the displacement:

$$q(t) \to \overline{q}(u(t)). \tag{4.6}$$

However, if the tunnel rate approaches the mechanical frequency ($\Gamma_t \gtrsim \Omega_0$), then we must take account of the time needed to reach an equilibrium charge on the quantum dot, given the changing displacement. The charge lags the displacement by approximately the electron tunnelling time. This is modelled by expanding $\overline{q}$ to lowest order in Γ_t/Ω:

$$\overline{q}(u(t)) \to \overline{q}(u(t - 1/\Gamma_t)) \tag{4.7}$$

$$\approx \overline{q}(u(t) - \dot{u}(t)/\Gamma_t) \tag{4.8}$$

where Γ sets the timescale for the charge on the dot to reach equilibrium. For small displacement, this can further be expanded in u, giving

$$\overline{q}(u(t)) \to \overline{q}(0) + \overline{q}'(0)[u(t) - \dot{u}(t)/\Gamma_t], \tag{4.9}$$

where the prime denotes a spatial derivative. Substituting into Eq. (4.5) then leads to a modified equation of motion, where the electromechanical coupling modifies the resonance frequency and the quality factor as follows:

$$\Omega \to \Omega_0 + \Delta\Omega \tag{4.10}$$

$$Q \to Q_0(1 - 2Q_0\Delta\Omega/\Gamma_t)^{-1}, \tag{4.11}$$

where

$$\Delta\Omega = -\frac{V}{2m\Omega_0 D}\,\overline{q}'(0). \tag{4.12}$$

In the limit of instantaneous electron tunnelling ($\Gamma_t \to \infty$), the resonator's frequency is modified, but not its damping. However, for a slower tunnelling rate, Eq. (4.11)

shows that electron tunnelling also modifies the damping factor. Self-driven oscillations occur when the total damping becomes negative.

The usual situation is for the quantum dot charge to increase monotonically as the chemical potential is decreased, i.e. $V\overline{q}' > 0$. Equation (4.12) shows that the mechanical resonance is then softened and the damping increased, especially near Coulomb peaks where $|\overline{q}'|$ is large [89, 151]. However, at large source-drain bias ($|V_{\mathrm{SD}}| > k_{\mathrm{B}}T, \Gamma_{\mathrm{t}}$), there may be gate voltage configurations where charging is reversed ($V\overline{q}' < 0$), leading to an increase in mechanical frequency. Equation (4.11) predicts that self-oscillations occur when

$$V\overline{q}' < -\frac{m\Omega_0\Gamma_{\mathrm{t}}D}{Q_0}. \tag{4.13}$$

This situation can arise if tunnel rates depend on energy [91, 172]. As shown in Fig. 4.7(a), a change in barrier asymmetry with energy causes the quantum dot occupation to vary non-monotonically, allowing the condition Eq. (4.13) to occur (Fig. 4.7(b)).

This model predicts that the same gate voltage settings that allow self-oscillations will also lead to positive frequency shifts $\Delta\Omega$. This is seen in Fig. 4.2b, c, which plots the driven and undriven power spectrum as a function of gate voltage. The peaks in the undriven spectrum, which are the signature of self-oscillation, correspond to gate voltage ranges where the driven mechanical frequency is above its trendline, indicating that $\Delta\Omega$ is positive. This is as predicted by Eq. (4.11), supporting this electromechanical mechanism as the main driver for the oscillations.

This simple model assumes just two tunnel barriers in the nanotube and therefore a single quantum dot, whereas in a real device disorder along the nanotube can lead to multiple dots, as is indicated in Fig. 4.2: the Coulomb diamonds in Fig. 4.2a are irregular, and the periodicity in Figs. 4.2b, c (measured at a bias larger than the charging energy) does not match the periodicity in Fig. 4.2a. Because the tunnelling rate between two quantum dots is modulated by the chemical level alignment, this may be the more fundamental reason that it is energy-dependent. Thus, some electrostatic disorder may be necessary to satisfy the oscillation criterion Eq. (4.13).

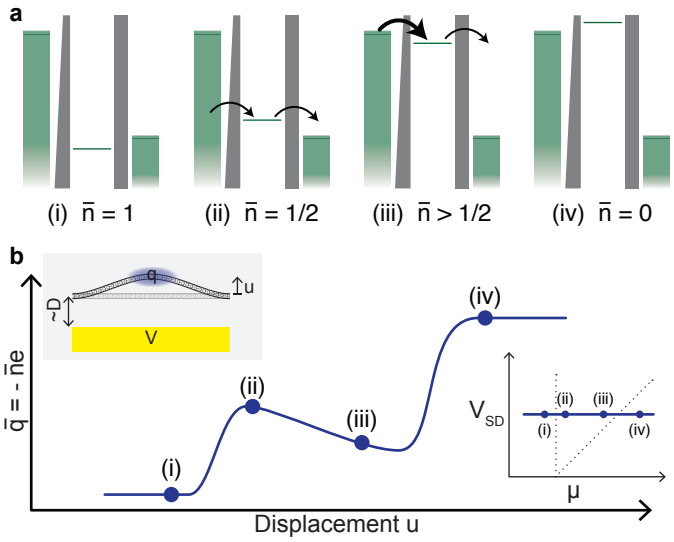


Figure 4.7: Mechanism of self-oscillations. **a**, Chemical potential of dot and leads for four different values of nanotube displacement (assuming gate voltage $V > 0$, and considering only a single level within the bias window). Tunnel barriers are marked by vertical bars, with changing bar thickness denoting energy-dependent tunnel rates. The mean excess electron number $\overline{n}$ is shown for each displacement. **b**, Quantum dot mean charge as a function of displacement. The four configurations sketched in **a** are marked. Near configuration (iii), the condition $V\overline{q}' < 0$ occurs, permitting self-oscillations. Lower inset: The same configurations plotted in a dot stability diagram as a function of bias $V_{\rm SD}$ and chemical potential μ relative to the right lead. Dotted lines mark the alignment of the dot potential with the leads, i.e. the edges of Coulomb blockade diamonds. Upper inset: Sketch of quantum dot displacement above gate.

While this mechanism appears to explain all our data, it is possible that other oscillation mechanisms also contribute. In other nanomechanical resonators, oscillations can emerge through a photothermal mechanism [214, 215] and an analogous electrothermal effect might contribute here since the ohmic heating depends on displacement. However, if this were the only mechanism then the feedback should only be positive for one sign of $\partial I/\partial u$ and therefore of $\partial I/\partial V_{\rm G}$, whereas Fig. 4.4 shows that oscillations occur in regions of both positive and negative current slope.

4.7.2 Quantifying the electromechanical coupling

To compare this nanotube device with other nanomechanical resonators, in this section we quantify the electromechanical coupling. The coupling arises from the extra force exerted on the nanotube by each additional electron on the SET.

Modelling the device for simplicity as a single quantum dot, this force is

$$F_{\mathrm{EM}} = \frac{eV}{C_{\mathrm{S}} + C_2 + C_{\mathrm{D}}} \frac{\partial C_2}{\partial u} \tag{4.14}$$

where $C_{\mathrm{S}}, C_2, C_{\mathrm{D}}$ are the capacitance between to source, gate, drain, respectively. This force can be compared with the quantum zero-point force scale, defined by analogy with the zero-point displacement $u_{\mathrm{ZPM}} \equiv \sqrt{\hbar/2m\Omega_0}$ as $F_{\mathrm{ZP}} \equiv m\Omega_0^2\, u_{\mathrm{ZPM}} = \sqrt{\hbar m\Omega_0^3/2}$. This leads to a dimensionless electromechanical coupling parameter defined as [91]:

$$\lambda \equiv \frac{1}{2}\left(\frac{F_{\mathrm{EM}}}{F_{\mathrm{ZP}}}\right)^2 = \frac{F_{\mathrm{EM}}^2}{\hbar m\Omega_0^3} \sim 170. \tag{4.15}$$

The uncertainty of this estimate is large because of unknown device parameters such as the nanotube mass and diameter. Based on previous characterization of the same device [180], we find that the coupling parameter is in the range $1.6 < \lambda < 26000$. Thus it is probable that the electromechanical force is larger than quantum fluctuations, i.e. the device is in the regime of strong coupling, hence the $\bar{n}\sqrt{\lambda}\varepsilon_{\mathrm{Q}}$ term in Eq. (II.15) in Ref. [93] is not necessarily negligible. A major difference is therefore that our model accounts for the first order contribution of the electromechanical coupling to the spring constant, so the applied force term in Eq. (II.14) in Ref. [93] becomes

$$\begin{aligned}
\mathcal{F}(u) &= -m\Omega_0^2(u + \bar{n}\sqrt{\lambda}\varepsilon_{\mathrm{Q}} + \frac{\dot{u}}{\Omega_0 Q}) && (4.16)\\
&= -m(\Omega_0^2 u + \frac{\bar{n}F_{\mathrm{EM}}}{m} + \frac{\dot{u}\Omega_0}{Q}) && (4.17)\\
&\approx -m[\Omega_0^2 u + \frac{F_{\mathrm{EM}}}{m}(\bar{n}(0) + \frac{\partial \bar{n}}{\partial u}u) + \frac{\dot{u}\Omega_0}{Q}] && (4.18)\\
&= -m((\Omega_0 + \frac{\frac{\partial \bar{n}}{\partial u}F_{\mathrm{EM}}}{2m\Omega_0})^2 u - (\frac{\frac{\partial \bar{n}}{\partial u}F_{\mathrm{EM}}}{2m\Omega_0})^2 u + \frac{F_{\mathrm{EM}}\bar{n}(0)}{m} + \frac{\dot{u}\Omega_0}{Q}), && (4.19)\\
&\approx -m((\Omega_0 + \frac{\frac{\partial \bar{n}}{\partial u}F_{\mathrm{EM}}}{2m\Omega_0})^2 u + \frac{F_{\mathrm{EM}}\bar{n}(0)}{m} + \frac{\dot{u}\Omega_0}{Q}). && (4.20)
\end{aligned}$$

In Eq. 4.19, we again linearize the average charge on dot $\bar{n}$ as a function of displacement u. In Eq. 4.20, the $-(\frac{\frac{\partial \bar{n}}{\partial u}F_{\mathrm{EM}}}{2m\Omega_0})^2 u$ term is neglected in comparison with the $\Omega_0^2 u$ term. Now it is evident that Eq. 4.20 modifies the resonance frequency by

the same amount as in Eq. 4.10. The fluctuation component of the electromechanical coupling also contributes to the damping and diffusion terms of the Fokker-Planck equation, as is shown in Ref. [95], but since they do not exhibit any significant impact on the experiment, we do not include them in our model.

The electromechanical force can also be compared with the thermal fluctuation force, given by $F_{\mathrm{th}} = \sqrt{m\Omega_0^2 k_{\mathrm{B}} T}$, where k_{B} is Boltzmann's constant and T is the temperature. Taking $T = 25$ mK (i.e. assuming that the resonator is fully thermalised), we can calculate a corresponding thermal coupling parameter

$$\lambda_{\mathrm{th}} \equiv \frac{1}{2}\left(\frac{F_{\mathrm{EM}}}{F_{\mathrm{th}}}\right)^2 = \frac{\hbar\Omega_0}{2k_{\mathrm{B}}T}\lambda \sim 37, \tag{4.21}$$

showing that the electromechanical force fluctuations probably also dominate the thermal fluctuations.

4.7.3 Phonon number and minimal linewidth

Phonon number

In this section we estimate the number of phonons in the oscillator. Similar to a laser, the mean phonon number $\bar{n}_{\mathrm{p}}$ can be deduced from the emission power P_{total} using

$$\bar{n}_{\mathrm{p}} = \frac{P_{\mathrm{total}}}{\kappa h f_{\mathrm{M}}}, \tag{4.22}$$

where $\kappa \equiv 2\pi f_{\mathrm{M}}/Q_{\mathrm{M}}$ is the mechanical decay rate. This equation assumes that all of the oscillator's energy is lost by electrical emission, and is therefore a lower bound on the phonon number. From the linewidth in Fig. 4.2b, we extract $\kappa = 2\pi\times(13\pm7)$ kHz. The emitted power P_{total} is extracted from a Lorentzian fit to the emission spectrum. For Fig. 4.4b, this leads to a phonon number

$$\bar{n}_{\mathrm{p}} = 1.2^{+1.3}_{-0.4} \times 10^4, \tag{4.23}$$

with the error bar dominated by the uncertainty in κ. The corresponding oscillation amplitude can be calculated from the zero-point amplitude:

$$u_{\mathrm{RMS}} = u_{\mathrm{ZPM}}\sqrt{2\bar{n}_{\mathrm{p}}} = 200^{+360}_{-130}\ \mathrm{pm}, \tag{4.24}$$

again subject to large uncertainty in the device parameters [180].

Minimal linewidth

Quantum uncertainty predicts a minimal linewidth for an oscillator containing a given number of quanta. For a conventional laser, this is the famous Schawlow-Townes linewidth [207]. For a general oscillator, the limit is reduced by a factor of two, giving the ultimate linewidth

$$\delta f_{\mathrm{ult}} = \frac{\kappa/2\pi}{4\bar{n}_{\mathrm{p}}}. \tag{4.25}$$

This limit is set ultimately by the quantum statistics of the boson mode, and is therefore independent of the oscillator mechanism [208]. For the configuration of Fig. 4.6, the emission power is similar to that in Fig. 4.3c, leading to a similar phonon number (Eqs (4.22)-(4.23)). Equation (4.25) therefore predicts $\delta f_{\mathrm{ult}} \approx 0.3$ Hz.

4.7.4 Consequences of anharmonicity

We now extend the theory of Section 4.7.1 to incorporate an anharmonic restoring force. As we shall show, this non-linearity has several consequences for the injection-locked oscillator, modifying the locking range and leading to satellite peaks in the oscillator's emission spectrum as seen in Fig. 4.5.

We model the non-linearity by considering a driven oscillator and introducing a Duffing-type restoring force $\tilde{\eta}u^3$ in the equation of motion:

$$m\ddot{u}(t) + m\Omega^2 u(t) + m\tilde{\Gamma}(u)\dot{u}(t) + \tilde{\eta}u^3(t) = \tilde{F}\cos\omega_{\mathrm{F}}t \tag{4.26}$$

Here Ω is the resonance frequency, ω_{F} is the driving frequency, $\tilde{F}$ is the driving force, and $\tilde{\eta}$ is the Duffing parameter. We must also incorporate explicitly the displacement dependence of the damping term $\tilde{\Gamma}(u) \equiv \frac{\Omega}{Q(u)}$. To do this, we expand it to second order in u:

$$\tilde{\Gamma}(u) = \tilde{\Gamma}^{(0)} + \tilde{\Gamma}^{(1)}u + \tilde{\Gamma}^{(2)}u^2. \tag{4.27}$$

In the rest of this section, we solve Eq. (4.26) and derive the consequences for the emission spectrum in Fig. 5. We follow an approach recently pioneered for anharmonic resonators [203], which for the first time explained satellite peaks

similar to those of Fig. 5f; however we extend the approach to the case of an anharmonic oscillator.

Deriving a Hamiltonian in the rotating frame

We begin by transforming Eq. (4.26), to a frame rotating at the drive frequency by writing:

$$u = q\,\mathrm{e}^{\mathrm{i}\omega_\mathrm{F} t} + \mathrm{c.c.} \tag{4.28}$$

where $q(t)$ is a complex displacement amplitude and c.c. denotes the complex conjugate. In the rotating frame approximation all terms fluctuating as $\mathrm{e}^{\pm 2\mathrm{i}\omega_\mathrm{F} t}$ or faster are neglected, $q(t)$ is assumed to evolve only much slower than $1/\omega_\mathrm{F}$, and Γ is assumed small so that terms proportional to $\Gamma\dot{q}$ are neglected. In this approximation, Eq. (4.26) becomes the following equation of motion in the rotating frame:

$$(-\omega_\mathrm{F}^2 + \Omega^2)q + 2\mathrm{i}\omega_\mathrm{F}\dot{q} + \mathrm{i}\omega_\mathrm{F}\Gamma(q)q + \frac{3\tilde{\eta}}{m}|q|^2 q = \frac{\tilde{F}}{2m}, \tag{4.29}$$

with amplitude-dependent damping factor

$$\Gamma(q) = \tilde{\Gamma}^{(0)} + \tilde{\Gamma}^{(2)}|q|^2. \tag{4.30}$$

Since the free-running oscillator has constant energy, we must have $\Gamma(R) = 0$, where R is the magnitude of the free-running amplitude q. Therefore we can re-express Eq. (4.30) as

$$\Gamma(q) = \tilde{\Gamma}^{(2)}(|q|^2 - R^2). \tag{4.31}$$

We now rearrange Eq. (4.29) to obtain an equation in hamiltonian form:

$$\dot{q} = -\mathrm{i}\delta q + \mathrm{i}\frac{\eta}{2}q^2 q^* - \mathrm{i}\frac{F}{2} - \frac{\Gamma(q)}{2}q \tag{4.32}$$

$$= \mathrm{i}\,\frac{\partial \mathcal{H}}{\partial q^*} - \frac{\Gamma(q)}{2}q, \tag{4.33}$$

where the Hamiltonian function is

$$\mathcal{H}(q) = \frac{\eta}{4}|q|^4 - \delta|q|^2 - \frac{F}{2}(q + q^*) \tag{4.34}$$

and we have defined the frequency detuning $\delta \equiv \omega_\mathrm{F} - \Omega \ll \Omega$, and normalized parameters $\eta \equiv \frac{3\tilde{\eta}}{m\omega_\mathrm{F}}$ and $F \equiv \frac{\tilde{F}}{2m\omega_\mathrm{F}}$.

Steady-state behaviour

When the oscillator is driven, the condition for it to be injection-locked is that it evolves at the same frequency as the drive, i.e. that $q(t)$ is stationary in the rotating frame. To see the conditions for this to occur, we express q and $\mathcal{H}$ in polar coordinates:

$$q(t) = r(t)\,\mathrm{e}^{\mathrm{i}\theta(t)} \tag{4.35}$$

$$\mathcal{H}(r,\theta) = \frac{\eta}{4}r^4 - \delta r^2 - Fr\cos\theta. \tag{4.36}$$

The equations of motion are:

$$\frac{dr}{dt} = -\frac{1}{2r}\frac{\partial\mathcal{H}}{\partial\theta} - \frac{\Gamma(r)}{2}r = -\frac{F}{2}\sin\theta - \frac{\Gamma(r)}{2}r \tag{4.37}$$

$$\frac{d\theta}{dt} = \frac{1}{2r}\frac{\partial\mathcal{H}}{\partial r} = \frac{\eta}{2}r^2 - \delta - \frac{F}{2r}\cos\theta. \tag{4.38}$$

To evaluate the stationary solutions of Eqs. (4.37)-(4.38) we set the time derivatives to zero, giving:

$$\sin\theta = \frac{r\Gamma(r)}{F} \tag{4.39}$$

$$\eta r^2 - 2\delta - \frac{F}{r}\sqrt{1 - \left(\frac{r\Gamma(r)}{F}\right)^2} = 0. \tag{4.40}$$

The solutions of Eqs. (4.39)-(4.40) describe the steady-state vibrations of the driven oscillator.

Figure 4.8 shows the hamiltonian function, marked with the stationary points obtained from Eqs. (4.39)-(4.40) in the limit of weak damping. The instantaneous state of the oscillator corresponds to a point in this hamiltonian landscape. If this is not a stable stationary point, Eq. (4.33) predicts that without damping it will evolve following the contours, with damping eventually causing it to settle at a stable stationary point.

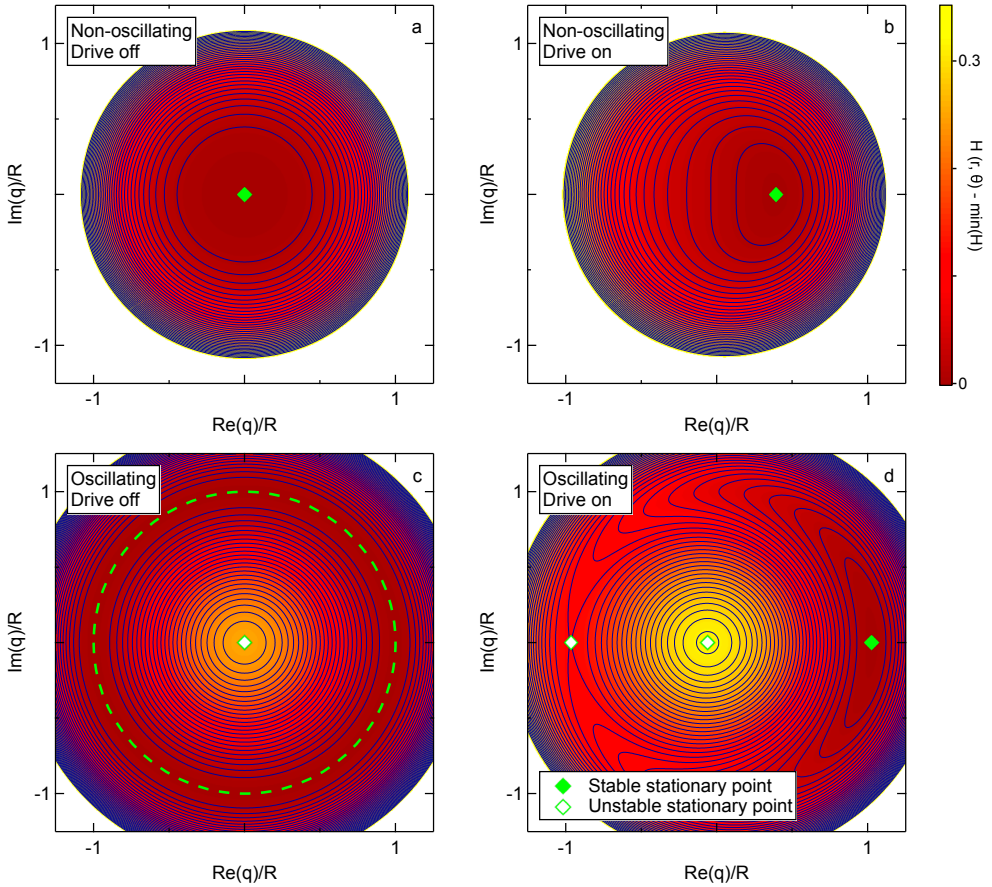


Figure 4.8: Hamiltonian function in the rotating frame. Equation (4.36), plotted as both colour and contour map, for four different situations. **a** Without self-oscillations ($\Gamma > 0$), no drive ($F = 0$). **b** Without self-oscillations, drive on ($F = 0.06$). **c** With self-oscillations ($\tilde{\Gamma}^{(0)} < 0$), drive off. **d** With self-oscillations, drive on ($F = 0.06$). In all panels, $\eta = 1$ and the drive detuning has been chosen equal to the free-running oscillator frequency ($\delta = \eta R^2/2$). For panels **a** and **b**, there is a single stable stationary point. In panel **c**, there is a stationary point at $q = 0$ made unstable by the negative damping, and a ring of metastable stationary points (dashed circle) that correspond to free-running oscillator states. In panel **d**, there are one stable and two unstable stationary points. Fluctuations about the stable points give rise to sidebands in the emission spectrum, with the sideband offset frequency being given by the confinement frequency in the hamiltonian potential. Squeezing occurs when the potential is locally anisotropic. While some squeezing occurs for the driven non-oscillating resonator (panel **b**), squeezing becomes much stronger for the oscillator. On the dashed circle in panel **c**, the squeezing parameter φ is infinite.

Range of injection locking

In an injection locking experiment as in Fig. 4.5, the oscillator can only be captured if there exists a solution to Eqs. (4.40)-(4.39) for the chosen drive strength F and detuning δ. For a linear oscillator ($\eta = 0$), this range is given by Adler's theory of injection locking [198, 216]. Here we extend this theory to the case of a non-linear oscillator. Using Eq. (4.31) we can rewrite Eq. (4.40) as:

$$\delta = \frac{\eta}{2}\left(R^2 + \frac{\Gamma}{\Gamma^{(2)}}\right) - \frac{F}{2r}\cos\theta \tag{4.41}$$

$$= \frac{\eta R^2}{2} - \frac{F}{2r}\left(\frac{2\eta}{\Gamma^{(2)}}\sin\theta + \cos\theta\right) \tag{4.42}$$

where the second step follows from Eq. (4.39). The locking range is determined by the extremal values of the right-hand side. With $\eta = 0$ and assuming weak driving so that $r \approx R$, and by considering the locking range $\Delta\delta \equiv 2\pi\Delta f_{\mathrm{D}}$ outside which Eq. (4.42) has no solutions, we recover Adler's result for the power dependence:

$$\Delta\delta = F/2R = \tilde{F}/4m\omega_{\mathrm{F}}R \propto P_{\mathrm{D}}^{1/2} \tag{4.43}$$

However, in the limit of strong drive, we find

$$\Delta\delta = \frac{F}{2r}\sqrt{1 + \left(\frac{2\eta}{\Gamma^{(2)}}\right)^2} \tag{4.44}$$

which allows for a more complicated power dependence because r depends on the driving force according to Eq. (4.40). In the simplest case of strong driving we have

$$r = \left(\frac{F}{\eta}\right)^{1/3} \tag{4.45}$$

giving

$$\Delta\delta = \frac{\eta^{1/3}F^{2/3}}{2}\sqrt{1 + \left(\frac{2\eta}{\Gamma^{(2)}}\right)^2} \propto P_{\mathrm{D}}^{1/3}. \tag{4.46}$$

This is in better agreement with the data of Fig. 4.5e than is Eq. (4.43), and confirms that the Adler theory of injection locking is modified by the anharmonicity of this device.

Satellite peaks

To understand the origin of the satellite peaks in Fig. 4.5f, consider the evolution of the oscillator when perturbed away from the stationary state given by Eqs. (4.40)-(4.39). We can write $(r, \theta) = (\overline{r} + \epsilon_r, \overline{\theta} + \epsilon_\theta)$, where $(\overline{r}, \overline{\theta})$ is a stable stationary point and $(\epsilon_r, \epsilon_\theta)$ is a small perturbation. To lowest order in Γ and in $(\epsilon_r, \epsilon_\theta)$, the equation of motion derived from Eqs. (4.37)-(4.38) is:

$$\begin{pmatrix} \dot{\epsilon_r} \\ \dot{\epsilon_\theta} \end{pmatrix} = \frac{1}{2\overline{r}} \begin{pmatrix} -\mathcal{H}_{r\theta} - \overline{r}\Gamma_\epsilon/2 & -\mathcal{H}_{\theta\theta} \\ \mathcal{H}_{rr} & \mathcal{H}_{r\theta} \end{pmatrix} \begin{pmatrix} \epsilon_r \\ \epsilon_\theta \end{pmatrix} \tag{4.47}$$

where the subscripts denote partial derivatives, and the damping factor is $\Gamma_\epsilon \equiv 2\Gamma + \overline{r}\Gamma'(\overline{r})$. This can be written in the form of an effective Hamiltonian equation by defining $\epsilon \equiv \epsilon_r + i\overline{r}\epsilon_\theta$, which obeys the equation of motion:

$$\dot{\epsilon} = i\frac{\partial \mathcal{H}^{\text{eff}}}{\partial \epsilon^*} - \frac{\Gamma_\epsilon}{2}(\epsilon + \epsilon^*) + \frac{\mathcal{H}_{r\theta}}{\overline{r}}\epsilon^* \tag{4.48}$$

with effective hamiltonian:

$$\mathcal{H}^{\text{eff}}(\epsilon) = -\left(\mathcal{H}_{rr} + \frac{\mathcal{H}_{\theta\theta}}{\overline{r}^2}\right)\frac{|\epsilon|^2}{4} - \left(\mathcal{H}_{rr} - \frac{\mathcal{H}_{\theta\theta}}{\overline{r}^2}\right)\frac{\epsilon^2 + (\epsilon^*)^2}{8}. \tag{4.49}$$

This effective hamiltonian describes a potential well in which the perturbed state vector moves, following elliptical orbits in $(\epsilon_r, \overline{r}\epsilon_\theta)$ space.

The frequency and aspect ratio of these orbits can be calculated from the principal frequencies derived by diagonalizing Eq. (4.49). The orbital frequency is:

$$\omega_{\text{side}} = \sqrt{\omega^{(1)}\omega^{(2)}} \tag{4.50}$$

where

$$\omega^{(1)} = \mathcal{H}_{rr}/2 \quad = \frac{3\eta\overline{r}^2}{2} - \delta \tag{4.51}$$

$$\omega^{(2)} = \mathcal{H}_{\theta\theta}/2\overline{r}^2 = \frac{F}{2\overline{r}}\cos\theta. \tag{4.52}$$

We can now understand the satellite peaks evident in Fig. 4.5f. Under the influence of stochastic force noise (for example thermal noise), the system fluctuates in the vicinity of its stable point. While the phase of these fluctuations is random, the characteristic frequency is given by Eq. (4.50). When transformed from the rotating

frame to the lab frame, these fluctuations give rise to sidebands in the power spectrum of the displacement at frequency $\omega_{\rm F} \pm \omega_{\rm side}$, where $\Delta f_{\rm side} = \omega_{\rm side}/2\pi$.

We now compare the predicted orbital frequency to the observed sidebands. Assuming weak damping, Eq. (4.39) tells us that $\theta \approx 0$. We further assume strong driving so that Eq. (4.45) holds and we can neglect the second term in Eq. (4.51) compared with the first term. Equation (4.50) then predicts:

$$\omega_{\rm side} = \frac{\sqrt{3}}{2}\eta^{1/3}F^{2/3} \propto P_{\rm D}^{1/3}. \tag{4.53}$$

This is in fairly good agreement with the data of Fig. 4.5g.

Classical squeezing

The difference between the principal frequencies gives rise to squeezing, because the system is more susceptible to force perturbations along one coordinate axis. The degree of squeezing is set by the aspect ratio of the orbital ellipses, which is

$$\sqrt{\omega^{(1)}/\omega^{(2)}} = e^{2\varphi} \tag{4.54}$$

where φ is the squeezing parameter, defined by this equation [203]. This ratio depends on the drive strength and on the detuning.

Substituting from Eqs. (4.51)-(4.52) and using the constraint (4.40), we find:

$$e^{4\varphi} = 1 + \frac{2\eta\overline{r}^3}{F\cos\theta}. \tag{4.55}$$

We can thus identify three regimes:

1. If $\eta = 0$ we have $\varphi = 0$, i.e. no squeezing, as expected for a harmonic oscillator.

2. When the driving is strong ($\overline{r} = (F/\eta)^3 \gg R$) so that the oscillator's self-excitation can be neglected, and damping is weak ($\theta \to 0$), then we find $e^{4\varphi} = 3$, i.e. moderate squeezing. This regime was recently studied using a nanowire resonator [203].

3. Strong squeezing is achieved when the driving is weak enough that the displacement is near the free-running amplitude, i.e. $\overline{r} = R > (F/\eta)^3$. In fact, for zero drive strength ($F \to 0$), the squeezing parameter $\varphi \to \frac{1}{4}\ln(\eta R^3/2F)$ approaches infinity.

In the work of Ref. [203], it was demonstrated that the squeezing parameter can be read off by comparing the intensities of the two satellites, which are in the ratio of $\tanh^2\varphi$. In the non-oscillating but weakly damped case, this intensity ratio cannot exceed $\tanh^2(\frac{1}{4}\ln 3) \approx 0.07$. However, Fig. 4.5f shows that the two intensities are nearly equal, which confirms that the non-linear oscillator enters a more squeezed state than a driven non-linear resonator does. This symmetry of the two satellite intensities is a clear difference between the behaviour of an anharmonic oscillator compared with an anharmonic resonator.

Surprisingly, the satellite intensity ratio indicates that the oscillator is in the regime of weak driving while the satellite frequency is more consistent with strong driving. This is possibly a consequence of the approximation made in Eq. (4.45) for the amplitude under strong driving. A detailed calculation would require an exact solution of Eq. (4.40); however, this would involve more free parameters and require the functional form of $\Gamma(r)$.

Numerically fitting the satellite frequency outside the strong-driving limit.

In this section we explain the numerical fit (solid lines) in Fig. 4.5g, which goes beyond the strong-driving approximation, Eq. (4.53). We solve Eqs. (4.39)-(4.40) under the assumption that the damping force is negligible compared with both the Duffing effect and the driving force, so that $\theta \to 0$. Equation (4.40) then becomes:

$$\underline{\eta}\underline{r}^3 - 2\underline{r}\delta - \sqrt{P_{\rm D}} = 0, \tag{4.56}$$

where $\underline{\eta} \equiv A_{\rm EM}^2\eta$ and $\underline{r} \equiv r/A_{\rm EM}$ are rescaled parameters, and we have defined the electromechanical scaling factor $A_{\rm EM} \equiv F/\sqrt{P_{\rm D}}$. The frequency offset $\delta = 15$ kHz is directly read off from data similar to Fig. 4.5f, assuming that the resonator frequency Ω is equal to the free-running oscillation frequency.

Since all parameters in Eq. (4.56) except $\underline{\eta}$ and $\underline{r}$ are known, it is an implicit equation for $\underline{r}(\underline{\eta})$, which can be solved numerically to give solution $\underline{r}_0$. Substituting this solution into Eq. (4.50) gives for the sideband frequency:

$$\omega_{\text{side}} = \sqrt{\left(\frac{3\underline{\eta}\underline{r}_0^2}{2} - \delta\right)\left(\frac{\underline{\eta}\underline{r}_0^2}{2} - \delta\right)} = \sqrt{\left(\frac{3\eta r_0^2}{2} - \delta\right)\left(\frac{\eta r_0^2}{2} - \delta\right)}. \tag{4.57}$$

where r_0 is the un-scaled amplitude corresponding to $\underline{r}_0$. Note that this frequency prediction is independent of the unknown scaling factor A_{EM}.

We therefore now have a function to predict the sideband frequency from the driving power using only one fit parameter $\underline{\eta}$. This is the function used to fit each of the three datasets in Fig. 4.5g. This model is more accurate in both the strong- and weak- driving limit than the simple function $\Delta f_{\text{side}} = BP_{\text{D}}^{1/3}$, where B is the free parameter (dashed lines).

4.8 Characterizing the displacement sensitivity

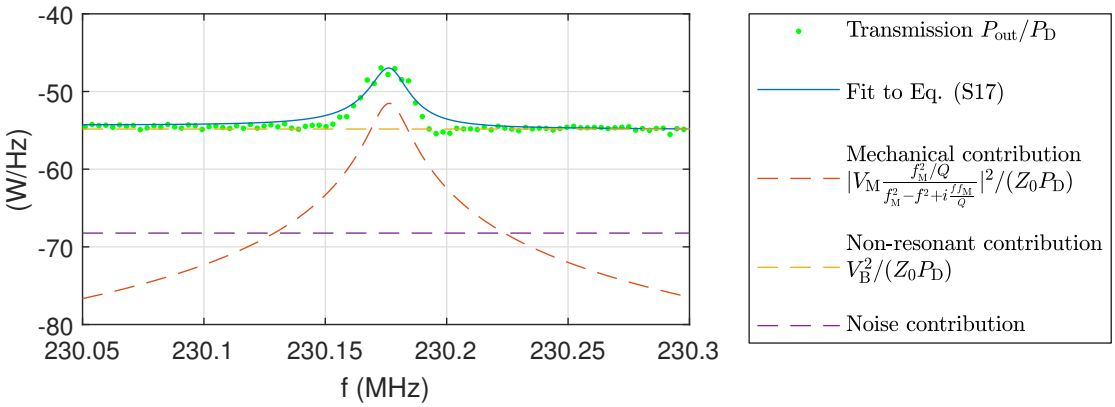


Figure 4.9: Extracting the measurement imprecision Points: measured transmission as a function of drive frequency, taken from a vertical cut through Fig. 4.2b at $V_{\text{G}} = -1907$ mV. Red curve: Fit using Eq. (4.58). Yellow curve: Electromechanical contribution, proportional to the first term in Eq. (4.58). Purple curve: Non-resonant contribution, proportional to the second term in Eq. (4.58). Green curve: Noise contribution, proportional to the third term in Eq. (4.58).

As shown in Fig. 2.1, the cryogenic setup is almost identical to that in the previous chapter, with the main difference being the addition of the SQUID amplifier. We therefore use a similar method to characterize the displacement sensitivity, by comparing the measurement imprecision voltage with the signal voltage generated

by a driven vibration. The measurement noise is read off from the background in Fig. 4.2c, from which we find $\sqrt{S_{VV}} = \sqrt{-192 \text{ dBm/Hz} \times Z_0} = 56 \text{ pV}/\sqrt{\text{Hz}}$. The signal voltage is deduced from Fig. 4.2b. As in Ref. [180], we must perform our analysis at a gate voltage setting for which the nanotube does not oscillate, so that the displacement can be deduced from the drive voltage assuming linear response. In this case we choose $V_\text{G} = -1907$ mV.

Figure 4.9 plots a vertical cut through Fig. 4.2b, showing the mechanical resonance as a peak in the transmitted power. We fit this data with the expected peak shape derived in the previous chapter:

$$P_\text{out}(f) = \frac{1}{Z_0}\left|V_\text{M}\frac{f_\text{M}^2/Q}{f_\text{M}^2 - f^2 + i\frac{f f_\text{M}}{Q}} + V_\text{B}e^{i\phi_\text{B}}\right|^2 + \frac{S_{VV}\Delta f}{Z_0}. \tag{4.58}$$

Here the first term inside the modulus sign describes the mechanical signal with peak amplitude V_M, the second term inside the modulus sign describes non-resonant electrical coupling to the tank circuit with amplitude V_B and phase ϕ_B, and the last term is detection noise, which depends on the resolution bandwidth Δf. The fit parameters are f_M, Q, V_M, V_B, and ϕ_B. Figure 4.9 also shows the contributions of the different terms in Eq. (4.58) to the measured signal.

The displacement sensitivity is deduced from the peak electromechanical signal V_M, using the estimated driven vibration amplitude $u_\text{RMS} = 87^{+2200}_{-83}$ pm:

$$\sqrt{S_{uu}} = \frac{u_\text{RMS}}{V_\text{M}}\sqrt{S_{VV}} \tag{4.59}$$

$$= 0.735^{+19}_{-0.700} \text{ pm}/\sqrt{\text{Hz}}, \tag{4.60}$$

where the large uncertainty stems from the unknown device geometry and mass [180]. This sensitivity is thus probably somewhat worse than in Chapter. 3, most likely because the mechanical frequency is no longer near a maximum of the cryostat's output transmission spectrum. The sensitivity should also depend on the steepness of the SET's transconductance, which depends on device tuning.

This sensitivity can also be expressed as a number of added noise phonons n_nf by comparing it to the imprecision of a phase-preserving amplifier in the

standard quantum limit [116]:

$$n_{\mathrm{nf}} = \frac{S_{uu}}{2\,S_{uu}(\mathrm{SQL})} \tag{4.61}$$

$$= 6940^{+1300000}_{-6860} \tag{4.62}$$

where [180]

$$S_{uu}(\mathrm{SQL}) = \frac{\hbar Q}{4\pi^2 m f_{\mathrm{M}}^2}. \tag{4.63}$$

Since the central estimate corresponds to a temperature of $n_{\mathrm{nf}}\,hf_{\mathrm{M}}/k_{\mathrm{B}} = 76$ K, this explains why we could not resolve Brownian motion in the undriven spectrum, even by averaging.

The measurement precision is here limited by amplifier noise [180]. To improve it, the SET should be fabricated to give a larger transconductance, and the tank circuit could be improved to give a larger conversion of current to signal voltage at the mechanical frequency.

The analysis of this section also leads to an independent estimate of the oscillation amplitude calculated in Sec. 4.7.3. From Fig. 4.9, an estimated driven amplitude of $u_{\mathrm{RMS}} \sim 87$ pm leads to an emission power of $V_{\mathrm{M}}^2/Z_0 = 890$ zW. The emission power in Fig. 3c is 145 aW, which therefore corresponds to ~ 1 nm, just outside the range of Eq. (4.24)

4.9 Supplementary data

4.9.1 Mechanical linewidth through the oscillation threshold

This section is dedicated to the bias-dependence of the self-oscillation linewidth. In Fig. 4.10b we sweep V_{DS} from 0 to 3 mV for a fixed $V_{\mathrm{G}} = -1885.8$ mV. Four typical vertical cuts are plotted in Fig. 4.10a and fitted with Lorentzian functions. With increasing bias, the peak becomes taller and narrower. From the fitting we extract the peak linewidth and power gain, which we plot in Fig. 4.10c. It can be seen from Fig. 4.10c that the total power gain and the linewidth both increase with increasing bias until $V_{\mathrm{DS}} = 1$ mV, then the gain saturates while the linewidth narrows down.

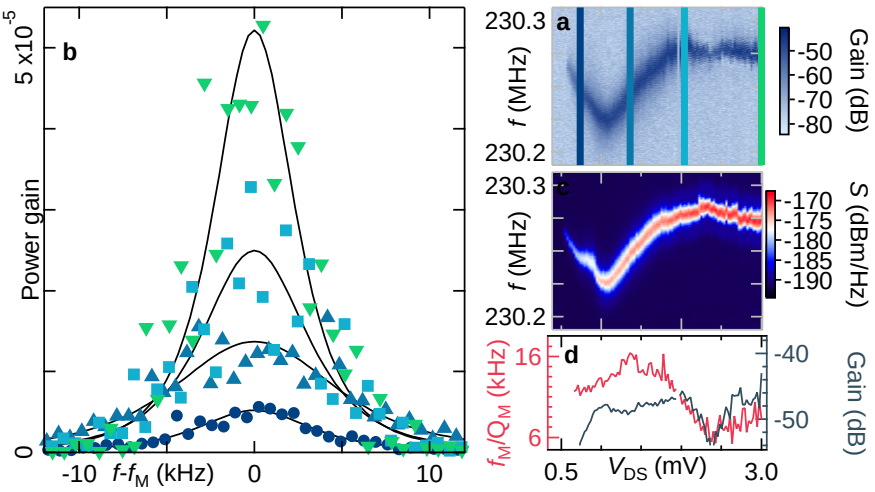


Figure 4.10: The linewidth as a function of the bias voltage. **a**, Gain spectrum $P_{\mathrm{out}}/P_{\mathrm{D}}$ for different bias voltage settings below and above the oscillation threshold. The gate voltage is fixed at $V_{\mathrm{G}} = -1885.8$ mV. **b**, Points: Four selected spectra from **a** (bias settings marked by vertical lines). Curves: Lorentzian fits, with peak gain and linewidth as free parameters. **c**, Self-oscillation emission spectrum without the TG driving. **d**, Peak gain and linewidth $f_{\mathrm{M}}/Q_{\mathrm{M}}$ across the entire range of **a**, extracted by Lorentzian fits as in **b**.

Finally, we compare the emission linewidth in the self-oscillation scenario and the driven scenario. In Ref. [180], we showed that the linewidth of the driven response is limited by SET-induced damping, while in the self-oscillation regime, where the energy decay time becomes infinite, the linewidth is therefore dominated by the flicker noise, possibly from the surface charge fluctuation.

4.9.2 Resonance linewidth

Because the mechanical damping rate is affected by the SET configuration, the linewidth varies strongly with gate voltage. We extract the resonance linewidth over the entire voltage range in Fig. 4.2b and calculate its histogram. It can be seen that the average linewidth across the gate voltage range is 13 kHz.

4.9.3 Self-oscillation frequency stability

To verify the dominant noise that limits the oscillation linewidth, in this section we analyze the frequency stability of the SET-driven resonator via its Allan deviation (ADEV) $\sigma_{\mathrm{Allan}}(\tau)$, as defined in Sec. 1.6. The clock accuracy of both the locking amplifier and the Alazartech data acquisition card is less than 2 ppm, hence

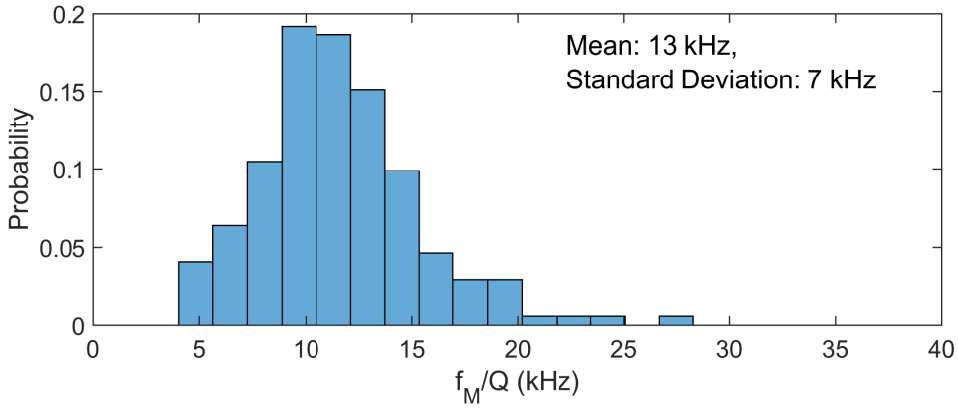


Figure 4.11: Histogram of resonance linewidth. A histogram of the Fano linewidth in each transmission spectrum in Fig. 4.2b as a function of the gate voltage.

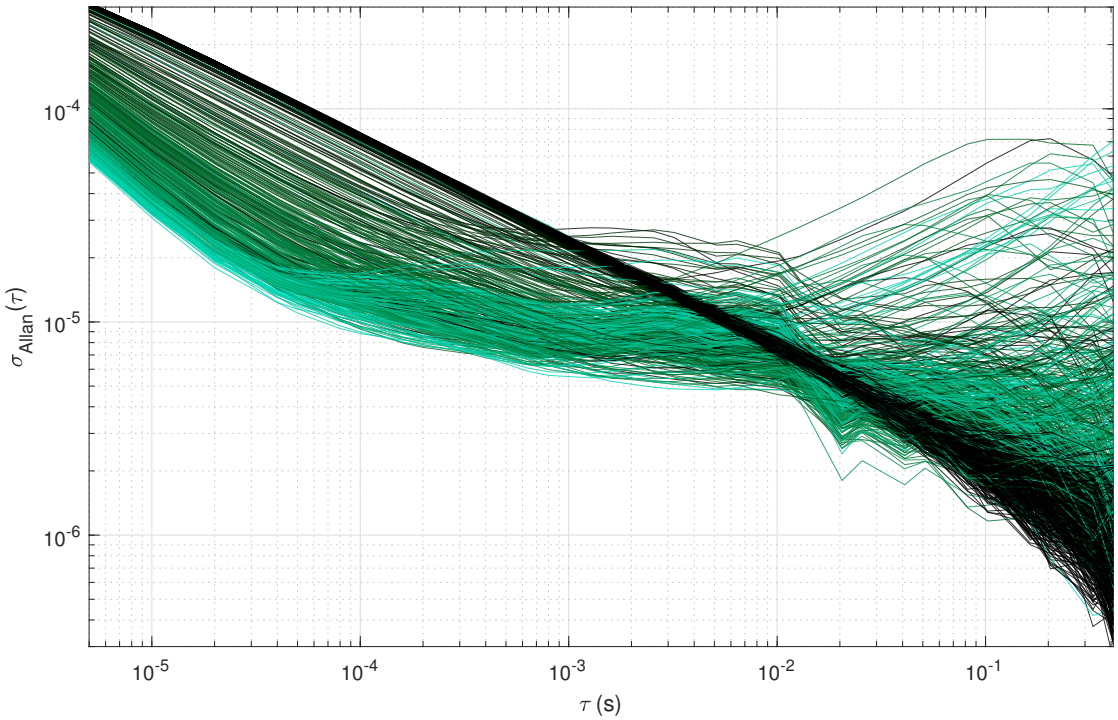


Figure 4.12: The Allan deviation $\sigma_{\mathrm{Allan}}(\tau)$ of the self-oscillation signal for 1 s, plotted in a double-logarithmic scale. $V_{\mathrm{G}} = -1880$ mV to -1700 mV. Brighter color indicates higher RF power.

negligible compared to the frequency instability of the nanotube self-oscillation. We record the heterodyne signal $V_{\mathrm{I}}(t)$ and $V_{\mathrm{Q}}(t)$ for one second, digitized with the ADC card at a sampling rate $f_{\mathrm{SA}} = 1$ MHz. The heterodyne signal is first passed through a 100 kHz LPF to reduce the noise, then converted into a polar coordinate $(\rho(t), \theta(t))$. Substitute $\theta(t)$ into Eqs. (1.28)-(1.29) as the phase deviation readings, we can now calculate the ADEV of the oscillation signal.

Using a MATLAB script from Ref. [217], we apply such analysis to the heterodyne record of other gate voltage configurations and plot them in Fig. 4.12, where the brightness of the curve color indicates the power of the received signal. We can see from the figure that the black traces, corresponding to zero RF emission, fit to a slope $\alpha = -1/2$, which is exactly what we expect for the ADEV of pure white noise [132, 218]. when the nanotube oscillates, we receive a combination of the signal and the instrumental white noise. The higher SNR reduces the imprecision noise, and reveals the phase noise in the lower τ range. For the maximum self-oscillation power, it can be seen that the ADEV is flat between $\tau = 10^{-4}$ s and 10^{-2} s. This indicates that the free-running linewidth is dominated by the flicker frequency modulation noise [132], which is slow enough to be compensated by the feedback loop.

It should be noticed, however, that because the sampling rate is much lower than the oscillation frequency, and that the input signal is filtered by a 100 kHz LPF in the lock-in amplifier, we are not able to trace the phase deviation of oscillation signal that drifts for more than 2π from the LO per sampling interval, which effectively sets an upper bound for the ADEV of the non-emitting signal in Fig. 4.12. The actual ADEV for pure white noise input would be actually higher.

Finally, we compare this observation with a recent work [218] on a similar resonator. Both resonators achieved a minimum ADEV $\sim 10^{-5}$ despite the different means of measurement and bias regime used in the two experiments, confirming our $\sigma_{\mathrm{Allan}}(\tau)$ is not limited by imprecision noise. Instead, this suggests there is possibly a common source of frequency instability for both devices. However, we note in Ref. [218] the authors reported an unexpected power exponent $\alpha = 1/4$. Further research is still needed to understand the exact reason behind such disagreement.

4.9.4 Thermal Dependence

Although we did not measure the autocorrelation as a function of temperature, we did measure the emission spectrum from base temperature up to 700 mK. As seen in Fig. 4.13, there is no observable change in the linewidth, implying that the coherence time is independent of temperature over this range.

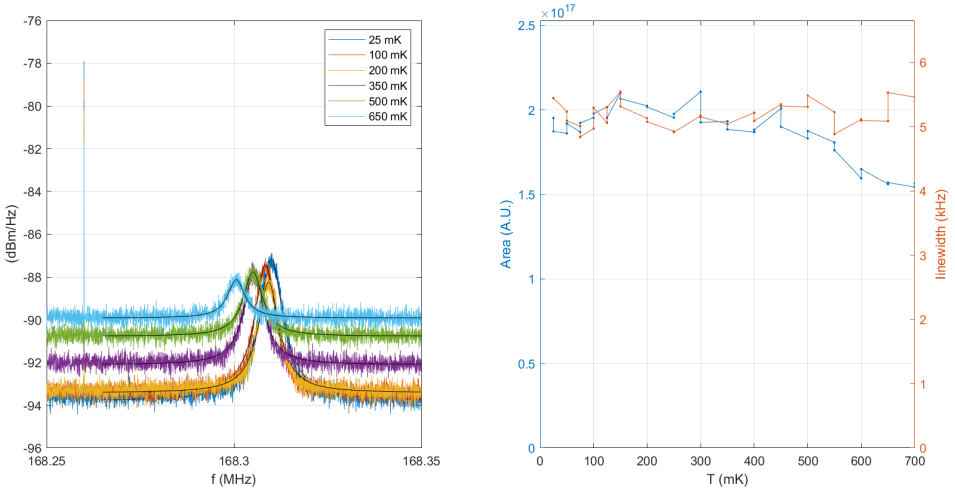


Figure 4.13: The linewidth as a function of the bias voltage. Left: Emission spectrum measured at different cryostat temperatures. The central peak is the oscillator output; the narrow peak on the left is a tone injected into the SQUID to monitor its gain. Right: Fitted peak area (left axis) and linewidth (right axis) as a function of temperature. There is no observable thermal broadening.

4.9.5 Further characterization of the emission sidebands

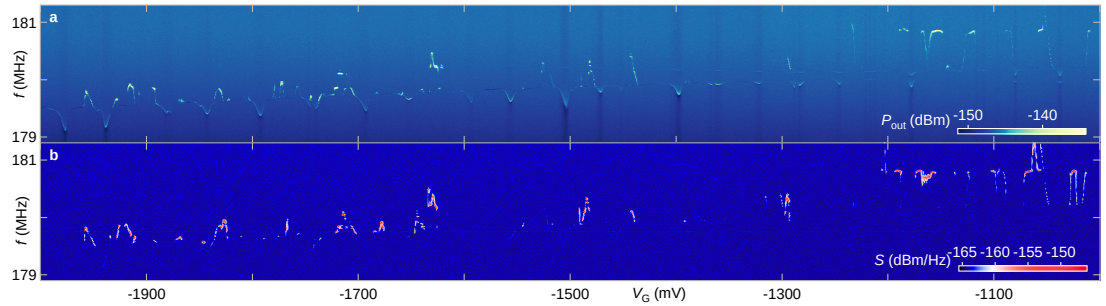


Figure 4.14: Transmission and emission spectra from a previous cool-down. **a**, Mechanical resonance detected in a transmission measurement. The nanotube is biased with $V_{DS} = 5$ mV and driven with power $P_{in} = -120$ dBm at gate G2. **b**, Emission spectrum under the same conditions but with no drive applied.

In this section we discuss the origin of the various sideband peaks in the RF spectra. Most of the sideband peaks in Fig. 4.2c and Fig. 4.5ab appear at a fixed frequency offset from the central peak. These are due to a frequency mixing in the SQUID amplifier, which persists for an external RF source, and they can be eliminated by turning off the SQUID. As a comparison to Fig. 4.2bc, in Fig. 4.14 we plot the transmission (a) and emission (b) spectra taken from the previous cool-down when the SQUID was not installed, and note the sidebands disappear. The higher received power is likely due to the better impedance matching between the tank circuit and the device.

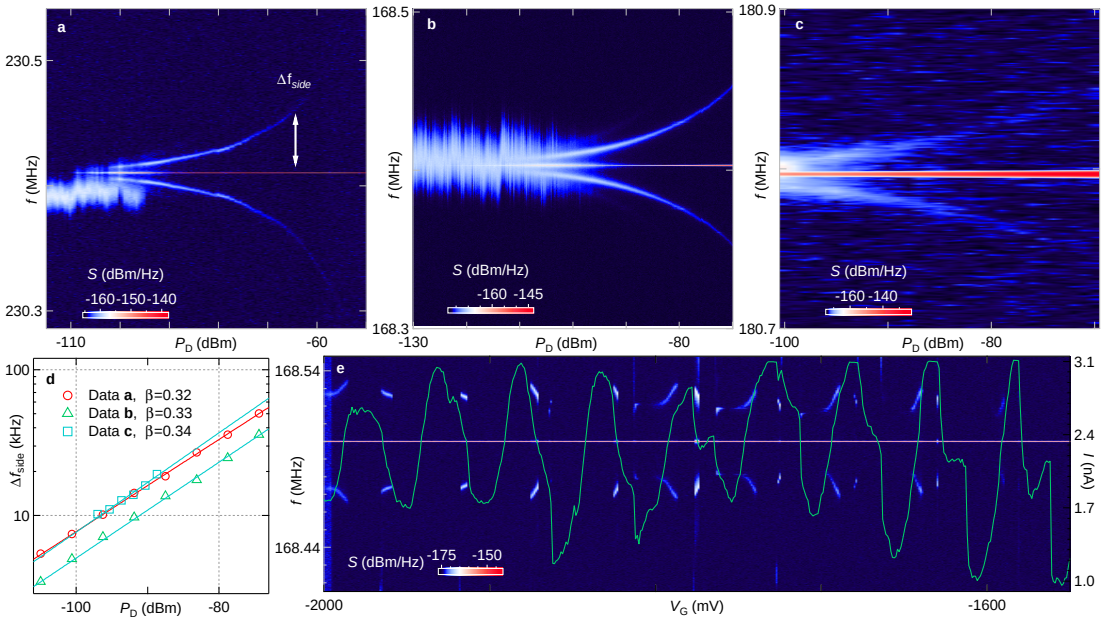


Figure 4.15: The sideband peaks. a,b,c, Transmission RF spectrum against the RF injection power at the back gate in various mechanical modes. The nanotube generates a pair of sideband peaks, the frequency offset of which increases with the injection power. **d**, Symbols: sideband spacing data taken from **a,b**. lines: fitting to $\Delta f_{\rm side} \propto P_{\rm D}^{\beta}$, with β as a free parameter. **e**, Left: Sweeping gate voltage with the injection tone fixed in power and frequency. The sideband peak shows up in the same range of frequency for a large range of gate potential. Right: The DC tunnelling current. In each Coulomb peak, the sideband peak spacing $\Delta f_{\rm side}$ is positively correlated to the current. The current saturation near 1 nA is due to the current meter.

There remains only the sideband peaks that appear when the CNT is locked to a strong RF injection. In Fig. 4.15a-c we plot the locked self-oscillation spectrum against the injection power $P_{\rm D}$ in various frequency bands. The SQUID amplifier was set off in Fig. 4.15a,b. Fig. 4.15c was taken from the same previous cool-down

as Fig. 4.14, in another cryostat with a different set of apparatus including the RF source, the HBT amplifier, the Room-temperature amplifier, the spectrum analyzer, and no SQUID amplifier. This indicates the sideband peak does not originate from the experimental setup.

The spacing between the sideband peak and the center tone Δf_{side} is power dependent. Our fitting in Fig. 4.15d shows the scaling fits very well to $\Delta f_{\text{side}} = BP_{\text{D}}^{\beta}$, where B and β are free parameters.

In Fig. 4.15e we scan V_{G} over a large voltage range, and show the sideband peak is pervasive. Compare this with the tunnel current I (right axis, green trace), we also notice in each Coulomb peak the sideband peak spacing Δf_{side} is positively correlated to the current, but there does not appears to be a general rule between those in different Coulomb peaks.

4.9.6 Joint histogram of feedback-locked oscillation

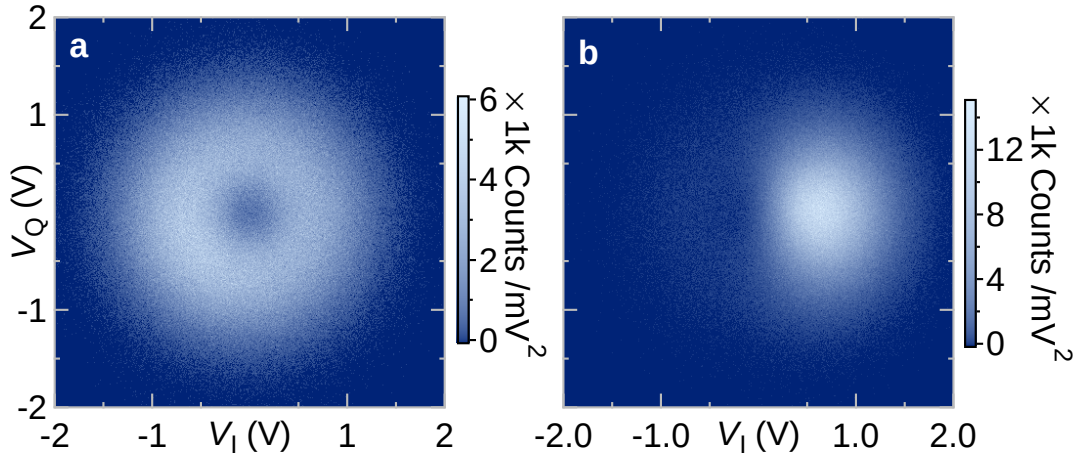


Figure 4.16: Effect of phase locking. **a**, Joint histogram, similar to Fig. 4.3c, when the oscillator is above threshold and feedback is applied with unoptimized PID parameters: $P = 500$ kV/deg, $I = 500$ kV/(deg s). **b**, Similar data with optimized parameters: $P = 105$ kV/deg, $I = 200$ kV/(deg s).

Figure 4.16 shows the effect of feedback on the coherence histogram. If the resonator were coherent but without a fixed phase, the joint histogram would show the same ring shape as Fig. 4.3c. In a perfectly phase-locked-loop, the ring would collapse towards a single point on its perimeter. Figure 4.16 shows this evolution.

When feedback is turned on but PID parameters are not optimized, the ring becomes slightly skewed (Fig. 4.16a). As the parameters are improved, the phase fluctuates less, and eventually the histogram collapses to the small arc of Fig. 4.16b.

4.9.7 50 Hz pick-up in the $g^{(2)}$ data

In Fig. 4.3f we notice the second-order autocorrelation function $g^{(2)}$ for the above threshold emission doesn't approach unity within the displayed range. This is possibly due to an unknown 50 Hz instrumental noise in either the amplifier chain or the DAC, which modulates the received power, generating an oscillation as shown in Fig. 4.17.

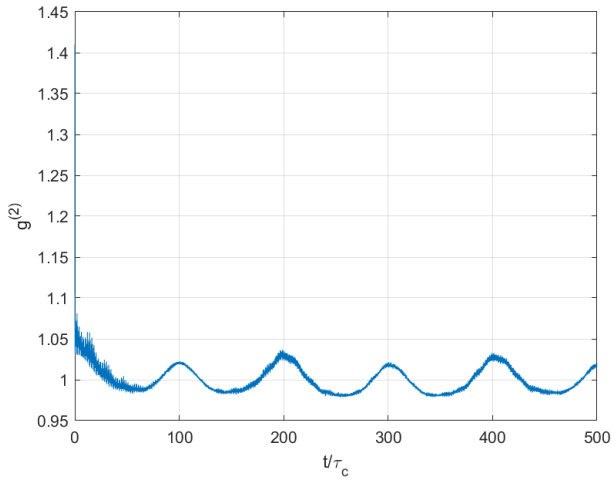


Figure 4.17: Second-order autocorrelation of the above threshold emission signal in Fig. 4.3f. $\tau_{\mathrm{coh}} = 99\,\mu\mathrm{s}$.

4.9.8 Oscillation bistability

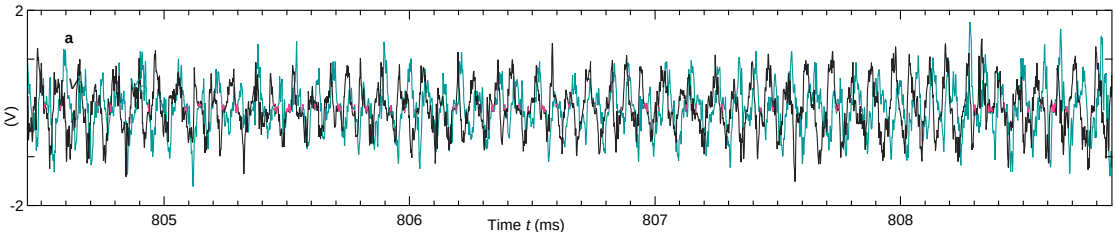


Figure 4.18: Oscillation bistability. Another excerpt from the same time trace in Fig. 4.3a highlighting (pink) when the CNT enters the other state due to bistability, either at a different frequency or stops oscillation all together, the squared sum amplitude of V_{I} and V_{Q} is nearly zero.

The faint spot at the centre of Fig. 4.3c indicates bistability [91, 94], where the nanotube is either below threshold or has switched to a different frequency outside the measurement bandwidth. The weight of the spot shows that for this gate setting the device spends approximately 0.5 % of its time in such a state [194], as hightlighted in the time traces in Fig. 4.19.

4.9.9 Strong localization

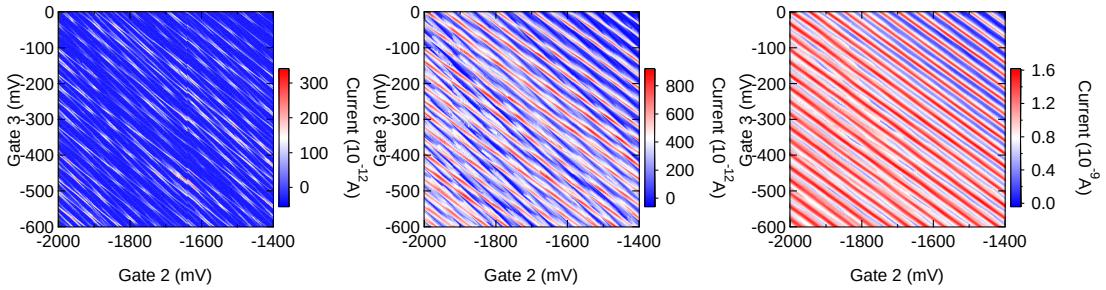


Figure 4.19: "Double dot" with a very thin middle-wall. The stability diagram with increasing bias voltage $V_{\mathrm{DS}} = 0.5\,\mathrm{mV}$ (a), $1.5\,\mathrm{mV}$ (b), $2.5\,\mathrm{mV}$ (c).

In Fig. 4.2a we see a fairly irregular Coulomb diamond patterns that appear in group of three peaks with the center one closing and two side peaks. This could, in principle, result from strong localization [219, 220] around crystalline defects in the nanotube forming a series of quantum dots. It can be seen from Fig. 4.19 as we increase the bias from 0.5 mV, 1.5 mV, to 2.5 mV, the stability diagram of gate G2 and G3 transits from a double dot honey comb into a single dot with non-closing Coulomb diamonds. Comparing the slope of the honey comb, it can be inferred that the right dot, which couples stronger to gate G2 than G3 than the left dot does, dominates the total current in the nanotube, which in turn determines the periodicity of the mechanical softening in the RF transmission spectrum Fig. 4.2b. The cotunnelling current via the left dot through the right dot therefore constitutes the side peaks in each peak group in Fig. 4.2a. The multiple energy level in the left dot might potentially serve as the energy dependent tunnelling barrier in the Section 4.7.1 model.

4.10 Conclusion

The dynamical instability explored here is an extreme consequence of invasive displacement measurement. For many kinds of nanomechanical sensing, it is a nuisance, because it means that same large bias necessary for precise measurement also strongly perturbs the displacement. However, when the aim is to detect a small frequency shift (e.g. for mass spectrometry [54] or some force-detected magnetic resonance schemes [221]), introducing feedback directly into the sensing element can be beneficial. Clearly, the external frequency stabilization schemes described in the previous section are not directly useful for sensing because they render the oscillator insensitive both to the undesirable drift and to the desirable signal (unless these can be separated spectrally). However, even without applying external stabilization, the oscillation linewidth is narrower than the resonance linewidth, just as a laser's emission is narrower than its cavity linewidth [96], making small shifts easier to detect.

A complement to this instability induced by positive feedback (negative damping) is nanomechanical cooling induced by negative feedback (positive damping). This should occur when the electromechanical contribution to the damping rate becomes positive, and may allow cooling below the refrigerator temperature, possibly down to few phonons. Unfortunately, in our experiment the measurement sensitivity, which is limited by amplifier noise and by inefficiencies in the conversion from displacement to signal voltage, was not sufficient to resolve Brownian motion (see Sec. 4.8). Further cooling may have occurred at some gate voltage settings, but was not resolved here.

The similarities between SET nanomechanics and laser physics are intriguing [96, 188]. Like a laser, this device combines a pumped two-level system with a boson cavity, and shows phase and amplitude coherence as well as self-amplification. It differs from a conventional laser by not requiring degeneracy between the SET and the resonator, since there is no stimulated emission. A desirable feature of a true phonon laser is that it should emit directionally into a propagating sound wave [222], which this experiment (like previous phonon laser realisations [177–179]) does not test. However, to the extent that the key laser characteristic is output

coherence [223], this experiment does indeed realise a phonon laser. It resembles unconventional lasers such as atom lasers that have coherent output statistics without stimulated emission [224].

5
Conclusions and outlook

In this thesis I presented a novel measurement of a suspended nanotube resonator via the radio-frequency current tunnelling through the embedded single-electron transistor, which operated as a linear amplifier. A coherent self-oscillation, induced by the measurement back-action, was recorded and analyzed. The real-time monitoring of the mechanical oscillation made it possible to implement a passive resonator stabilization scheme via a static gate voltage, with which we improved the coherence time to second-scale. Evidence was shown to indicate that the linewidth was limited by flicker noise from the environment. Due to the high tunnelling rate, the system was dominated by classical physics.

With a better tank circuit of higher quality-factor or improved amplifier thermalization, lower imprecision might be achieved, and the quantum back action due to the charge fluctuation would then be observable. Further development to this device could replace the SET with a coherent two-level system such as a double quantum dot [225], a superconducting SET [188], or an electron spin [226, 227]. This would allow a phonon laser driven by conventional stimulated emission. Ultimately, superpositions might be transferred between the two-level system and the oscillator, allowing dynamic back-action to be studied in the fully quantum limit.

Appendices

A

Fabrication processes

A.1 Carbon Nanotube synthesis

Carbon nanotubes are synthesized using chemical vapour deposition (CVD) based on the recipes adapted from Ref. [100, 228] and the references therein.

The catalyst nanoparticles are deposited on top of micro-pillars on a quartz chip. During the CVD, the nanotubes first grow vertically then fall down, by chance bridging pairs of pillars, allowing for the stamping transfer in the subsequent steps [115, 167].

A.1.1 Catalyst preparation

The catalyst used in this thesis is a methanol suspension of

- Al_2O_3 nanoparticles (0.375 mg/ml),
- $Fe(NO_3)_3 \cdot 9H_2O$ (0.5 mg/ml),
- $MoO_2(acac)_2$ (0.113 mg/ml).

A.1.2 Catalyst deposition

The quartz chip is previously patterned with pillars that are about 4 μm tall. It is then coated with 495 Poly(methyl methacrylate) (PMMA) in anisole solution,

which should be just thick enough to cover the entire chip surface while allowing the pillars to protrude. The following procedure is what I used to fabricate all the devices mentioned in this thesis:

- Ultrasonicate the catalyst suspension at highest power for at least an hour;
- Coat the quartz chip with PMMA 495k A5, spun at 6000 rpm for one minute;
- Deposit the catalyst suspension on the quartz;
- Dry in still air for 10 minutes;
- Blow dry with compressed air;
- Hard bake at 150 °C for 10 minutes;
- Cool down for two minutes;
- Ultrasonication with highest power for 30 seconds;
- Immediately squirt with cold acetone
- Immediately transfer into a second beaker of acetone to dissolve the residual PMMA.
- Wait for two hours and blow dry.

To gain better control of the total amount of catalyst nanoparticles on the chip, the quartz chips are left drying between a pair of petri dishes, one covering another. This is because the air flow in a fume hood can significantly speed up the drying process, sometimes leaving the the entire catalyst solution drying out on the sample. Special care must be taken to make sure the nanoparticles mostly remain only on top of the quartz pillars, so the last step has to be done quickly before the acetone dries, otherwise the nanoparticles would stick to the residual PMMA on chip, yielding nanotubes in unwanted places, as illustrated by Fig. A.1.

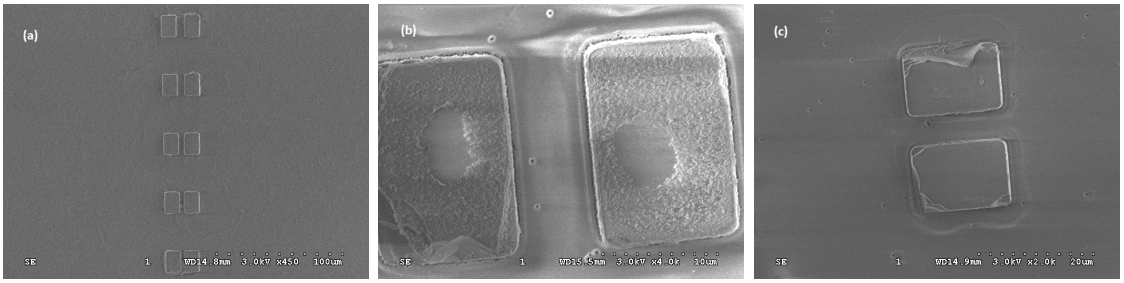


Figure A.1: Scanning electron microscope (SEM) images of the quartz chips after catalyst deposition. (a) 495A3@6000rpm. The PMMA layer is dissolved in the catalyst suspension before it dries out, and the nanoparticles are left all over the chip. (b) 495A5@6000rpm. The recipe used in this thesis. (c) 495A6@6000rpm. The PMMA layer is too thick and the pillars did not protrude.

A.1.3 Chemical vapour deposition

The next step is CVD. The quartz chip is heated to 950 °C slowly in a tube furnace while exposed to a H_2:Ar atmosphere, reducing the $Fe(NO_3)_3$ to Fe. The atmosphere is then changed to CH_4:H_2, during which period nanotubes grow to several micrometer long [100, 229]. The heating and cooling rate are controlled throughout the process to prevent the quartz chips from cracking. The full CVD recipe is as follows:

- Load the sample in the centre of the furnace.
- Connect the tube and the flange terminals.
- Check for leakage using diluted liquid soap.
- Open the main valves on the hydrogen and methane cylinders inside the gas cage.
- Open the manual gas valves on the control panel.
- Close the explosion shield.
- Set all mass flow controllers to maximum for 2 minutes to flush the lines.
- Set the hydrogen and methane controllers to zero. Set the argon controller to 200 sccm.

- Set target oven temperature to 950 °C. The heating rate should be no higher than 30 °C/ min or the quartz might shatter. Close the lid.
- When the target temperature is reached, set the hydrogen flow rate to 25 sccm, the argon flow rate to 145 sccm. Wait for 10 minutes.
- Set the methane flow rate to 91 sccm, hydrogen 800 sccm, and the growth will start. Wait for 10 minutes.
- Set the methane flow rate to zero, hydrogen 25 sccm, argon 145 sccm.
- Set the furnace temperature to zero.
- Once the furnace temperature falls below 200 °C, set the hydrogen flow rate to zero.
- Wait for 60 seconds. Set Ar flow rate to zero.
- Open the explosion shield. Open the lid of the furnace.
- Close the manual valves on the control panel.
- Disconnect the flange terminals and remove the sample.

A.2 Electrode Base Chip

The base chip is fabricated lithographically in four steps based on the original design of Tian Pei [100]. The chip is a 10 mm p-doped Silicon chip with resistivity of less than 10 Ω cm, with dry thermal oxide of thickness of 300 nm on both sides (IDBTechnology, UK).

All four electron beam lithography (EBL) steps are performed in a JEOL JBX-5500FS e-beam lithography system. While it should in principle be possible to save money and time by defining the contact pads patterns with photo lithography, the low resolution (1 μm with S1813) and the difficulty of alignment rendered it less practical for our design.

A.2.1 Global marks and bonding pads

Before lithography, the silicon chip is cleaned by sonication in hot acetone to remove all the residual glue, and then cleaned in Piranha solution (sulfuric acid:hydrogen peroxide = 3:1) for 10 minutes. For the global marks (red in Fig. 1.7(e) and bonding pads (blue in Fig. 1.7(e)) I used a bi-layer PMMA recipe:

- Spin PMMA 495k A5 for 60 s at 5000 rpm.
- Bake on hotplate at 170 °C for 5 minutes.
- Spin PMMA 950k A3 for 60 s at 5000 rpm.
- Bake on hotplate at 170 °C for 5 minutes.
- Use Electron-optical system (EOS) Mode 2 (accelerating voltage 25 kV) aperture 3 (beam current 10 nA) in the EBL.
- Expose at dose 530 μC/cm^2.
- Develop in MIBK:IPA (1:3) at 25 °C(±1 °C) for 45 s.
- Thin film deposition: 10 nm chromium + 80 nm gold.
- Lift off in acetone overnight and sonication for 1 minute.
- Rinse with acetone, IPA. Blow dry.

A.2.2 Local marks

As a local positioning reference, I write an extra set of local marks in each device. For the local marks (blue in Fig. 1.7(f)) I used a single-layer PMMA recipe:

- Spin PMMA 950k A3 for 60 s at 5000 rpm.
- Bake on hotplate at 170 °C for 5 minutes.
- Use EOS Mode 2 (accelerating voltage 25 kV) aperture 2 (beam current 1 nA) in the EBL.

- Expose at dose 530 μC/cm^2, aligned with single chip marks from the previous deposition to ensure connection.
- Develop in MIBK:IPA (1:3) at 25 °C($\pm$1 °C) for 45 s.
- Thin film deposition: 10 nm chromium + 50 nm gold.
- Lift off in acetone overnight and sonication for 1 minute.
- Rinse with acetone + IPA. Blow dry.

A.2.3 Gates

The gates (red in Fig. 1.7(f)) are the smallest features (50 nm wide, 10 nm chromium + 15 nm gold) of the devices, which require extra care in the lifting off stage to avoid residue metal debris causing short circuit. I used the same single-layer PMMA recipe as before. The EOS condition is mode 4 (accelerating voltage 50 kV) aperture 1 (beam current 0.1 nA). Each gate pattern in a device is individually aligned with three local marks.

A.2.4 Source and drain electrodes

The source and drain electrodes (yellow in Fig. 1.7(f)) are 200 nm wide, 15 nm chromium + 120 nm gold using the double-layer PMMA recipe. The EOS condition is mode 4 (accelerating voltage 50 kV) aperture 1 (beam current 0.1 nA). Each electrode pattern in a device is individually aligned with the same set of three local marks as its gates.

A.3 Stamping transfer

The nanotubes, some of which span pairs of pillars, are transferred to the device chip by stamping [115, 167].

To improve the electrical contact, we clean the gold surface with oxygen plasma immediately before stamping. In an Oxford Instruments Plasmalab 80plus reactive

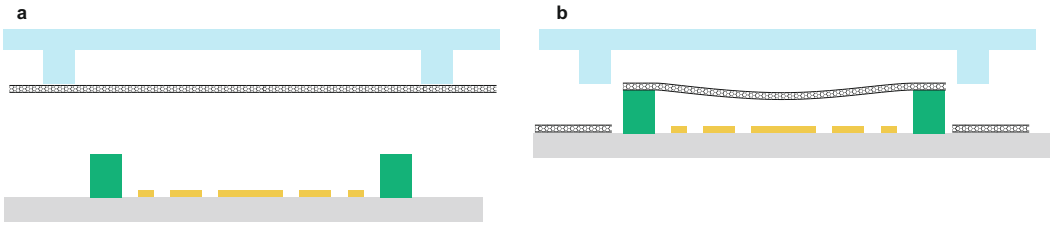


Figure A.2: Schematics of the stamping process. (a) Bring the silicon chip (grey) to about 10 micrometer below the quartz chip (blue) and align the two using global chip marks. (b) Further raise the silicon chip to contact. The nanotubes will afterwards stick to the metal electrodes (green) and snap between the electrodes and the quartz pillars.

ion etcher (RIE) system, I use 50 flow units of oxygen for 5 minutes, followed by 30 seconds of purge at 50 pressure units.

The stamping process is illustrated in Fig. A.2. The quartz chip is mounted on a transparent mask in an optical mask aligner. The silicon is fixed to the chip platform, secured by vacuum. Raise the chip platform to bring it close to the silicon chip until contact, whist constantly aligning the two using the global marks (red in Fig. 1.7(e)). The nanotubes will adhere to the metal electrodes and the silicon chip, after the quartz is removed.

A.4 Nanotube characterization and recipe optimization

In nanoscience, there is no single recipe that works in every furnace, and some adaptation is always called-for. The following is a brief recount of my efforts in nanotube characterization and recipe optimization.

A.4.1 Furnace setup

In year 2017 we assembled a CVD system in the lab, as shown in Fig. A.3. The design goals of the new CVD furnace system are to minimize the chemical contamination in the gas lines, and to allow pure methane and hydrogen without having to dilute them with argon, which I found to generate much less defects in the resultant CNTs. Compared to the old system, the new 4-inch tube furnace has improved thermal isolation, which might have also contributed to the better reproducibility of the synthesis process.

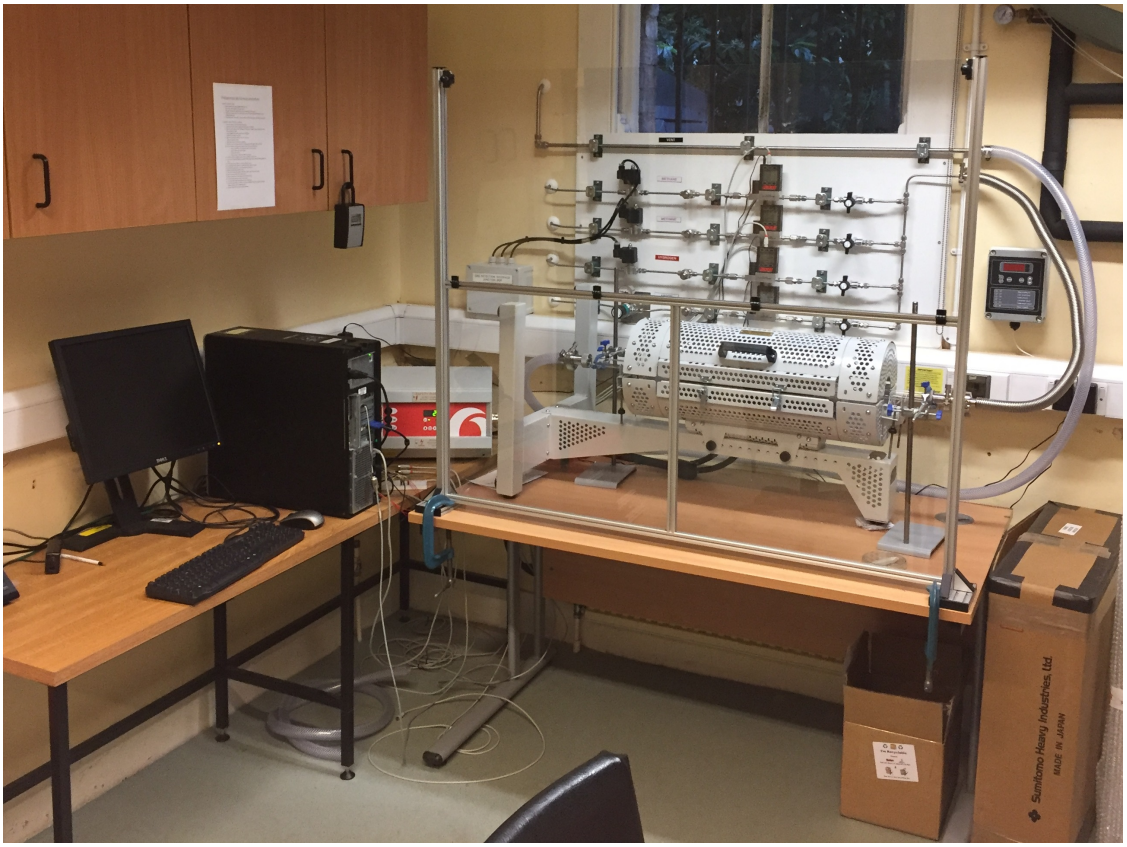


Figure A.3: Chemical vapor deposition system. Our in-house CVD system consists of (a) one set of Alicat MC-2SLPM-D/5M/5IN mass flow controller (argon) and three sets of MC-1SLPM-D/5M/5IN (hydrogen, methane, carbon-13-depleted methane), (b) one Carbolite EVT12300B-230SN tube furnace, and (c) a PC to control both the MFCs and the furnace temperature.

A.4.2 Raman spectroscopy

Raman spectroscopy [230, 231] is my go-to tool for quantitative analysis of the density of defects on the CNTs, as due to its simplicity and ease to use. Its principle of operation relies on the inelastic scattering of light. If a beam of monochromatic optical laser is shined on a sample, a small proportion of the photons will interact with the molecule bonds, generating vibrons, phonons, and various other excitations in the system, and causing its wavelength to shift. Therefore the absorption spectrum of the collected reflection light gives out a certain chemical fingerprint of the material understudy.

In carbon nanotubes, it is well-known that the graphitic sp^2 network typical of carbonaceous impurities, such as amorphous carbon particles, tends to generate an abortion peak near 1350 cm^{-1}, known as the D-band, and the tangential mode of

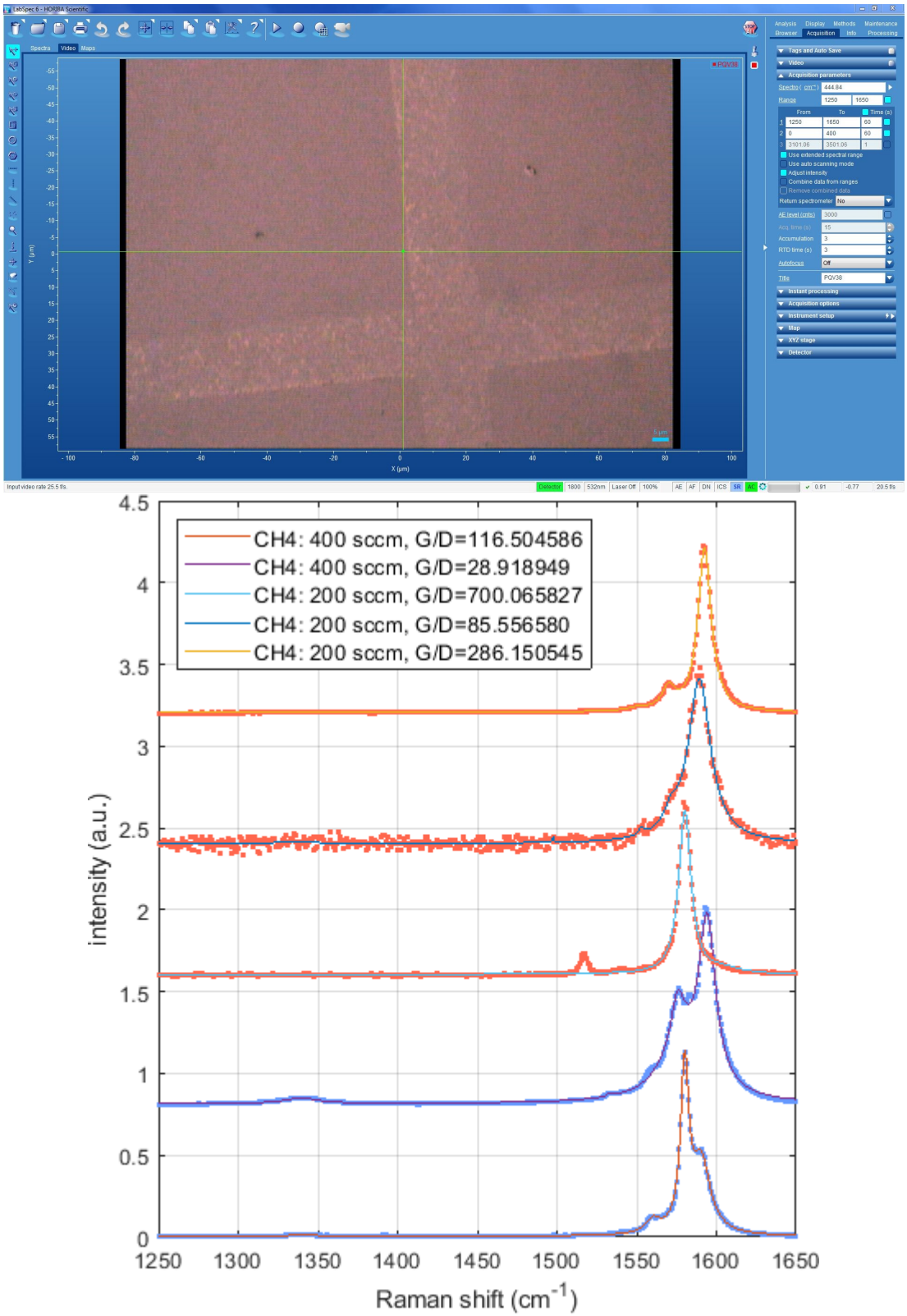


Figure A.4: Raman spectroscopy. (top) Locating the nanotubes in an optical microscope. A green laser beam of 532 nm is later projected to the center of the cross. To minimize the noise from catalyst residue, the cross is offset from the direct contact area. (bottom) The Raman spectra of nanotubes grown in an atmosphere of 200 sccm methane/1000 sccm hydrogen (red data points) and in 400 sccm methane/1000 sccm hydrogen (blue data points).

SWCNTs will result in multiple peaks around 1580 cm^{-1} (G-band) [232]. While the intensity of these absorption peaks is dependent on many factors including the density of nanotubes and the collection efficiency, but the ratio between the total intensity of the G-peaks to that of the D-peak - often called the G/D ratio - is a good indicator of the density of defects on the nanotube [232–234].

A typical set of Raman spectra is plotted in bottom panel of Fig. A.4. With all other CVD parameters controlled, here I compare the crystalline quality of the CNTs synthesized in different atmospheres. The spectra are first normalized then fitted with multi-Lorentzian functions. The extracted G/D ratio is higher for nanotubes grown in 200 sccm methane/1000 sccm hydrogen (red data points) than that in 400 sccm methane/1000 sccm hydrogen (blue data points), indicating a lower density of defects with a lower partial pressure of methane.

A.4.3 Transmission electron microscopy

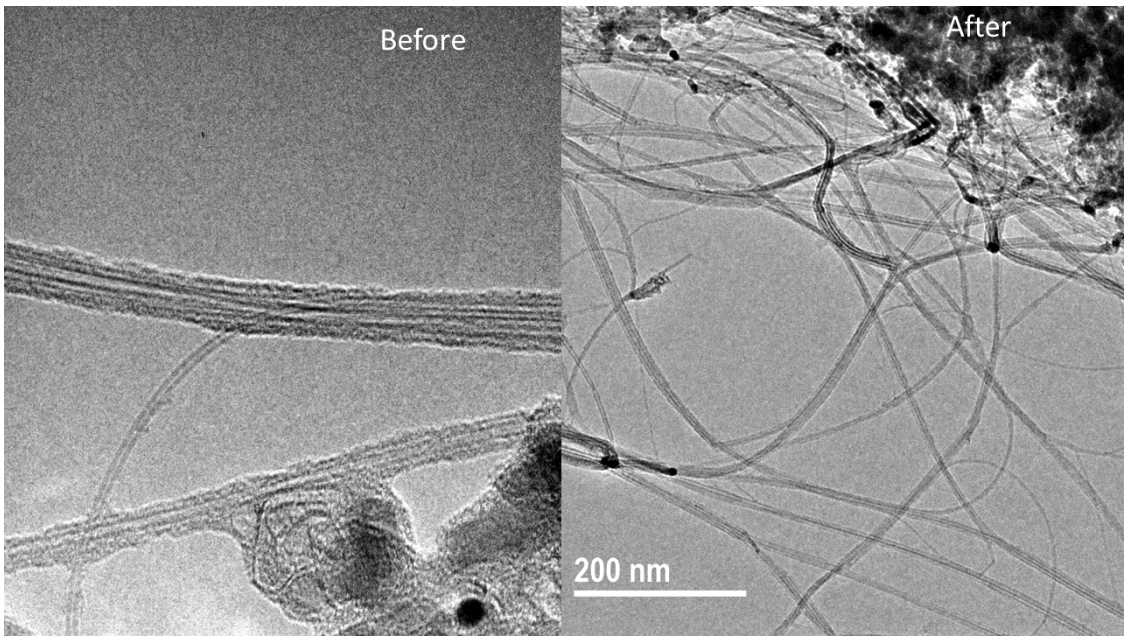


Figure A.5: TEM images of carbon nanotubes synthesized in different CVD systems
Image courtesy of Dr Alex W Robertson.

Nanotubes were transferred to a lacey carbon transmission electron microscopy (TEM) grid. Fig. A.5 compares the TEM images of the synthesized carbon nanotubes in the two systems with similar partial methane pressure, nominal CVD temperature,

and reaction time. The TEM images showed typical diameter $D = 4.5 \pm 1.5$ nm and typical number of walls $N_{\mathrm{W}} = 2 \pm 1$. It can be seen by comparison that in the new furnace, the surface of nanotubes are cleaner. There are less amorphous carbon attached to it, and less defects. We also observe a reduction in the average number of walls and bundles.

B

Autocorrelation functions of intermediate-frequency signals

Here I prove equivalence of the shifted autocorrelation functions and its standard form up to a constant frequency modulation factor.

For signals well above 1 MHz the standard route involves first shifting the signal to an intermediate frequency (heterodyning), which is then fed to a square law detector through a narrow band filter to minimize the noise in the unwanted frequency bands [116]. In the setup shown in Section 2.1, the first two steps are done in a lock-in amplifier where we extract the in-phase and quadrature components:

$$V_{\mathrm{I}}(t) \propto \mathrm{Re}\Big\{\boldsymbol{V}_{\mathrm{M}}(t)\mathrm{e}^{-\mathrm{i}2\pi f_{\mathrm{LO}}t}\Big\}\ ,\ V_{\mathrm{Q}}(t) \propto \mathrm{Im}\Big\{\boldsymbol{V}_{\mathrm{M}}(t)\mathrm{e}^{-\mathrm{i}2\pi f_{\mathrm{LO}}t}\Big\}\ . \tag{B.1}$$

The output of the lock-in amplifier is slowly-varying, so now instead of measuring the symmetrized noise power, we can again calculate the autocorrelation in the time domain. It is straightforward to prove that autocorrelation functions of these signals are equivalent to that of the original signal, modulated by the

frequency offset of the LO:

$$g^{(1)}(\tau) = \frac{\langle [V_\mathrm{I}(t) - \mathrm{i}V_\mathrm{Q}(t)]\mathrm{e}^{-\mathrm{i}2\pi(f_\mathrm{M}-f_\mathrm{LO})t}[V_\mathrm{I}(t+\tau) + \mathrm{i}V_\mathrm{Q}(t+\tau)]\mathrm{e}^{\mathrm{i}2\pi(f_\mathrm{M}-f_\mathrm{LO})(t+\tau)}\rangle}{\langle |V_\mathrm{M}(t)|^2\rangle} \tag{B.2}$$

$$\approx \frac{\langle [V_\mathrm{I}(t)V_\mathrm{I}(t+\tau) + V_\mathrm{Q}(t)V_\mathrm{Q}(t+\tau)]\mathrm{e}^{\mathrm{i}2\pi(f_\mathrm{M}-f_\mathrm{LO})\tau}\rangle}{\langle |V_\mathrm{M}(t)|^2\rangle} \tag{B.3}$$

$$= \frac{\langle V_\mathrm{I}(t)V_\mathrm{I}(t+\tau)\mathrm{e}^{\mathrm{i}2\pi(f_\mathrm{M}-f_\mathrm{LO})\tau}\rangle}{\langle V_\mathrm{I}(t)^2\rangle} \,, \tag{B.4}$$

assuming V_I and V_Q are subject to the same probability distribution. Therefore, we may estimate the phase coherence of the mechanical signal from that of the slow lock-in signal. The only difference would be an extra sinusoidal modulation to the later signal, on top of the exponentially decaying envelope.

For the second-order correlation function [131], it is evident that the LO frequency factor already cancels out in Eq. (1.24):

$$g^{(2)}(\tau) \equiv \frac{\langle V_\mathrm{M}^*(t)V_\mathrm{M}^*(t+\tau)V_\mathrm{M}(t+\tau)V_\mathrm{M}(t)\rangle}{\langle V_\mathrm{M}^*(t)V_\mathrm{M}(t)\rangle^2} \tag{B.5}$$

$$= \frac{\langle V_\mathrm{I}^2(t)V_\mathrm{I}^2(t+\tau)\rangle}{\langle V_\mathrm{I}^2(t)\rangle^2} \,. \tag{B.6}$$

References

[1] H. G. Craighead. "Nanoelectromechanical Systems". In: *Science* 290.5496 (Nov. 2000), pp. 1532–1535. DOI: 10.1126/science.290.5496.1532.

[2] MP Blencowe. "Nanoelectromechanical systems". In: *Contemp. Phys.* 46.4 (July 2005), pp. 249–264. DOI: 10.1080/00107510500146865.

[3] Robert G. Knobel and Andrew N. Cleland. "Nanometre-scale displacement sensing using a single electron transistor". In: *Nature* 424.6946 (2003), pp. 291–293. DOI: 10.1038/nature01773.

[4] Matthew D. LaHaye et al. "Approaching the Quantum Limit of a Nanomechanical Resonator". In: *Science* 304.5667 (2004), pp. 74–77. DOI: 10.1126/science.1094419.

[5] A. Naik et al. "Cooling a nanomechanical resonator with quantum back-action". In: *Nature* 443.7108 (2006), pp. 193–196. DOI: 10.1038/nature05027.

[6] P. Rabl et al. "A quantum spin transducer based on nanoelectromechanical resonator arrays". In: *Nat. Phys.* 6.8 (Aug. 2010), pp. 602–608. DOI: 10.1038/nphys1679.

[7] J. D. Teufel et al. "Nanomechanical motion measured with an imprecision below that at the standard quantum limit". In: *Nat. Nanotechnol.* 4.12 (Dec. 2009), pp. 820–823. DOI: 10.1038/nnano.2009.343.

[8] C. A. Regal, J. D. Teufel, and K. W. Lehnert. "Measuring nanomechanical motion with a microwave cavity interferometer". In: *Nat. Phys.* 4.7 (2008), pp. 555–560. DOI: 10.1038/nphys974.

[9] R.H Blick et al. "Freely suspended two-dimensional electron gases". In: *Phys. B Condens. Matter* 249-251 (June 1998), pp. 784–787. DOI: 10.1016/S0921-4526(98)00314-7.

[10] H. X. Tang et al. "Two-dimensional electron-gas actuation and transduction for GaAs nanoelectromechanical systems". In: *Appl. Phys. Lett.* 81.20 (Nov. 2002), pp. 3879–3881. DOI: 10.1063/1.1516237.

[11] I. Bargatin et al. "Sensitive detection of nanomechanical motion using piezoresistive signal downmixing". In: *Appl. Phys. Lett.* 86.13 (Mar. 2005), p. 133109. DOI: 10.1063/1.1896103.

[12] Guido Burkard. "Quantum sound on a chip". In: *Nat. Nanotechnol.* 14.4 (2019), pp. 311–312. DOI: 10.1038/s41565-019-0391-4.

[13] Luis Guillermo Villanueva, Joan Bausells, and Juergen Brugger. "Grand Challenge in N/MEMS". In: *Front. Mech. Eng.* 1.January (Jan. 2016). DOI: 10.3389/fmech.2015.00015.

[14] Debiotech. *Nanopump - Programmable Infusion Pump.*

[15] Benoit Witkamp, Menno Poot, and Herre S. J. van der Zant. "Bending-Mode Vibration of a Suspended Nanotube Resonator". In: *Nano Lett.* 6.12 (Dec. 2006), pp. 2904–2908. DOI: 10.1021/nl062206p.

[16] K. L. Ekinci. "Electromechanical transducers at the nanoscale: Actuation and sensing of motion in nanoelectromechanical systems (NEMS)". In: *Small* 1.8-9 (2005), pp. 786–797. DOI: 10.1002/smll.200500077.

[17] V.V. Avrutov et al. "NEMS Gyroscope". In: *2017 Int. Conf. Eng. Technol. Innov.* Vol. 2018-Janua. 1. IEEE, June 2017, pp. 394–398. DOI: 10.1109/ICE.2017.8279912.

[18] K. V. Klitzing, G. Dorda, and M. Pepper. "New Method for High-Accuracy Determination of the Fine-Structure Constant Based on Quantized Hall Resistance". In: *Phys. Rev. Lett.* 45.6 (Aug. 1980), pp. 494–497. DOI: 10.1103/PhysRevLett.45.494.

[19] Yoseph Imry. *Introduction to Mesoscopic Systems*. Oxford University Press, 1997.

[20] Yoseph Imry. "Mesoscopic Physics and the Fundamentals of Quantum Mechanics". In: *Phys. Scr.* T76.1 (2003), p. 171. DOI: 10.1238/physica.topical.076a00171.

[21] R. Landauer. "Spatial Variation of Currents and Fields Due to Localized Scatterers in Metallic Conduction". In: *IBM J. Res. Dev.* 1.3 (July 1957), pp. 223–231. DOI: 10.1147/rd.13.0223.

[22] Rolf Landauer. "Electrical resistance of disordered one-dimensional lattices". In: *Philos. Mag.* 21.172 (1970), pp. 863–867. DOI: 10.1080/14786437008238472.

[23] Henrik Bruus and Karsten Flensberg. *Many-Body Quantum Theory in Condensed Matter Physics—An Introduction*. 1st ed. OUP Oxford, Sept. 2004, p. 435.

[24] Supriyo Datta. *Electronic Transport in Mesoscopic Systems*. Cambridge: Cambridge University Press, 1995. DOI: 10.1017/CBO9780511805776.

[25] Gordon E. Moore. "Cramming more components onto integrated circuits, Reprinted from Electronics, volume 38, number 8, April 19, 1965, pp.114 ff." In: *IEEE Solid-State Circuits Soc. Newsl.* 11.3 (Sept. 2006), pp. 33–35. DOI: 10.1109/N-SSC.2006.4785860.

[26] U. Meirav, M. A. Kastner, and S. J. Wind. "Single-electron charging and periodic conductance resonances in GaAs nanostructures". In: *Phys. Rev. Lett.* 65.6 (Aug. 1990), pp. 771–774. DOI: 10.1103/PhysRevLett.65.771.

[27] J. H. F. Scott-Thomas et al. "Conductance Oscillations Periodic in the Density of a One-Dimensional Electron Gas". In: *Phys. Rev. Lett.* 62.5 (Jan. 1989), pp. 583–586. DOI: 10.1103/PhysRevLett.62.583.

[28] Stuart B. Field et al. "Conductance oscillations periodic in the density of one-dimensional electron gases". In: *Phys. Rev. B* 42.6 (Aug. 1990), pp. 3523–3536. DOI: 10.1103/PhysRevB.42.3523.

[29] Henk Van Houten. "Coulomb blockade oscillations in semiconductor nanostructures". In: *Surf. Sci.* 263.1-3 (1992), pp. 442–445. DOI: 10.1016/0039-6028(92)90385-J.

[30] Leo P. Kouwenhoven et al. "Electron Transport in Quantum Dots". In: *Mesoscopic Electron Transp.* Dordrecht: Springer Netherlands, 1997, pp. 105–214. DOI: 10.1007/978-94-015-8839-3_4.

[31] Leo P. Kouwenhoven, D. G. Austing, and S. Tarucha. "Few-electron quantum dots". In: *Reports Prog. Phys.* 64.6 (June 2001), pp. 701–736. DOI: 10.1088/0034-4885/64/6/201.

[32] Wilfred G. Van Der Wiel et al. "Electron transport through double quantum dots". In: *Rev. Mod. Phys.* 75.1 (2003), pp. 1–22. DOI: 10.1103/RevModPhys.75.1.

[33] R. Hanson et al. "Spins in few-electron quantum dots". In: *Rev. Mod. Phys.* 79.4 (Oct. 2007), pp. 1217–1265. DOI: 10.1103/RevModPhys.79.1217.

[34] B. M. Maune et al. "Coherent singlet-triplet oscillations in a silicon-based double quantum dot". In: *Nature* 481.7381 (2012), pp. 344–347. DOI: 10.1038/nature10707.

[35] K. C. Nowack et al. "Coherent control of a single electron spin with electric fields". In: *Science* 318.5855 (Nov. 2007), pp. 1430–1433. DOI: 10.1126/science.1148092.

[36] Mikael T. Björk et al. "Few-electron quantum dots in nanowires". In: *Nano Lett.* 4.9 (2004), pp. 1621–1625. DOI: 10.1021/nl049230s.

[37] Martin Josefsson et al. "A quantum-dot heat engine operating close to the thermodynamic efficiency limits". In: *Nat. Nanotechnol.* 13.10 (Oct. 2018), pp. 920–924. DOI: 10.1038/s41565-018-0200-5.

[38] M Heiss et al. "Self-assembled quantum dots in a nanowire system for quantum photonics". In: *Nat. Mater.* 12.5 (May 2013), pp. 439–444. DOI: 10.1038/nmat3557.

[39] Paul L McEuen. "Single-wall carbon nanotubes". In: *Phys. World* 13.6 (June 2000), pp. 31–36. DOI: 10.1088/2058-7058/13/6/26.

[40] Cees Dekker. "Carbon nanotubes as molecular quantum wires". In: *Phys. Today* 52.5 (1999), pp. 22–28. DOI: 10.1063/1.882658.

[41] David L. Klein et al. "An approach to electrical studies of single nanocrystals". In: *Appl. Phys. Lett.* 68.18 (1996), pp. 2574–2576. DOI: 10.1063/1.116188.

[42] J. R. Petta and D. C. Ralph. "Studies of Spin-Orbit Scattering in Noble-Metal Nanoparticles Using Energy-Level Tunneling Spectroscopy". In: *Phys. Rev. Lett.* 87.26 (Dec. 2001), p. 266801. DOI: 10.1103/PhysRevLett.87.266801.

[43] D. C. Ralph, C. T. Black, and M. Tinkham. "Spectroscopic measurements of discrete electronic states in single metal particles". In: *Phys. Rev. Lett.* 74.16 (Apr. 1995), pp. 3241–3244. DOI: 10.1103/PhysRevLett.74.3241.

[44] Jan von Delft and D.C. Ralph. "Spectroscopy of discrete energy levels in ultrasmall metallic grains". In: *Phys. Rep.* 345.2-3 (Apr. 2001), pp. 61–173. DOI: 10.1016/S0370-1573(00)00099-5.

[45] S. Guéron et al. "Tunneling via individual electronic states in ferromagnetic nanoparticles". In: *Phys. Rev. Lett.* 83.20 (Nov. 1999), pp. 4148–4151. DOI: 10.1103/PhysRevLett.83.4148.

[46] Jiwoong Park et al. "Coulomb blockade and the kondo effect in single-atom transistors". In: *Nature* 417.6890 (June 2002), pp. 722–725. DOI: 10.1038/nature00791.

[47] Edward A. Laird et al. “Quantum transport in carbon nanotubes”. In: *Rev. Mod. Phys.* 87.3 (July 2015), pp. 703–764. DOI: 10.1103/RevModPhys.87.703.

[48] C. W.J. Beenakker. “Theory of Coulomb-blockade oscillations in the conductance of a quantum dot”. In: *Phys. Rev. B* 44.4 (1991), pp. 1646–1656. DOI: 10.1103/PhysRevB.44.1646.

[49] H. Pothier et al. “Single-Electron Pump Based on Charging Effects”. In: *Europhys. Lett.* 17.3 (Jan. 1992), pp. 249–254. DOI: 10.1209/0295-5075/17/3/011.

[50] Michael Perlmutter and Laurent Robin. “High-performance, low cost inertial MEMS: A market in motion!” In: *Proc. 2012 IEEE/ION Position, Locat. Navig. Symp.* IEEE, Apr. 2012, pp. 225–229. DOI: 10.1109/PLANS.2012.6236884.

[51] Xining Zang et al. “Graphene and carbon nanotube (CNT) in MEMS/NEMS applications”. In: *Microelectron. Eng.* 132 (Jan. 2015), pp. 192–206. DOI: 10.1016/j.mee.2014.10.023.

[52] K L Ekinci, X M H Huang, and M L Roukes. “Ultrasensitive nanoelectromechanical mass detection”. In: *Appl. Phys. Lett.* 84.22 (May 2004), pp. 4469–4471. DOI: 10.1063/1.1755417.

[53] J. Moser et al. “Nanotube mechanical resonators with quality factors of up to 5 million”. In: *Nat. Nanotechnol.* 9.12 (2014), pp. 1007–1011. DOI: 10.1038/nnano.2014.234.

[54] J. Chaste et al. “A nanomechanical mass sensor with yoctogram resolution”. In: *Nat. Nanotechnol.* 7.5 (May 2012), pp. 301–304. DOI: 10.1038/nnano.2012.42.

[55] W. Chung Fon et al. “Nanoscale, Phonon-Coupled Calorimetry with Sub-Attojoule/Kelvin Resolution”. In: *Nano Lett.* 5.10 (Oct. 2005), pp. 1968–1971. DOI: 10.1021/nl051345o.

[56] B. Ilic et al. “Attogram detection using nanoelectromechanical oscillators”. In: *J. Appl. Phys.* 95.7 (2004), pp. 3694–3703. DOI: 10.1063/1.1650542.

[57] Terunobu Akiyama, Dominique Collard, and Hiroyuki Fujita. “Scratch drive actuator with mechanical links for self-assembly of three-dimensional MEMS”. In: *J. Microelectromechanical Syst.* 6.1 (Mar. 1997), pp. 10–17. DOI: 10.1109/84.557525.

[58] Hergen Kapels, Robert Aigner, and Josef Binder. “Fracture strength and fatigue of polysilicon determined by a novel thermal actuator”. In: *IEEE Trans. Electron Devices* 47.7 (July 2000), pp. 1522–1528. DOI: 10.1109/16.848302.

[59] Sebastian Bütefisch, Volker Seidemann, and Stephanus Büttgenbach. “Novel micro-pneumatic actuator for MEMS”. In: *Sensors Actuators A Phys.* 97-98 (Apr. 2002), pp. 638–645. DOI: 10.1016/S0924-4247(01)00843-3.

[60] M.J. Sinclair. “A high force low area MEMS thermal actuator”. In: *ITHERM 2000. Seventh Intersoc. Conf. Therm. Thermomechanical Phenom. Electron. Syst. (Cat. No.00CH37069)*. Vol. 74. 2. IEEE, 1989, pp. 127–132. DOI: 10.1109/ITHERM.2000.866818.

[61] Clark Nguyen. “MEMS technology for timing and frequency control”. In: *IEEE Trans. Ultrason. Ferroelectr. Freq. Control* 54.2 (2007), pp. 251–270. DOI: 10.1109/TUFFC.2007.240.

[62] Hwaider Lin et al. "Tunable RF band-pass filters based on NEMS magnetoelectric resonators". In: *2016 IEEE MTT-S Int. Microw. Symp.* Vol. 2016-Augus. IEEE, May 2016, pp. 1–4. DOI: 10.1109/MWSYM.2016.7540335.

[63] Sayfe Kiaei, S.M. Taleie, and Bertan Bakkaloglu. "Low-Power High-Q NEMS Receiver Architecture". In: *2005 IEEE Int. Symp. Circuits Syst.* IEEE, 2005, pp. 4401–4404. DOI: 10.1109/ISCAS.2005.1465607.

[64] Bhargav P. Nabar, Zeynep Celik-Butler, and Donald P. Butler. "A NEMS vibration energy harvester using ordered piezoelectric Zinc Oxide nanowire arrays". In: *2012 IEEE Sensors*. IEEE, Oct. 2012, pp. 1–4. DOI: 10.1109/ICSENS.2012.6411355.

[65] Kai Tao et al. "MEMS/NEMS-Enabled Vibrational Energy Harvesting for Self-Powered and Wearable Electronics". In: *Outlook Challenges Nano Devices, Sensors, MEMS*. Cham: Springer International Publishing, Jan. 2017, pp. 271–297. DOI: 10.1007/978-3-319-50824-5_9.

[66] Jacopo Iannacci. "Microsystem based Energy Harvesting (EH-MEMS): Powering pervasivity of the Internet of Things (IoT) – A review with focus on mechanical vibrations". In: *J. King Saud Univ. - Sci.* 31.1 (Jan. 2019), pp. 66–74. DOI: 10.1016/j.jksus.2017.05.019.

[67] Yole Dévelopment. *From Technologies to Markets, Status of the MEMS Industry Get high for MEMS*. 2018.

[68] N. E. Flowers-Jacobs, D. R. Schmidt, and K. W. Lehnert. "Intrinsic Noise Properties of Atomic Point Contact Displacement Detectors". In: *Phys. Rev. Lett.* 98.9 (Mar. 2007), p. 096804. DOI: 10.1103/PhysRevLett.98.096804.

[69] Yuma Okazaki et al. "Quantum point contact displacement transducer for a mechanical resonator at sub-Kelvin temperatures". In: *Appl. Phys. Lett.* 103.19 (Nov. 2013), p. 192105. DOI: 10.1063/1.4828890.

[70] Srujan Meesala et al. "Enhanced Strain Coupling of Nitrogen-Vacancy Spins to Nanoscale Diamond Cantilevers". In: *Phys. Rev. Appl.* 5.3 (Mar. 2016), p. 034010. DOI: 10.1103/PhysRevApplied.5.034010.

[71] Z. Y. Xu et al. "Deterministically entangling distant nitrogen-vacancy centers by a nanomechanical cantilever". In: *Phys. Rev. A* 80.2 (Aug. 2009), p. 022335. DOI: 10.1103/PhysRevA.80.022335.

[72] T. Kouh et al. "Diffraction effects in optical interferometric displacement detection in nanoelectromechanical systems". In: *Appl. Phys. Lett.* 86.1 (Jan. 2005), p. 013106. DOI: 10.1063/1.1843289.

[73] D. W. Carr, L. Sekaric, and H. G. Craighead. "Measurement of nanomechanical resonant structures in single-crystal silicon". In: *J. Vac. Sci. Technol. B Microelectron. Nanom. Struct.* 16.6 (Nov. 1998), p. 3821. DOI: 10.1116/1.590416.

[74] A. Schliesser et al. "Resolved-sideband cooling and position measurement of a micromechanical oscillator close to the Heisenberg uncertainty limit". In: *Nat. Phys.* 5.7 (2009), pp. 509–514. DOI: 10.1038/nphys1304.

[75] Simon Gröblacher et al. "Demonstration of an ultracold micro-optomechanical oscillator in a cryogenic cavity". In: *Nat. Phys.* 5.7 (2009), pp. 485–488. DOI: 10.1038/nphys1301.

[76] Pablo Jarillo-Herrero et al. “Electron-hole symmetry in a semiconducting carbon nanotube quantum dot”. In: *Nature* 429.6990 (May 2004), pp. 389–392. DOI: 10.1038/nature02568.

[77] Yuval Oreg, Krzysztof Byczuk, and Bertrand I. Halperin. “Spin Configurations of a Carbon Nanotube in a Nonuniform External Potential”. In: *Phys. Rev. Lett.* 85.2 (July 2000), pp. 365–368. DOI: 10.1103/PhysRevLett.85.365.

[78] Sami Sapmaz et al. “Quantum dots in carbon nanotubes”. In: *Semicond. Sci. Technol.* 21.11 (Nov. 2006), S52–S63. DOI: 10.1088/0268-1242/21/11/S08.

[79] A. D. O’Connell et al. “Quantum ground state and single-phonon control of a mechanical resonator”. In: *Nature* 464.7289 (Apr. 2010), pp. 697–703. DOI: 10.1038/nature08967.

[80] C. F. Ockeloen-Korppi et al. “Stabilized entanglement of massive mechanical oscillators”. In: *Nature* 556.7702 (Apr. 2018), pp. 478–482. DOI: 10.1038/s41586-018-0038-x.

[81] M. D. Lahaye et al. “Nanomechanical measurements of a superconducting qubit”. In: *Nature* 459.7249 (2009), pp. 960–965. DOI: 10.1038/nature08093.

[82] D Rugar et al. “Single spin detection by magnetic resonance force microscopy”. In: *Nature* 430.6997 (July 2004), pp. 329–332. DOI: 10.1038/nature02658.

[83] Menno Poot and Herre S. J. van der Zant. “Mechanical systems in the quantum regime”. In: *Phys. Rep.* 511.5 (2012), pp. 273–335. DOI: 10.1016/j.physrep.2011.12.004.

[84] K. L. Ekinci and M. L. Roukes. “Nanoelectromechanical systems”. In: *Rev. Sci. Instrum.* 76.6 (June 2005). Ed. by Stefano Cabrini and Satoshi Kawata, p. 061101. DOI: 10.1063/1.1927327.

[85] Philipp Treutlein et al. “Hybrid mechanical systems”. In: *Cavity Optomech. Nano-Micromechanical Reson. Interact. with Light* (2014), pp. 327–351. DOI: 10.1007/978-3-642-55312-7_14.

[86] Philippe Poncharal et al. “Electrostatic deflections and electromechanical resonances of carbon nanotubes”. In: *Science* 283.5407 (1999), pp. 1513–1516. DOI: 10.1126/science.283.5407.1513.

[87] Ray H. Baughman et al. “Carbon nanotube actuators”. In: *Science* 284.5418 (1999), pp. 1340–1344. DOI: 10.1126/science.284.5418.1340.

[88] Vera Sazonova et al. “A tunable carbon nanotube electrochemical oscillator”. In: *Nature* 431.7006 (2004), pp. 284–287. DOI: 10.1038/nature02905.

[89] Gary A. Steele et al. “Strong coupling between single-electron tunneling and nanomechanical motion.” In: *Science* 325.5944 (Aug. 2009), pp. 1103–1107. DOI: 10.1126/science.1176076.

[90] Chunyu Li, Erik T. Thostenson, and Tsu-Wei Chou. “Sensors and actuators based on carbon nanotubes and their composites: A review”. In: *Compos. Sci. Technol.* 68.6 (May 2008), pp. 1227–1249. DOI: 10.1016/j.compscitech.2008.01.006.

[91] O Usmani, Yaroslav M. Blanter, and Yuli V. Nazarov. “Strong feedback and current noise in nanoelectromechanical systems”. In: *Phys. Rev. B* 75.19 (2007), p. 195312. DOI: 10.1103/PhysRevB.75.195312.

[92] G. Micchi, R. Avriller, and F. Pistolesi. "Mechanical Signatures of the Current Blockade Instability in Suspended Carbon Nanotubes". In: *Phys. Rev. Lett.* 115.20 (Nov. 2015), p. 206802. DOI: 10.1103/PhysRevLett.115.206802.

[93] Omar Azim Usmani. "Strong Feedback in Nanoelectromechanical Systems". PhD thesis. TU Delft, 2006.

[94] F. Pistolesi, Yaroslav M. Blanter, and Ivar Martin. "Self-consistent theory of molecular switching". In: *Phys. Rev. B* 78.8 (Aug. 2008), p. 085127. DOI: 10.1103/PhysRevB.78.085127.

[95] D. Mozyrsky, M. B. Hastings, and I. W. Martin. "Intermittent polaron dynamics: Born-Oppenheimer approximation out of equilibrium". In: *Phys. Rev. B* 73.3 (Jan. 2006), p. 035104. DOI: 10.1103/PhysRevB.73.035104.

[96] S. D. Bennett and Aashish A. Clerk. "Laser-like instabilities in quantum nano-electromechanical systems". In: *Phys. Rev. B* 74.20 (Nov. 2006), p. 201301. DOI: 10.1103/PhysRevB.74.201301.

[97] Marcel Van de Voorde et al., eds. *Nanoelectronics: Materials, Devices, Applications*. Weinheim, Germany: Wiley-VCH Verlag GmbH & Co. KGaA, May 2017. DOI: 10.1002/9783527800728.

[98] M. L. Roukes. "Nanoelectromechanical Systems". In: (Aug. 2000).

[99] A. K. Hüttel, B. Witkamp, and H S J van der Zant. "Double quantum dots in suspended carbon nanotubes". In: *J. Phys. Conf. Ser.* 92.1 (Dec. 2007), p. 012037. DOI: 10.1088/1742-6596/92/1/012037.

[100] Tian Pei et al. "Hyperfine and Spin-Orbit Coupling Effects on Decay of Spin-Valley States in a Carbon Nanotube". In: *Phys. Rev. Lett.* 118.17 (Apr. 2017), p. 177701. DOI: 10.1103/PhysRevLett.118.177701.

[101] L. V. Radushkevich and V M Lukyanovich. "O strukture ugleroda, obrazueshegosya pri termicheskom razlozhenii okisi ugleroda na zheleznom kontakte". In: *Russ. J. Phys. Chem. A* 26.1 (1952), pp. 88–95.

[102] Sumio Iijima. "Helical microtubules of graphitic carbon". In: *Nature* 354.6348 (1991), pp. 56–58. DOI: 10.1038/354056a0.

[103] Jeroen W.G. Wildöer et al. "Electronic structure of atomically resolved carbon nanotubes". In: *Nature* 391.6662 (1998), pp. 59–62. DOI: 10.1038/34139.

[104] Min Feng Yu et al. "Strength and breaking mechanism of multiwalled carbon nanotubes under tensile load". In: *Science* 287.5453 (Jan. 2000), pp. 637–640. DOI: 10.1126/science.287.5453.637.

[105] Min-Feng Yu et al. "Tensile Loading of Ropes of Single Wall Carbon Nanotubes and their Mechanical Properties". In: *Phys. Rev. Lett.* 84.24 (June 2000), pp. 5552–5555. DOI: 10.1103/PhysRevLett.84.5552.

[106] B. I. Yakobson, C. J. Brabec, and J. Bernholc. "Nanomechanics of carbon tubes: Instabilities beyond linear response". In: *Phys. Rev. Lett.* 76.14 (Apr. 1996), pp. 2511–2514. DOI: 10.1103/PhysRevLett.76.2511.

[107] M. R. Falvo et al. "Bending and buckling of carbon nanotubes under large strain". In: *Nature* 389.6651 (Oct. 1997), pp. 582–584. DOI: 10.1038/39282.

[108] Xinjian Zhou et al. “Band structure, phonon scattering, and the performance limit of single-walled carbon nanotube transistors”. In: *Phys. Rev. Lett.* 95.14 (2005), pp. 1–4. DOI: 10.1103/PhysRevLett.95.146805.

[109] Ji Yong Park et al. “Electron-phonon scattering in metallic single-walled carbon nanotubes”. In: *Nano Lett.* 4.3 (2004), pp. 517–520. DOI: 10.1021/nl035258c.

[110] Zhaohui Zhong et al. “Terahertz time-domain measurement of ballistic electron resonance in a single-walled carbon nanotube”. In: *Nat. Nanotechnol.* 3.4 (Apr. 2008), pp. 201–205. DOI: 10.1038/nnano.2008.60.

[111] Meninder S. Purewal et al. “Scaling of resistance and electron mean free path of single-walled carbon nanotubes”. In: *Phys. Rev. Lett.* 98.18 (2007), pp. 2–5. DOI: 10.1103/PhysRevLett.98.186808.

[112] Andreas K. Hüttel et al. “Carbon nanotubes as ultrahigh quality factor mechanical resonators”. In: *Nano Lett.* 9.7 (July 2009), pp. 2547–2552. DOI: 10.1021/nl900612h.

[113] Vishal Ranjan et al. “Clean carbon nanotubes coupled to superconducting impedance-matching circuits”. In: *Nat. Commun.* 6.May (2015), p. 7165. DOI: 10.1038/ncomms8165.

[114] R Saito, G Dresselhaus, and M S Dresselhaus. *Physical Properties of Carbon Nanotubes*. Imperial College Press, July 1998. DOI: 10.1142/p080.

[115] Chung Chiang Wu, Chang Hua Liu, and Zhaohui Zhong. “One-Step Direct Transfer of Pristine Single-Walled Carbon Nanotubes for Functional Nanoelectronics”. In: *Nano Lett.* 10.3 (Mar. 2010), pp. 1032–1036. DOI: 10.1021/nl904260k.

[116] Aashish A. Clerk et al. “Introduction to quantum noise, measurement, and amplification”. In: *Rev. Mod. Phys.* 82.2 (2010), pp. 1155–1208. DOI: 10.1103/RevModPhys.82.1155.

[117] Howard M. Wiseman and Gerard J. Milburn. *Quantum Measurement and Control*. Vol. 52. 2. Cambridge: Cambridge University Press, Mar. 2009, pp. 162–163. DOI: 10.1017/CBO9780511813948.

[118] V. B. (Vladimir Borisovich) Braginskiĭ, Farid Ya. Khalili, and Kip S. Thorne. *Quantum measurement*. Cambridge University Press, 1995, p. 191.

[119] V. B. Braginsky and F. Ya Khalili. “Quantum nondemolition measurements: the route from toys to tools”. In: *Rev. Mod. Phys.* 68.1 (Jan. 1996), pp. 1–11. DOI: 10.1103/RevModPhys.68.1.

[120] J. Kelly et al. “State preservation by repetitive error detection in a superconducting quantum circuit”. In: *Nature* 519.7541 (2015), pp. 66–69. DOI: 10.1038/nature14270.

[121] S Rosenblum et al. “Fault-tolerant detection of a quantum error”. In: *Science* 361.6399 (2018), pp. 266–270. DOI: 10.1126/science.aat3996.

[122] Z. K. Minev et al. “To catch and reverse a quantum jump mid-flight”. In: *Nature* 570.7760 (June 2019), pp. 200–204. DOI: 10.1038/s41586-019-1287-z.

[123] Gerhard Kirchmair et al. “Observation of quantum state collapse and revival due to the single-photon Kerr effect”. In: *Nature* 495.7440 (2013), pp. 205–209. DOI: 10.1038/nature11902.

[124] Nissim Ofek et al. "Extending the lifetime of a quantum bit with error correction in superconducting circuits". In: *Nature* 536.7617 (Aug. 2016), pp. 441–445. DOI: 10.1038/nature18949.

[125] L Sun et al. "Tracking photon jumps with repeated quantum non-demolition parity measurements". In: *Nature* 511.7510 (July 2014), pp. 444–448. DOI: 10.1038/nature13436.

[126] Kevin S. Chou et al. "Deterministic teleportation of a quantum gate between two logical qubits". In: *Nature* 561.7723 (Sept. 2018), pp. 368–373. DOI: 10.1038/s41586-018-0470-y.

[127] H. A. Haus and J. A. Mullen. "Quantum Noise in Linear Amplifiers". In: *Phys. Rev.* 128.5 (Dec. 1962), pp. 2407–2413. DOI: 10.1103/PhysRev.128.2407.

[128] Carlton M. Caves. "Quantum limits on noise in linear amplifiers". In: *Phys. Rev. D* 26.8 (1982), pp. 1817–1839. DOI: 10.1103/PhysRevD.26.1817.

[129] Abraham Nitzan. *Chemical Dynamics in Condensed Phases. Relaxation, Transfer and Reactions in Condensed Matter Molecular Systems*. New York, New York, USA: Oxford University Press, June 2007. DOI: 10.1002/cphc.200700074.

[130] Crispin Gardiner. *Stochastic Methods: A Handbook for the Natural and Social Sciences*. 2009.

[131] Mark Fox. *Quantum Optics*. Cambridge: Oxford University Press, 2006.

[132] F. L. Walls and David W. Allan. "Measurements of Frequency Stability". In: *Proc. IEEE* 74.1 (1986), pp. 162–168. DOI: 10.1109/PROC.1986.13429.

[133] J.A. Barnes and D.W. Allan. "A statistical model of flicker noise". In: *Proc. IEEE* 54.2 (1966), pp. 176–178. DOI: 10.1109/PROC.1966.4630.

[134] W J Riley. *Handbook of frequency stability analysis*. NIST, 2008.

[135] ez SQUID. http://www.ez-squid.de/.

[136] Felix J. Schupp et al. *Radio-frequency reflectometry of a quantum dot using an ultra-low-noise SQUID amplifier*. Preprint at: https://arxiv.org/abs/1810.05767. (2018).

[137] N. Ares et al. "Sensitive Radio-Frequency Measurements of a Quantum Dot by Tuning to Perfect Impedance Matching". In: *Phys. Rev. Appl.* 5.3 (2016), p. 034011. DOI: 10.1103/PhysRevApplied.5.034011.

[138] John Clarke. "Principles and Applications of SQUIDs". In: *Proc. IEEE* 77.8 (1989), pp. 1208–1223. DOI: 10.1109/5.34120.

[139] J. R. Kirtley et al. "Scanning SQUID susceptometry of a paramagnetic superconductor". In: *Phys. Rev. B* 85.22 (2012), pp. 1–11. DOI: 10.1103/PhysRevB.85.224518.

[140] David Blair, L. Ju, and Yiqiu Ma. *Optomechanics for gravitational wave detection — from resonant bars to next generation laser interferometers*. 2017.

[141] John Clarke, Michael Hatridge, and Michael Mößle. "SQUID-Detected Magnetic Resonance Imaging in Microtesla Fields". In: *Annu. Rev. Biomed. Eng.* 9.1 (Aug. 2007), pp. 389–413. DOI: 10.1146/annurev.bioeng.9.060906.152010.

[142] Rainer Körber et al. “SQUIDs in biomagnetism: a roadmap towards improved healthcare”. In: *Supercond. Sci. Technol.* 29.11 (Nov. 2016), p. 113001. DOI: 10.1088/0953-2048/29/11/113001.

[143] Jens Koch et al. “Charge-insensitive qubit design derived from the Cooper pair box”. In: *Phys. Rev. A* 76.4 (Oct. 2007), p. 042319. DOI: 10.1103/PhysRevA.76.042319.

[144] Andrew A. Houck et al. “Controlling the spontaneous emission of a superconducting transmon qubit”. In: *Phys. Rev. Lett.* 101.8 (2008), p. 080502. DOI: 10.1103/PhysRevLett.101.080502.

[145] R. Barends et al. “Superconducting quantum circuits at the surface code threshold for fault tolerance”. In: *Nature* 508.7497 (2014), pp. 500–503. DOI: 10.1038/nature13171.

[146] Michael Mück and Robert McDermott. “Radio-frequency amplifiers based on dc SQUIDs”. In: *Supercond. Sci. Technol.* 23.9 (Sept. 2010), p. 093001. DOI: 10.1088/0953-2048/23/9/093001.

[147] J. Moser et al. “Ultrasensitive force detection with a nanotube mechanical resonator”. In: *Nat. Nanotechnol.* 8.7 (2013), pp. 493–496. DOI: 10.1038/nnano.2013.97.

[148] Hsin Ying Chiu et al. “Atomic-scale mass sensing using carbon nanotube resonators”. In: *Nano Lett.* 8.12 (2008), pp. 4342–4346. DOI: 10.1021/nl802181c.

[149] B. Lassagne et al. “Ultrasensitive mass sensing with a nanotube electromechanical resonator”. In: *Nano Lett.* 8.11 (2008), pp. 3735–3738. DOI: 10.1021/nl801982v.

[150] Renaud Leturcq et al. “Franck-Condon blockade in suspended carbon nanotube quantum dots”. In: *Nat. Phys.* 5.5 (2009), pp. 327–331. DOI: 10.1038/nphys1234.

[151] Benjamin Lassagne et al. “Coupling mechanics to charge transport in carbon nanotube mechanical resonators”. In: *Science* 325.5944 (2009), pp. 1107–1110. DOI: 10.1126/science.1174290.

[152] A. Benyamini et al. “Real-space tailoring of the electron-phonon coupling in ultraclean nanotube mechanical resonators”. In: *Nat. Phys.* 10.2 (2014), pp. 151–156. DOI: 10.1038/nphys2842.

[153] Anil Kumar Verma et al. “A rapid and efficient route to synthesis of 2-amino-4H-pyran-3-carbonitrile derivatives in the presence of L-proline and their antimicrobial activity”. In: *Der Pharma Chem.* 8.1 (2016), pp. 380–391. DOI: 10.1038/NNANO.2011.71.

[154] Andres Castellanos-Gomez et al. “Strong and tunable mode coupling in carbon nanotube resonators”. In: *Phys. Rev. B* 86.4 (July 2012), p. 041402. DOI: 10.1103/PhysRevB.86.041402.

[155] Marc Ganzhorn et al. “Carbon nanotube nanoelectromechanical systems as magnetometers for single-molecule magnets”. In: *ACS Nano* 7.7 (2013), pp. 6225–6236. DOI: 10.1021/nn402968k.

[156] Kyle Willick, Chris Haapamaki, and Jonathan Baugh. “Sensitive magnetic force detection with a carbon nanotube resonator”. In: *J. Appl. Phys.* 115.11 (2014), p. 114501. DOI: 10.1063/1.4868686.

[157] Ben H. Schneider et al. "Observation of decoherence in a carbon nanotube mechanical resonator." In: *Nat. Commun.* 5 (2014), p. 5819. DOI: 10.1038/ncomms6819.

[158] M. Poggio and B. E. Herzog. "Force-detected Nuclear Magnetic Resonance". In: *Micro Nano Scale NMR Technol. Syst.* (2017), pp. 1–31.

[159] Harold B. Meerwaldt et al. "Submicrosecond-timescale readout of carbon nanotube mechanical motion". In: *Appl. Phys. Lett.* 103.5 (2013). DOI: 10.1063/1.4817755.

[160] Kyle Willick, Xiaowu Shirley Tang, and Jonathan Baugh. "Probing the non-linear transient response of a carbon nanotube mechanical oscillator". In: *Appl. Phys. Lett.* 111.22 (2017). DOI: 10.1063/1.4991412.

[161] S. L. de Bonis et al. "Ultrasensitive Displacement Noise Measurement of Carbon Nanotube Mechanical Resonators". In: *Nano Lett.* 18.8 (Aug. 2018), pp. 5324–5328. DOI: 10.1021/acs.nanolett.8b02437.

[162] N. Ares et al. "Resonant Optomechanics with a Vibrating Carbon Nanotube and a Radio-Frequency Cavity". In: *Phys. Rev. Lett.* 117.17 (2016), p. 170801. DOI: 10.1103/PhysRevLett.117.170801.

[163] Yuehang Xu et al. "Radio frequency electrical transduction of graphene mechanical resonators". In: *Appl. Phys. Lett.* 97.24 (2010), pp. 243111–153101. DOI: 10.1063/1.3528341.

[164] J P Mathew et al. "Nanoscale Electromechanics to Measure Thermal Conductivity, Expansion, and Interfacial Losses". In: *Nano Lett.* 15.11 (2015), pp. 7621–7626. DOI: 10.1021/acs.nanolett.5b03451.

[165] Edward A. Laird et al. "A high quality factor carbon nanotube mechanical resonator at 39 GHz". In: *Nano Lett.* 12.1 (2012), pp. 193–197. DOI: 10.1021/nl203279v.

[166] Yu A. Pashkin et al. "Detection of mechanical resonance of a single-electron transistor by direct current". In: *Appl. Phys. Lett.* 96.26 (2010), pp. 8–11. DOI: 10.1063/1.3455880.

[167] Fei Pei et al. "Valley-spin blockade and spin resonance in carbon nanotubes". In: *Nat. Nanotechnol.* 7.10 (2012), pp. 630–634. DOI: 10.1038/nnano.2012.160.

[168] A. Mavalankar et al. "Photon-assisted tunneling and charge dephasing in a carbon nanotube double quantum dot". In: *Phys. Rev. B* 93.23 (2016), p. 235428. DOI: 10.1103/PhysRevB.93.235428.

[169] N. Mason, M. J. Biercuk, and Charles M. Marcus. "Local Gate Control of a Carbon Nanotube Double Quantum Dot". In: *Science* 303.5658 (Jan. 2004), pp. 655–658. DOI: 10.1126/science.1093605.

[170] Harold B. Meerwaldt, Gary A. Steele, and Herre S. J. van der Zant. "Carbon nanotubes: nonlinear high-Q resonators with strong coupling to singleelectron tunneling". In: *Fluctuating Nonlinear Oscil. From Nanomechanics to Quantum Supercond. Circuits*. Vol. 9780199691. 2012. DOI: 10.1093/acprof:oso/9780199691388.003.0012.

[171] Markus Aspelmeyer, Tobias J. Kippenberg, and Florian Marquardt. "Cavity optomechanics". In: *Rev. Mod. Phys.* 86.4 (2014), pp. 1391–1452. DOI: 10.1103/RevModPhys.86.1391.

[172] Harold B. Meerwaldt et al. "Probing the charge of a quantum dot with a nanomechanical resonator". In: *Phys. Rev. B* 86.11 (2012), p. 115454. DOI: 10.1103/PhysRevB.86.115454.

[173] Aashish A. Clerk and Steven Bennett. "Quantum nanoelectromechanics with electrons, quasi-particles and Cooper pairs: Effective bath descriptions and strong feedback effects". In: *New J. Phys.* 7 (2005), p. 238. DOI: 10.1088/1367-2630/7/1/238.

[174] S. Kafanov and P. Delsing. "Measurement of the shot noise in a single-electron transistor". In: *Phys. Rev. B* 80.15 (Oct. 2009), p. 155320. DOI: 10.1103/PhysRevB.80.155320.

[175] Hui Wang et al. "High-efficiency multiphoton boson sampling". In: *Nat. Photonics* 11.6 (2017), pp. 361–365. DOI: 10.1038/nphoton.2017.63.

[176] Rob Schoelkopf et al. "The Radio-Frequency Single-Electron Transistor (RF-SET): A Fast and Ultrasensitive Electrometer". In: *Science* 280.5367 (1998), pp. 1238–1242. DOI: 10.1126/science.280.5367.1238.

[177] K Vahala et al. "A phonon laser". In: *Nat. Phys.* 5.9 (2009), pp. 682–686. DOI: 10.1038/nphys1367.

[178] Ivan S Grudinin et al. "Phonon Laser Action in a Tunable Two-Level System". In: *Phys. Rev. Lett.* 104.8 (Feb. 2010), p. 083901. DOI: 10.1103/PhysRevLett.104.083901.

[179] I. Mahboob et al. "Phonon lasing in an electromechanical resonator". In: *Phys. Rev. Lett.* 110.12 (2013), p. 127202. DOI: 10.1103/PhysRevLett.110.127202.

[180] Yutian Wen et al. "Measuring carbon nanotube vibrations using a single-electron transistor as a fast linear amplifier". In: *Appl. Phys. Lett.* 113.15 (Oct. 2018), p. 153101. DOI: 10.1063/1.5052185.

[181] Ilya Khivrich, Aashish A. Clerk, and Shahal Ilani. "Nanomechanical pump–probe measurements of insulating electronic states in a carbon nanotube". In: *Nat. Nanotechnol.* 14.2 (Jan. 2019), pp. 161–167. DOI: 10.1038/s41565-018-0341-6.

[182] D. Mozyrsky, I. W. Martin, and M. B. Hastings. "Quantum-Limited Sensitivity of Single-Electron-Transistor-Based Displacement Detectors". In: *Phys. Rev. Lett.* 92.1 (Jan. 2004), p. 018303. DOI: 10.1103/PhysRevLett.92.018303.

[183] Jens Koch, Felix von Oppen, and A. V. Andreev. "Theory of the Franck-Condon blockade regime". In: *Phys. Rev. B* 74.20 (Nov. 2006), p. 205438. DOI: 10.1103/PhysRevB.74.205438.

[184] Enrique Burzurí et al. "Franck-condon blockade in a single-molecule transistor". In: *Nano Lett.* 14.6 (2014), pp. 3191–3196. DOI: 10.1021/nl500524w.

[185] A Mitra, I Aleiner, and A J Millis. "Phonon effects in molecular transistors: Quantal and classical treatment". In: *Phys. Rev. B* 69.24 (June 2004), p. 245302. DOI: 10.1103/PhysRevB.69.245302.

[186] C. B. Doiron, W. Belzig, and C. Bruder. "Electrical transport through a single-electron transistor strongly coupled to an oscillator". In: *Phys. Rev. B* 74.20 (Nov. 2006), p. 205336. DOI: 10.1103/PhysRevB.74.205336.

[187] Andrew D. Armour, M P Blencowe, and Y Zhang. "Classical dynamics of a nanomechanical resonator coupled to a single-electron transistor". In: *Phys. Rev. B* 69.12 (Mar. 2004), p. 125313. DOI: 10.1103/PhysRevB.69.125313.

[188] D. A. Rodrigues, J. Imbers, and Andrew D. Armour. "Quantum Dynamics of a Resonator Driven by a Superconducting Single-Electron Transistor: A Solid-State Analogue of the Micromaser". In: *Phys. Rev. Lett.* 98.6 (Feb. 2007), p. 067204. DOI: 10.1103/PhysRevLett.98.067204.

[189] S. I. Klselev et al. "Microwave oscillations of a nanomagnet driven by a spin-polarized current". In: *Nature* 425.6956 (2003), pp. 380–383. DOI: 10.1038/nature01967.

[190] I. Tsioutsios et al. "Real-Time Measurement of Nanotube Resonator Fluctuations in an Electron Microscope". In: *Nano Lett.* 17.3 (Mar. 2017), pp. 1748–1755. DOI: 10.1021/acs.nanolett.6b05065.

[191] Arthur W. Barnard et al. "Real-time vibrations of a carbon nanotube". In: *Nature* 566.7742 (Feb. 2019), pp. 89–93. DOI: 10.1038/s41586-018-0861-0.

[192] Cyril Elouard, Maxime Richard, and Alexia Auffèves. "Reversible work extraction in a hybrid opto-mechanical system". In: *New J. Phys.* 17.5 (May 2015), p. 055018. DOI: 10.1088/1367-2630/17/5/055018.

[193] Juliette Monsel, Cyril Elouard, and Alexia Auffèves. "An autonomous quantum machine to measure the thermodynamic arrow of time". In: *npj Quantum Inf.* 4.1 (Dec. 2018), p. 59. DOI: 10.1038/s41534-018-0109-8.

[194] Y.-Y. Liu et al. "Semiconductor double quantum dot micromaser". In: *Science* 347.6219 (Jan. 2015), pp. 285–287. DOI: 10.1126/science.aaa2501.

[195] M. C. Cassidy et al. "Demonstration of an ac Josephson junction laser". In: *Science* 355.6328 (2017), pp. 939–942. DOI: 10.1126/science.aah6640.

[196] Toshimasa Fujisawa et al. "Spontaneous emission spectrum in double quantum dot devices". In: *Science* 282.5390 (Oct. 1998), pp. 932–935. DOI: 10.1126/science.282.5390.932.

[197] P. G. Steeneken et al. "Piezoresistive heat engine and refrigerator". In: *Nat. Phys.* 7.4 (2011), pp. 354–359. DOI: 10.1038/nphys1871.

[198] Robert Adler. "A Study of Locking Phenomena in Oscillators". In: *Proc. IRE* 34.6 (1946), pp. 351–357. DOI: 10.1109/JRPROC.1946.229930.

[199] H. L. Stover and W. H. Steier. "Locking of Laser Oscillators by Light Injection". In: *Appl. Phys. Lett.* 8.4 (Feb. 1966), pp. 91–93. DOI: 10.1063/1.1754502.

[200] Y.-Y. Liu et al. "Injection locking of a semiconductor double-quantum-dot micromaser". In: *Phys. Rev. A* 92.5 (Nov. 2015), p. 53802. DOI: 10.1103/PhysRevA.92.053802.

[201] S Knünz et al. "Injection Locking of a Trapped-Ion Phonon Laser". In: *Phys. Rev. Lett.* 105.1 (July 2010), p. 013004. DOI: 10.1103/PhysRevLett.105.013004.

[202] Maximilian J. Seitner et al. “Parametric Oscillation, Frequency Mixing, and Injection Locking of Strongly Coupled Nanomechanical Resonator Modes”. In: *Phys. Rev. Lett.* 118.25 (June 2017), p. 254301. DOI: 10.1103/PhysRevLett.118.254301.

[203] J S Huber et al. *Detecting squeezing from the fluctuation spectrum of a driven nanomechanical mode*. Preprint at: https://arxiv.org/abs/1903.07601. (2019).

[204] C. Stambaugh and H. B. Chan. “Supernarrow Spectral Peaks near a Kinetic Phase Transition in a Driven Nonlinear Micromechanical Oscillator”. In: *Phys. Rev. Lett.* 97.11 (Sept. 2006), p. 110602. DOI: 10.1103/PhysRevLett.97.110602.

[205] R. W. P. Drever et al. “Laser phase and frequency stabilization using an optical resonator”. In: *Appl. Phys. B Photophysics Laser Chem.* 31.2 (June 1983), pp. 97–105. DOI: 10.1007/BF00702605.

[206] B. P. Abbott et al. “LIGO: the Laser Interferometer Gravitational-Wave Observatory”. In: *Reports Prog. Phys.* 72.7 (July 2009). Ed. by D. G. Blair et al., p. 076901. DOI: 10.1088/0034-4885/72/7/076901.

[207] A. L. Schawlow and C. H. Townes. “Infrared and optical masers”. In: *Phys. Rev.* 112.6 (Dec. 1958), pp. 1940–1949. DOI: 10.1103/PhysRev.112.1940.

[208] H M Wiseman. “Light amplification without stimulated emission: Beyond the standard quantum limit to the laser linewidth”. In: *Phys. Rev. A* 60.5 (1999), pp. 4083–4093. DOI: 10.1103/PhysRevA.60.4083.

[209] Steven T. Cundiff and Jun Ye. “Colloquium: Femtosecond optical frequency combs”. In: *Rev. Mod. Phys.* 75.1 (Mar. 2003), pp. 325–342. DOI: 10.1103/RevModPhys.75.325.

[210] R. P. Erickson et al. “Frequency Comb Generation in Superconducting Resonators”. In: *Phys. Rev. Lett.* 113.18 (Oct. 2014), p. 187002. DOI: 10.1103/PhysRevLett.113.187002.

[211] P Solinas et al. “A Josephson radiation comb generator”. In: *Sci. Rep.* 5.1 (Dec. 2015), p. 12260. DOI: 10.1038/srep12260.

[212] Katsuhiko Ogata. *Modern control engineering*. Prentice hall, 1970.

[213] Yaroslav M. Blanter, O. Usmani, and Yuli V. Nazarov. “Erratum: Single-Electron Tunneling with Strong Mechanical Feedback [Phys. Rev. Lett. 93 , 136802 (2004)]”. In: *Phys. Rev. Lett.* 94.4 (Feb. 2005), p. 049904. DOI: 10.1103/PhysRevLett.94.049904.

[214] Nader Kalantar, Christopher S. Takehana, and Nina L. Shapiro. “Outcomes of reduced postoperative stay following outpatient pediatric tonsillectomy”. In: *Int. J. Pediatr. Otorhinolaryngol.* 70.12 (2006), pp. 2103–2107. DOI: 10.1021/nl302036x.

[215] A. Tavernarakis et al. “Optomechanics with a hybrid carbon nanotube resonator”. In: *Nat. Commun.* 9.1 (Dec. 2018), p. 662. DOI: 10.1038/s41467-018-03097-z.

[216] Anthony E. Siegman. *Lasers*. 1990 editi. University Science Books, 1986, p. 1285.

[217] M. A. Hopcroft. *allan_overlap.m*. https://uk.mathworks.com/matlabcentral/fileexchange/26441-allan_overlap. Mar. 18, 2014.

[218] Jil Schwender et al. "Improving the read-out of the resonance frequency of nanotube mechanical resonators". In: *Appl. Phys. Lett.* 113.6 (2018). DOI: 10.1063/1.5045309.

[219] David Ferry and Stephen Marshall Goodnick. *Transport in Nanostructures*. Cambridge: Cambridge University Press, 1997. DOI: 10.1017/CBO9780511626128.

[220] Thomas Ihn. *Semiconductor Nanostructures: Quantum States and Electronic Transport*. Oxford University Press, Nov. 2010, pp. 1–568. DOI: 10.1093/acprof:oso/9780199534425.001.0001.

[221] B C Stipe et al. "Electron Spin Relaxation Near a Micron-Size Ferromagnet". In: *Phys. Rev. Lett.* 87.27 (Dec. 2001), p. 277602. DOI: 10.1103/PhysRevLett.87.277602.

[222] W Maryam et al. "Dynamics of a vertical cavity quantum cascade phonon laser structure". In: *Nat. Commun.* 4.1 (Dec. 2013), p. 2184. DOI: 10.1038/ncomms3184.

[223] H. Wiseman. "Defining the (atom) laser". In: *Phys. Rev. A* 56.3 (Sept. 1997), pp. 2068–2084. DOI: 10.1103/PhysRevA.56.2068.

[224] Anton Öttl et al. "Correlations and Counting Statistics of an Atom Laser". In: *Phys. Rev. Lett.* 95.9 (Aug. 2005), p. 090404. DOI: 10.1103/PhysRevLett.95.090404.

[225] T Brandes and N Lambert. "Steering of a bosonic mode with a double quantum dot". In: *Phys. Rev. B* 67.12 (Mar. 2003), p. 125323. DOI: 10.1103/PhysRevB.67.125323.

[226] C Ohm et al. "Readout of carbon nanotube vibrations based on spin-phonon coupling". In: *Appl. Phys. Lett.* 100.14 (Apr. 2012), p. 143103. DOI: 10.1063/1.3698395.

[227] András Pályi et al. "Spin-orbit-induced strong coupling of a single spin to a nanomechanical resonator". In: *Phys. Rev. Lett.* 108.20 (2012), p. 206811. DOI: 10.1103/PhysRevLett.108.206811.

[228] Fei Pei. "Quantum transport in one-dimensional nanostructures". PhD thesis. TU Delft, 2015.

[229] Jing Kong et al. "Synthesis of individual single-walled carbon". In: *Nature* 395.3 (1998), pp. 1–4. DOI: 10.1038/27632.

[230] Gordon G. Hammes. *Spectroscopy for the Biological Sciences*. Hoboken, NJ, USA: John Wiley & Sons, Inc., June 2005, pp. 1–172. DOI: 10.1002/0471733555.

[231] M.A. Hazle et al. *Practical Raman Spectroscopy*. Ed. by Derek J. Gardiner and Pierre R. Graves. Vol. 1. 1. Berlin, Heidelberg: Springer Berlin Heidelberg, 1989, p. 104. DOI: 10.1007/978-3-642-74040-4.

[232] Hiromichi Kataura, Yasumitsu Miyata, and Kohei Mizuno. "Purity and defect characterization of single-wall carbon nanotubes using raman spectroscopy". In: *J. Nanomater.* 2011.7 (2011), pp. 1–7. DOI: 10.1155/2011/786763.

[233] Vincent Jourdain and Christophe Bichara. "Current understanding of the growth of carbon nanotubes in catalytic chemical vapour deposition". In: *Carbon N. Y.* 58 (2013), pp. 2–39. DOI: 10.1016/j.carbon.2013.02.046.

[234] Christian Thomsen and Stephanie Reich. "Raman Scattering in Carbon Nanotubes". In: *Light Scatt. Solid IX*. Vol. 65. 23. Berlin, Heidelberg: Springer Berlin Heidelberg, May 2002, pp. 115–234. DOI: 10.1007/978-3-540-34436-0_3.